# Design, Modeling and Fabrication of Polymer-based Capacitive Micromachined Ultrasonic Transducers (polyCMUTs)

by

Carlos Daniel Gerardo Hernandez

B.Sc., The Autonomous University of San Luis Potosi, 2007
M.Sc., The Autonomous University of San Luis Potosi, 2010

A THESIS SUBMITTED IN PARTIAL FULFILLMENT OF
THE REQUIREMENTS FOR THE DEGREE OF

DOCTOR OF PHILOSOPHY

in

The Faculty of Graduate and Postdoctoral Studies

(Electrical & Computer Engineering)

THE UNIVERSITY OF BRITISH COLUMBIA

(Vancouver)

October 2018

The following individuals certify that they have read, and recommend to the Faculty of Graduate and Postdoctoral Studies for acceptance, the dissertation entitled:

Design, Modeling and Fabrication of Polymer-based Capacitive Micromachined Ultrasonic Transducers (polyCMUTs)

submitted by Carlos Daniel Gerardo Hernandez in partial fulfillment of the requirements for the degree of: Doctor of Philosophy

in Electrical and Computer Engineering

**Examining Committee:**

Edmond Cretu
Supervisor

Robert Rohling
Co-supervisor

Mona Berciu
University Examiner

Guangrui Xia
University Examiner

Sazzadur Chowdhury
External University Examiner

Carlos Ventura
University Chair

# Abstract

Capacitive Micromachined Ultrasonic Transducers (CMUTs) are considered advantageous over piezoelectric transducers for ultrasound imaging for the high bandwidth, ease of integration with electronics and miniaturization. Research efforts over the past two decades have been focusing on manufacturing and system integration of CMUTs to achieve comparable and better performance than the piezoelectric counterparts, while the uniqueness of the CMUT structure is barely exploited.

This thesis explores the modeling, simulation, fabrication and characterization of CMUTs fabricated using polymer materials. We begin by developing a large-signal non linear model (macromodel) to analyze the energy interactions between the electrical, mechanical and acoustic domains in CMUTs. The simulation results are in good agreement with FEM simulations and experimental results.

The development of a macromodel for a special kind of CMUTs called asymmetric CMUTs is also presented. Asymmetric CMUTs have three electrodes that can be independently addressed to excite non-axisymmetric vibration modes in the CMUT membrane. Some of the applications of this mode include super-resolution algorithms and physical beam steering.

In an attempt to reduce manufacturing costs while improving the perfor-

mance in CMUTs, we fabricated a polymer-based CMUT (polyCMUT) using inexpensive materials, minimum fabrication steps and fabrication times of less than 24 hours. The fabricated polyCMUTs have low excitation voltages ($10V_{DC}$ and $15V_{AC}$) and presented a phenomenon termed pre-biasing; which allowed us to operate the polyCMUT as passive device in receiving mode. The first B-mode ultrasound image in the world created using polyCMUTs is also presented.

The exploration of fabricating electronics devices using the same materials as polyCMUTs is also presented in chapter 5. A mixture containing the photopolymer SU-8 and silver nanoparticles was used to pattern planar capacitors and inductors. An electroplating stage enhanced the performance of the patterned devices. It is shown that this technique can be used to fabricate high-density interconnections with $5\mu$m line widths.

Future integration of polyCMUTs and polymer-based passive devices on flexible substrates is described at the end of this thesis. As a future work we plan to develop an ultra-low cost portable ultrasound systems on flexible patches for continuous health monitoring applications.

# Lay Summary

Capacitive Micromachined Ultrasonic Transducers (CMUTs) are considered the replacement of piezoelectric transducers in biomedical ultrasound systems. CMUTs have larger bandwidths, easier electronic integration and miniaturization capabilities.

We developed a nonlinear mathematical model to predict the behavior of CMUTs under different operating conditions and to optimize the design prior fabrication.

A simple microfabrication technique using inexpensive polymer materials was developed to fabricate polymer-based CMUTs (polyCMUTs). The proposed technique allowed us to fabricate biomedical ultrasound prototypes in less than 24 hours with materials costs below $100 USD. We created the first B-mode ultrasound image in the world using polyCMUTs.

The exploration of fabricating electronics devices using the same polymer materials as polyCMUTs is also presented. A mixture photopolymers and silver nanoparticles was used to create planar capacitors, miniature inductors and ultra thin interconnection lines.

As a future work we plan to develop an ultra-low cost portable ultrasound systems on flexible substrates for continuous health monitoring applications.

# Preface

All of the work presented henceforth was conducted in the Adaptive Microsystems Laboratory and in the Robotics and Control Laboratory at the University of British Columbia, Point Grey campus.

Dr. Edmond Cretu and Dr. Robert Rohling were the supervisory authors on this project and were involved throughout the materials and concepts presented in all chapters, including manuscript edits.

A brief summary of the major contributions and related publications of this thesis is below:

Chapter 2 proposes a large-signal model for CMUTs based on energy-flow theory, the simulation results and the comparison against FEM simulations and experimental results have been submitted for journal publication.

The macromodel developed for asymmetric CMUTs presented in chapter 3 were presented in a conference: C. D. Gerardo, E. Cretu, and R. Rohling, Nonlinear model with lumped parameters for asymmetric CMUTs, in Ultrasonics Symposium (IUS), 2015 IEEE International, 2015, pp. 14.

The novel concept of fabrication of CMUTs using polymer materials were published as the following journal paper:

Gerardo, C.D., Cretu, E., Rohling, R., Fabrication and testing of polymer-based Capacitive Micromachined Ultrasound Transducers for medical imag-

ing, Nature Microsystems and Nanotechnology, DOI: 10.1038/S41378-018-0022-5.

The fabrication design procedure and the details outlined in this publication were filed as the following United States patent application:

Cretu, E., Rohling, R. and Gerardo, C.D., Layered structure and method for fabricating same. Filed on December 2017.

The material covered in chapter 5 regarding electrical passive components fabricated with conductive SU-8 was published as the following journal article:

C. D. Gerardo, E. Cretu, and R. Rohling, Fabrication of Circuits on Flexible Substrates Using Conductive SU-8 for Sensing Applications, Sensors, vol. 17, no. 6, p. 1420, Jun. 2017.

The experimental results shown in Appendix C were shown as a presentation in the conference:

C. D. Gerardo, A. Kulpa, and E. Cretu, "Electrostatically actuated 3D printed microstructures for sensing applications", in 2nd International Congress on Materials and Renewable Energy (MRE2014) and Nanomaterials Symposia, Hong Kong, 2014.

# Table of Contents

**Abstract** . . . . . **iii**

**Lay Summary** . . . . . **v**

**Preface** . . . . . **vi**

**Table of Contents** . . . . . **viii**

**List of Tables** . . . . . **xiii**

**List of Figures** . . . . . **xiv**

**Table of abbreviations** . . . . . **xxvii**

**Acknowledgments** . . . . . **xxix**

**Dedication** . . . . . **xxx**

**1 Background and motivation** . . . . . **1**

1.1 Principle of Ultrasound Imaging Systems . . . . . 1

1.2 Ultrasonic transducers . . . . . 3

1.3 Capacitive Micromachined Ultrasound Transducers (CMUTs) 5

1.3.1 Operation Principle of CMUTs . . . . . 6

1.3.2 Modeling of CMUTs . . . . . 11
1.3.3 Fabrication techniques . . . . . 14
1.3.4 Applications of CMUTs . . . . . 17
1.3.5 Disadvantages of CMUTs . . . . . 18
1.4 Integrating CMUTs with imaging systems . . . . . 20
1.5 Hypotheses and potential benefits . . . . . 20
1.5.1 Development of multi-vibration mode large-signal model 22
1.5.2 Rapid low cost fabrication of prototype transducers . 23
1.5.3 Capability for a hybrid integration . . . . . 24
1.6 Contribution and structure of the thesis . . . . . 25

**2 Equivalent circuit macromodel for CMUTs . . . . . 26**
2.1 CMUT modeling problem . . . . . 26
2.1.1 Mason model (MS) . . . . . 27
2.2 Equivalent circuit model of CMUTs . . . . . 28
2.2.1 Parallel-plate model (PP) . . . . . 30
2.2.2 Deflected Membrane model (DM) . . . . . 33
2.3 Simulations and experimental results . . . . . 35
2.3.1 Sine excitation . . . . . 38
2.4 Discussions and conclusions . . . . . 46

**3 Equivalent circuit macromodel for asymmetric CMUTs . . 48**
3.1 Equivalent circuit macromodel . . . . . 50
3.1.1 Parallel-plate approach . . . . . 51
3.1.2 Mode participation factors approach . . . . . 56
3.2 Simulations and experimental results . . . . . 57

3.2.1 Air operation . . . . . 58
3.2.2 Immersed operation . . . . . 61
3.3 Pull-in detection . . . . . 66
3.4 Impedance analyzer measurements . . . . . 67
3.5 Conclusions and Discussion . . . . . 68

**4 Polymer-based CMUTs (polyCMUTs) . . . . . 70**
4.1 Motivation of using polymers as structural material . . . . . 71
4.2 Structural materials . . . . . 72
4.3 Selection of sacrificial layer . . . . . 72
4.3.1 Explored sacrificial materials . . . . . 73
4.3.2 Omnicoat . . . . . 75
4.4 Fabrication of polyCMUTs . . . . . 77
4.5 Results and Discussion . . . . . 92
4.5.1 Optical characterization . . . . . 92
4.5.2 Validation of operation . . . . . 93
4.5.3 Pre-biasing . . . . . 96
4.5.4 B-mode imaging . . . . . 101
4.6 Discussions and conclusions . . . . . 105

**5 Polymer-based fabrication techniques for integrating electronic subsystems . . . . . 109**
5.1 Functionalized materials . . . . . 110
5.1.1 Functionalized SU-8 Preparation . . . . . 114
5.1.2 Sample processing . . . . . 115
5.2 Experimental results . . . . . 116

5.2.1 Copper electroplating . . . . . 120
5.2.2 Inductors fabrication . . . . . 121
5.2.3 High-density interconnections . . . . . 126
5.2.4 LC resonant circuit . . . . . 127
5.2.5 Bending effects . . . . . 127
5.3 Hybrid integration of conductive SU-8 and CMUTs . . . . . 132
5.3.1 Optimum energy transfer using embedded passive components . . . . . 132
5.4 Conclusions and discussions . . . . . 133

**6 Conclusions and future work . . . . . 135**
6.1 Summary of the thesis . . . . . 135
6.2 Contributions to the state of knowledge . . . . . 142
6.3 Future directions . . . . . 143
6.3.1 Fabrication of polyCMUTs on flexible substrates . . . 143
6.3.2 Large-area ultrasound systems . . . . . 145
6.3.3 High-frequency polyCMUTs . . . . . 146
6.3.4 Charge trapping control of CMUTs . . . . . 147
6.3.5 Hybrid integration with electronics . . . . . 148

**Bibliography . . . . . 149**

**Appendices . . . . .**

**A Combining Symmetric and Asymmetric CMUTs . . . . . 168**

**B Polysilicon-based CMUTs experimentation . . . . . 173**

**C Alternative fabrication for CMUTs . . . . . 177**

# List of Tables

2.1 Equivalence between the variables used in Mason's model and this model . . . . . 34
2.2 Simulation parameters . . . . . 35
2.3 Simulated and measured pull-in voltages . . . . . 45

3.1 Simulation parameters for asymmetric CMUTs . . . . . 57

4.1 Parameters of fabricated polyCMUTs . . . . . 82

# List of Figures


1.1 Basic ultrasound imaging system. Acoustic waves generated and sensed by a transducer array are used to create sonograms. 2

1.2 Resolutions in an ultrasound array. Axial resolution lies along the beam propagation direction. Lateral resolution is perpendicular to the beam propagation and along the transducer array. Elevational resolution is also perpendicular to the beam propagation, but along the transducer height. . . . 4

1.3 Components of a CMUT array. (a) CMUT cell. (b) CMUT Element. (c) CMUT array . . . . . 7

1.4 First two natural vibration modes of a CMUT cell. (a) (0,1) mode. (b) (1,1) mode . . . . . 9

1.5 Higher vibration modes in a circular membrane. . . . . 9

2.1 Typical Mason-like model. The electrical domain (left portion of circuit) is coupled to the mechanical domain (right) using a linear transformer. The acoustic interaction is done through the impedance $Z_R$ . . . . . 28

2.2 Basic parallel-plate equivalent circuit model [1]. With permission from the author. . . . . 30

2.3 Mode equivalent circuit of a single cell CMUT. The electrical domain (left portion of circuit) is coupled to the mechanical domain by a dependent current source $I_{ES}$, representing the electrostatic force. . . . . 30

2.4 Simulated normalized radiation impedance for a single CMUT membrane clamped all-around. . . . . 33

2.5 Membrane deflection profiles simulated for modes DM and PP under different bias voltages. . . . . 36

2.6 Implementation of the DM model for symmetric CMUTs in Matlab-Simulink, a script containing the implementation with Bessel functions is located in the subsystem at the lower-left corner. . . . . 37

2.7 Model in Comsol of a single CMUT immersed in water. The membrane sits on an infinite baffle modeled by sound rigid walls. A semi-sphere with boundary conditions set to radiate spherical waves captures the effect of fluid loading. . . . . 37

2.8 Diagram of the described polyCMUT, the top electrode is purposely embedded in the membrane to decrease the effective gap between electrodes. . . . . 38

2.9 Simulated variation in the membrane deflection as the DC bias voltage is increased. The linear behavior of Mason model does not capture in an accurately way the membrane deflection at high voltages, where it gets amplified closer to pull-in. 40

2.10 Simulated sinusoidal excitation of CMUTs without DC bias (pure AC). Using the proposed models (DM and PP), the membrane deflects at twice the input frequency as expected whereas Mason's model incorrectly follows the input frequency. 41

2.11 Comparison of the normalized frequency response of CMUTs with symmetric excitation in air. . . . . 42

2.12 Comparison of the normalized frequency response of CMUTs with symmetric excitation in water. . . . . 43

2.13 The proposed macromodel can capture the spring softening effect without adding extra electrical components to the circuit as in Mason's model . . . . . 44

2.14 Comparison of membrane deflection when the bias voltage is gradually increased beyond the pull-in voltage. The linear behavior of Mason models is evident. The proposed model is able to capture the pull-in and snap-back operations. . . . . 45

2.15 Capacitance measurement using an impedance analyzer when the DC bias voltage is gradually increased. A change in the slope in the capacitance reading reveals a pull-in voltage around 60V. . . . . 46

3.1 Top and cross-section view of a symmetric CMUT cell (left), and an asymmetric CMUT cell (right). . . . . 49

3.2 Measurement of the deflection of an asymmetric CMUT cell during asymmetric excitation. The result is a "tilted" membrane. . . . . 49

3.3 First two natural vibration modes of a CMUT cell. **(a)** Mode (0,1) **(b)** Mode (1,1). . . . . 50
3.4 Deflections of an asymmetric CMUT membrane considering a parallel plate capacitor model. . . . . 52
3.5 (0,1) mode and (1,1) mode equivalent circuit of an asymmetric CMUT. . . . . 53
3.6 Deflection of the asymmetric CMUT membrane when (a) voltage is applied on both bottom electrodes, (b) "tilted membrane" effect when voltage is applied on one bottom electrode only. . . . . 56
3.7 Implementation of the macromodel for asymmetric CMUTs in Matlab-Simulink, a script containing the implementation with Bessel functions is located in the subsystem at the lower-left corner. . . . . 58
3.8 Model in Comsol of a single CMUT immersed in water. The membrane sits at the bottom of a water column to model array operation of CMUTs. The cylinder walls are set to sound hard boundary conditions. The other end of the cylinder is set to radiate planer waves. . . . . 59
3.9 Comparison of the normalized frequency response of CMUTs with symmetric excitation in air. . . . . 60
3.10 Comparison of the normalized frequency response of CMUTs with asymmetric excitation in air. . . . . 61
3.11 Comparison of the normalized frequency response of CMUTs with symmetric+asymmetric excitation in water. . . . . 62

3.12 Excitation voltages in an asymmetric CMUT to produce a pure asymmetric excitation mode (only mode (1,1) present). . 63

3.13 Comparison of different types of operation modes in an asymmetric CMUT. . . . . 63

3.14 Capacitance levels on left and right electrodes of an asymmetric CMUT cell during (a) symmetric excitation and (b) asymmetric excitation. . . . . 64

3.15 Spring softening effect of a CMUT cell (a) symmetric excitation and (b) asymmetric excitation. . . . . 65

3.16 Pull-in detection in asymmetric CMUTs with symmetric excitation (same voltage applied on both top electrodes). . . . . 66

3.17 Pull-in detection in asymmetric CMUTs with asymmetric excitation (voltage applied on one top electrodes, the second top electrode is grounded). . . . . 67

3.18 Impedance measurements of CMUTs immersed in mineral oil for different depths. The ripples in the measurements are thought to be originated by reverberations in the air-oil interface . . . . . 68

4.1 Overbaked S1813 as sacrificial layer. a) Patterned square areas using S1813 prior spin coating SU-8, these square areas will become the cavities of CMUTs, b) SU-8 structures patterned on top of the sacrificial layer, an ultrasound bath had to be used to partially remove the S1813 underneath, leading to damage of the membranes. . . . . 74

4.2 Poly-acrylic acid (PAA) as sacrificial layer. a) Patterned square areas prior spin coating SU-8, these square areas will become the cavities of CMUTs, b) SU-8 structures patterned on top of the sacrificial layer, an undesirable residual layer formed between the interface between SU-8 and PAA. . . . . 76

4.3 Poly-vinyl acid (PVA) as sacrificial layer. a) Patterned square areas with release channels prior spin coating SU-8, these square areas will become the cavities of CMUTs, b) SU-8 structures patterned on top of the sacrificial layer, the sacrificial material did not etch completely through the etch channels. 76

4.4 Experimentation with Omnicoat as sacrificial layer. a) Patterned Omnicoat structures, b) Layer of SU-8 deposited on Omnicoat structures with patterned holes to access the sacrificial layer, c) Omnicoat layer gradually being etched when the sample was immersed in developer MF319, d) Omnicoat sacrificial layer completely removed. SU-8 structures were not damaged even after 48 hours immersed in developer. . . . 78

4.5 Cross-section view of the six fabrication steps used to create polymer-based CMUTs (polyCMUTs) . . . . . 79

4.6 Overview of the six fabrication steps used to create polymer-based CMUTs (polyCMUTs) . . . . . 80

4.7 Experimental setup to assess the best geometry for sacrificial release channels. An array of circular membranes with releasing channels varying in length and width. Photolithography design (top). Fabricated structures (bottom). Optimum design was 5$\mu$m X 15$\mu$m release channels. . . . . 84

4.8 PolyCMUTs with embedded electrodes in the membrane. Electrodes with different effective areas were tested to assess the adhesion of chromium and SU-8. No delamination problems were encountered. . . . . 86

4.9 Table showing the different generations of polyCMUTs fabricated for this project. The fill factor in the elements was gradually increasing while lowering the operational voltage. . 89

4.10 PCB interface for polyCMUTs linear array. Electrical connections located at bottom of board. (a) Render model designed in Altium, (b) Real prototype. . . . . 90

4.11 PolyCMUT linear array being wire bonded to interface PCB using aluminum wires. Forces on the bonding tool damaged electrodes on the surface of polyCMUTs with only a few successful bonds. . . . . 91

4.12 PolyCMUT linear array connected to interface PCB using flexible Kapton film and high-purity silver ink. . . . . 92

4.13 (a) 64 element CMUT linear array mounted on PCB. (b) Six CMUT elements separated by a pitch of 550 $\mu$m. (c) CMUT cells showing interconnected top electrodes and cavities underneath, the optical transparency of SU-8 allows a visual identification of any possible defect. . . . . 93

4.14 In air characterization of polymer CMUTs showing the first vibration mode at 2.83 MHz. . . . . 94

4.15 Static topography of a CMUT element using a white light interferometer. . . . . 95

4.16 Experimental setup for polyCMUTs. An external piezoelectric probe used as acoustic source. The polyCMUT array was connected to bias-tee for echo detection. . . . . 95

4.17 Acoustic response in mineral oil from polymer-based CMUT and FFT of received acoustic pulse showing a 101.6% fractional bandwidth. . . . . 96

4.18 Ultrasound pulses generated by polymer CMUTs recorded every 30 minutes for a period of 12 hours. Signals stayed within 95% of the maximum detected peak . . . . . 97

4.19 PolyCMUTs C-V charging curves. The intrinsic (build-in) bias is inferred from symmetry lines in C-V curves. (a) Negative charging, (b) Positive charging. . . . . 100

4.20 Contribution of different factors towards the total CMUT membrane deflection. . . . . 101

4.21 (a) Diagram of the wire phantom used; 12 aluminum wires spaced by 5 mm. (b) Photograph of the actual wire phantom immersed in mineral oil. (c) B-mode image of a wire phantom using a linear array of polymer-based CMUTs using a display dynamic range of 30 dB. (d) Assessment of the lateral resolution, the FWHM for the first 5 wires down to a depth of 50 mm was less than 1.5 mm. . . . . 103

4.22 B-mode comparison of a wire phantom array using (a) poly-CMUT linear array, (b) Commercial L14-5 piezoelectric probe, (c) Commercial C5-2 piezoelectric probe. . . . . 104

4.23 Adhesion test of calibration featured patterned in SU-8 on flexible Kapton film. . . . . 105

5.1 Cloverleaf design with conductive SU-8 for sheet resistance measurement. The topography on the right was measured using a white light interferometer. . . . . 117

5.2 I-V graph showing a linear behavior for structures patterned using functionalized SU-8. . . . . 117

5.3 Array of microinductors fabricated using conductive SU-8 with the proposed fabrication technique. Microinductor with 5$\mu$m lines and 20$\mu$m spacing shown in the inset. . . . . 118

5.4 **(a)** RC filter showing the capacitor on the left and the resistance path on the right. **(b)** Dark-field view of a capacitor finger showing the silver nanoparticles embedded in the SU-8 matrix. . . . . 119

5.5 Experimental frequency response of a low-pass RC filter fabricated using conductive SU-8 on Kapton film. . . . . 119

5.6 Dark-field microscope images showing the dispersion of silver nanoparticles in different locations within a sample **(a)** Center of sample. **(b)** Area close to the edge of sample. . . . 120

5.7 Cross-sectional view of the conductive line monitored for different electroplated times . . . . . 121

5.8 Resistivity variation of a 100$\mu$m conductive SU-8 line for a 1mA electroplating current. . . . . 122

5.9 **(a)** NFC antenna fabricated with functionalized SU-8 as a seed layer after copper electroplating.**(b)** Detailed view of electroplated traces. . . . . 123

5.10 **(a)** Topography of replicated NFC antenna design before electroplating. **(b)** Topography after electroplating. . . . . 124

5.11 Frequency response of fabricated NFC antenna with electroplated copper on top of conductive SU-8. . . . . 124

5.12 **(a)** Microinductor with 5$\mu$m line width and 20$\mu$m spacing fabricated with condcutive SU-8. **(b)** Topography measurement after electroplating . . . . . 125

5.13 **(a)** BGA fan-out interconnection circuit. **(b)** Detailed view of the center of the array. . . . . 126

5.14 **(a)** Patterned LC circuit before electroplating. **(b)** LC circuit after electroplating, the copper thickness around the conductive SU-8 is 4.5$\mu$m. . . . . 128

5.15 Broad frequency response of the fabricated LC circuit with electroplated copper on top of conductive SU-8 with measured values shown in inset. . . . . 128

5.16 **(a)** Mechanical setup for bending test. **(b)** Bending test of LC circuit when bending radius is 15mm. . . . . 130

5.17 Frequency response of the fabricated LC circuit with electroplated copper on top of conductive SU-8 for different bending radii. . . . . 131

5.18 Electroplated copper traces peeling off the substrate after 10 bending cycles when r=5mm. . . . . 131

5.19 Surface-mounted capacitor soldered between electroplated tracks on functionalized SU-8. . . . . 132

6.1 Futuristic vision of polyCMUT-based portable and flexible ultrasound system for continuous cardiac monitoring. . . . . 144

6.2 Cross sectional view of CMUTs and polyCMUTs for different frequency range. (a) The effective gap CMUTs increases as the membrane get thicker for high-frequency operations, (b) The effective gap in polyCMUTs remains the same regarding the operational frequency thanks to their embedded electrodes. 147

A.1 Proposed chip structure of the CMUT array. Containing 32 rows of square membranes and 32 rows of rectangular membranes in parallel . . . . . 169

A.2 General layout of the asymmetric CMUT array, showing the details of individual cells and the test structures . . . . . 170

A.3 Parameters of the asymmetric CMUT array, including theoretical and experimental values of the resonant frequencies . . 170

A.4 Measured topography of the different CMUT cells in the chip and the simulated cross-sectional view. Left to right: CMUTs in the array, test cells 2 and test cells 3 . . . . . 171

A.5 Comparison of the frequency response of asymmetric CMUTs in the array showing the separation in frequency ($\delta$) between the mode (0,1) for the square membranes and mode (1,1) for the rectangular membranes . . . . . 172

B.1 Section view of CMUT array showing the unsealed membranes (left), the printing pattern (center) and the cells after sealing (right) . . . . . 175

B.2 Frequency response of a row of sealed CMUT membranes showing the variation in resonant frequency . . . . . 175

C.1 Different electrostatically actuated structures showing the frequency response and the deflections measured using an LDV. Left to right: cantilevers, doubly-clamped beams and square membranes . . . . . 179

C.2 Support structure from 3D printer showing the printer bottom electrodes (left). Measured topography revealing the discrepancies between the 3D model and the real model . . . 180

C.3 Final device with the copper tape glued on the support structure (top). Frequency response and deflection shape of membranes captured by an LDV (bottom) . . . . . 181

C.4 Cavities created using a Laser Micromachining System (left) and measured topography using a white light interferometer (right) . . . . . 182

C.5 Final device showing the electrical connections on top (left). Frequency response of 500um (top) and 1mm membranes (bottom) . . . . . 183

# Table of abbreviations

| **Abbreviation** | **Meaning** |
|---|---|
| CMUT | Capacitive Micromachined Ultrasonic Transducer |
| CMOS | Complementary metal-oxide-semiconductor |
| FEM | Finite element modeling |
| FFT | Fast Fourier Transform |
| FWHM | Full width at half maximum |
| HDPE | High-density polyethylene |
| IVUS | Intravascular ultrasound |
| LDV | Laser Doppler Vibrometer |
| MEMS | Microelectromechanical systems |
| NFC | Near Field Communication |
| PAA | Poly-acrylic acid |
| PDMS | Polydimethylsiloxane |
| PEDOT:PSS | poly(3,4-ethylenedioxythiophene) polystyrene sulfonate |
| PMGI | Polymethylglutarimide |
| PMMA | polymethylmethacrylate |
| polyCMUT | Polymer-based Capacitive Micromachined Ultrasonic Transducer |
| PVA | Poly-vynil acid |

| **Abbreviation** | **Meaning** |
|---|---|
| PVDF | Polyvinylidene fluoride |
| PZT | Lead zirconate titanate |
| RF | Radio frequency |
| SNR | Signal-to-noise ratio |
| UV | Ultraviolet |
| TPE | Thermoplastic elastometers |

# Acknowledgments

The authors would like to thank CMC Microsystems Canada and the Natural Sciences and Engineering Research Council of Canada (NSERC) for their funding, software and fabrication support.

We thank the Science and Technology National Council of Mexico (CONACYT) and the Science and Technology Council of San Luis Potosi (COPOCYT) for their funding.

We thank Manyou Ma for her support with the synthetic aperture beamforming algorithm during B-mode imaging reconstruction. We thank Maan Almarghalani for his support during the creation of the functionalized SU-8 and Chang Ge for his help with the electroplating system during the creation of flexible passive devices.

# Dedication

To my beautiful wife Adriana and my three lovely kids Daniel, Annika and Derek, you truly made this possible.

# Chapter 1

# Background and motivation

Ultrasound imaging is the most widely used medical imaging modality in the world in terms of the number of images created annually. In an ultrasound imaging system, ultrasonic waves emitted by a transducer travel along soft tissues, creating wave reflections (echoes) at the interfaces between two different tissues; these echoes travel back to the transducer and are collected and processed to form an ultrasound image. The collection and subsequent processing of multiple echo signals along different directions is the basis of ultrasound image formation. Ultrasound transducers are a key component in an ultrasound imaging system, which transform electrical voltages into acoustic waves and vice versa.

## 1.1 Principle of Ultrasound Imaging Systems

Figure 1.1 shows a diagram of a basic ultrasound system; the ultrasound waves sent from, and received by, a group of elements are usually tuned with different time delays and gains, so that waves from different elements meet at a certain focal point along a scan line. During reception, the transducer converts the returning echoes along a scan line into electronic signals that are subsequently amplified and converted to digital signals. The amplitude

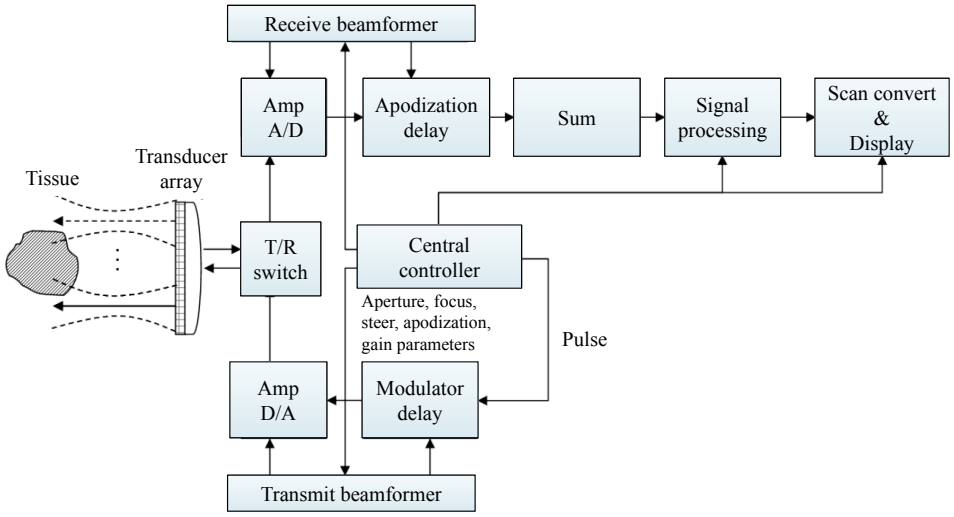


Figure 1.1: Basic ultrasound imaging system. Acoustic waves generated and sensed by a transducer array are used to create sonograms.

of received echo signals are mapped into a grayscale representation, where high-amplitude signals appear as bright pixels on a monitor (hence the name B-mode, or brightness-mode).

The main performance criteria in an ultrasound system are the bandwidth, sensitivity and resolution. A broad bandwidth is desired so it would be possible to capture the range of frequencies contained in echoes returning from tissues. The sensitivity refers to the ability to capture small variations in the detected signals from noise, especially faint echoes from deep locations. Penetration is another way of quantifying sensitivity. It can be determined from the signal-to-noise ratio (SNR) measurements; it is the depth at which the SNR falls below 6dB. The physical design of an ultrasonic transducer as well as the materials used mainly dictates the bandwidth and sensitivity.

Figure 1.2 shows the three different kinds of resolutions in an ultrasound imaging system. The axial (longitudinal) resolution is in the beam propagation direction and depends on the pulse length and the wavelength (operating frequency). The lateral (transverse) resolution is perpendicular to the beam propagation, but within the plane of the image, it depends on the focusing and aperture (number and spacing of transducer elements in an array). The elevational (slice) resolution is also perpendicular to the beam propagation, and depends on the height and physical lens of the transducer. Another type of resolution is called contrast resolution, which is altered by compression of the range of the reflected ultrasound amplitudes, number of bits per pixel, and the use of contrast agents.

The axial resolution improves with smaller wavelengths (high frequencies), but higher frequencies have also lower penetrating power in tissues. This gives the fundamental trade-off of depth penetration with resolution in all ultrasound systems.

## 1.2 Ultrasonic transducers

Medical ultrasound systems have traditionally used piezoelectric materials for its transducers since the 1930s. Materials such as piezoelectric crystals (e.g. quartz), ceramics (e.g. lead zirconate titanate (PZT)), and polymers (e.g. polyvinylidene fluoride (PVDF)) have been used as the transducer materials [2].

Despite the fact that piezoelectric transducers technology is mature, it suffers many drawbacks, such as expensive fabrication technology, limited

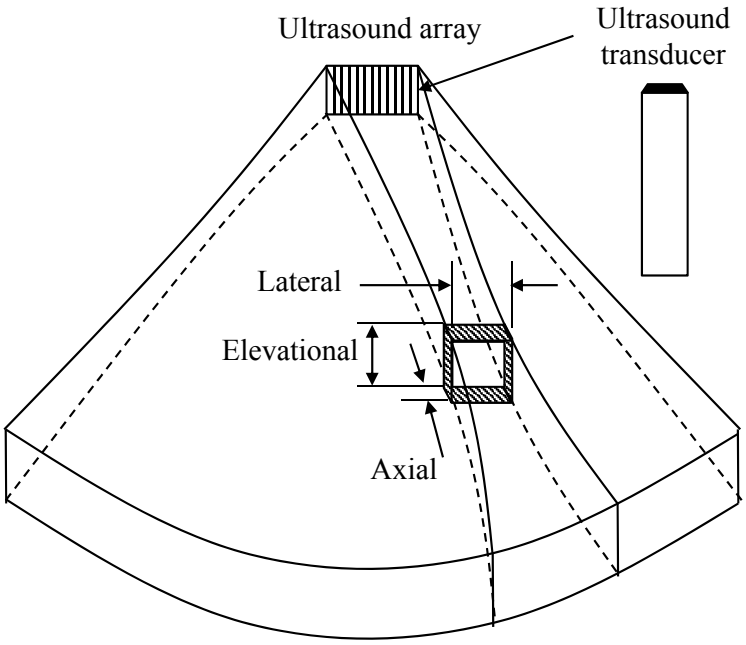


Figure 1.2: Resolutions in an ultrasound array. Axial resolution lies along the beam propagation direction. Lateral resolution is perpendicular to the beam propagation and along the transducer array. Elevational resolution is also perpendicular to the beam propagation, but along the transducer height.

geometrical designs, difficulties achieving small kerf sizes, technical challenges in fabricating large two-dimensional arrays due to interconnect technologies [2] and the integration with electronics at the die-level.

An appropriate acoustic impedance matching between the transducer and the medium is paramount in ultrasound imaging systems, as this impedance matching has a profound impact on the efficiency of the system. For current piezoelectric-based systems, there is a high acoustic impedance mismatch between piezoelectric crystals ($\sim$30 MRayl) and soft tissues ($\sim$1.5

MRayl). Typically, layers of high-density rubber, which act as an acoustic matching layer, are placed between the transducer and the medium. The matching layer however is not always available for high-frequency transducers and certain bandwidth restrictions [3]. Although piezoelectric imaging transducers having fractional bandwidths [1] of the order of 80% and higher are becoming gradually available, the majority of the imaging transducers exhibit limited bandwidths, typically in the range $30-50\%$ [4].

The electromechanical coupling coefficient ($k$) characterizes the efficiency of an ultrasound transducer. For piezoelectric transducers, the bandwidth is determined by $k$ [5]; while a high $k$ is desirable for the useful vibration mode, a low $k$ is often required for other competing modes, in order to suppress the spurious response caused by mode coupling [6]. This $k$ value is not constant and depends on the shape and dimensions of the transducer [7]; other factors such as backing substrate, residual stress and electrode coverage can also affect this coefficient [8].

## 1.3 Capacitive Micromachined Ultrasound Transducers (CMUTs)

An alternative to the piezoelectric effect is the electrostatic principle. The operation principle of electrostatic transducers is based on electrostatic attraction of two metallic electrodes. Even though the idea of electrostatic ultrasonic transducers is as old as the piezoelectric transducers, piezoelectric materials have dominated the ultrasonic industry. The reason why capaci-

[1] The fractional bandwidth is the bandwidth of a device divided by its center frequency. It is a figure of merit in ultrasound imaging systems.

tive transducers have not played a role before is that electric field strengths on the order of a million volts per centimeter ($10^6$ V/cm) are required [2].

Thanks to recent advances in microfabrication, it has been possible to create Capacitive Micromachined Ultrasonic Transducers (CMUTs) with operating characteristics competing with their piezoelectric counterparts, and are considered as a potential replacement for piezoelectric transducers by the ultrasound imaging community [2], with even some commercially available CMUT-based ultrasound systems emerging in the market [9, 10].

Conventional piezoelectric arrays are typically fabricated by mechanically dicing piezoelectric crystals and filling the kerfs with a polymer. Using this approach, the fabrication of ultrasonic arrays operating above 20MHz is very challenging [11]. This contrasts with the wide range of operating frequencies of CMUTs, some of them reportedly reaching 60MHz [12].

### 1.3.1 Operation Principle of CMUTs

CMUTs are typically made up of silicon or silicon nitride membranes suspended over a metallic substrate. CMUTs offer certain potential advantages over their piezoelectric counterparts, such as wider bandwidth, higher operating frequency, closer integration with electronics and ease of fabricating large arrays [2]. A CMUT cell is essentially a quasi-parallel plate capacitor consisting of a metalized membrane (top electrode) suspended above an electrically conductive substrate (bottom electrode) as shown in Figure 1.3a. The dimension of the membrane is usually in the order of tens of microns, with a sub-micron gap between the electrodes, which provides the dielectric space for capacitive actuation. Many of these individual cells are

grouped in parallel to create large groups called CMUT elements as shown in Figure 1.3b. Groups of CMUT elements make a CMUT array (Figure 1.3c), which can be in the form of linear, ring or 2D arrays.


(a) (b) (c)

Figure 1.3: Components of a CMUT array. (a) CMUT cell. (b) CMUT Element. (c) CMUT array

### Symmetric CMUTs

During the CMUT operation, a voltage is applied between the two electrodes (bottom electrode and metalized membrane) causing the membrane to deflect towards the substrate by the electrostatically induced force; since the membrane is usually clamped all around, the mechanical stress within the membrane resists this attraction. Applying a high frequency AC voltage produces an alternating electrostatic force that generates ultrasound waves. If the membrane is subjected to ultrasound echoes, an output current is generated in the circuit between the electrodes due to the capacitance change under constant bias voltage. The amplitude of this current output is a function of the amplitude and frequency of the incident wave and the capacitance of the device. A DC voltage called bias voltage is typically used and combined with an AC voltage on transmit to maintain a closer

gap between the electrodes, increasing its sensitivity.

The dynamics of a CMUT membrane can be modeled by the equations of a uniformly loaded clamped membrane [13]. A powerful technique to analyze the vibrations of a CMUT membrane is the mode superposition method [14], where the total deflection of a membrane is treated as a superposition of different (and orthogonal) vibration modes; it allows the construction of arbitrary motion shapes of the plate with the sum of natural mode shapes weighted by mode participation factors.

A CMUT element containing hundreds of individual cells are actuated in phase to generate enough acoustic power for sufficient depth penetration in tissues. Each of the CMUT cells is modeled considering only the first vibration mode of a membrane [15] as shown in Figure 1.4a. The term *symmetric CMUT* refers to a conventional CMUT with two electrodes (metalized membrane and a bottom electrode) during normal operation, the term is used throughout this document to differentiate from the asymmetric operation mode described in the next section.

### Asymmetric CMUTs

When a nonuniform force is acting on the CMUT membrane, the resulting behavior is the superposition of axially symmetric and asymmetric mode shape components. Asymmetric mode components (Figure 1.4b) exist when a non-axisymmetric force is exerted on the membrane, e.g., a difference in electrostatic forces applied on the left and right part of the membrane during transmission, or a difference in acoustic pressure during reception. Higher order vibration modes similar to the ones shown in Figure 1.5 can exist

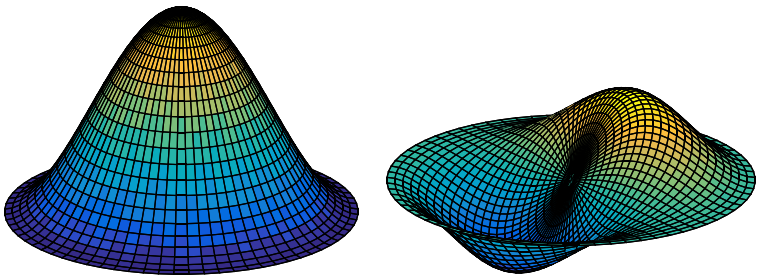

(a) (b)

Figure 1.4: First two natural vibration modes of a CMUT cell. (a) (0,1) mode. (b) (1,1) mode

during the normal operation of a CMUT, but their frequencies are so distant from the fundamental (or first vibration mode) and have so low energy that their contribution to the total membrane deflection can be neglected. The subscripts *(0,1)* and *(1,1)* in the form ($m$,$n$) refer to the number of nodal diameters ($m$) and the number of nodal circles ($n$) of the modes [14].

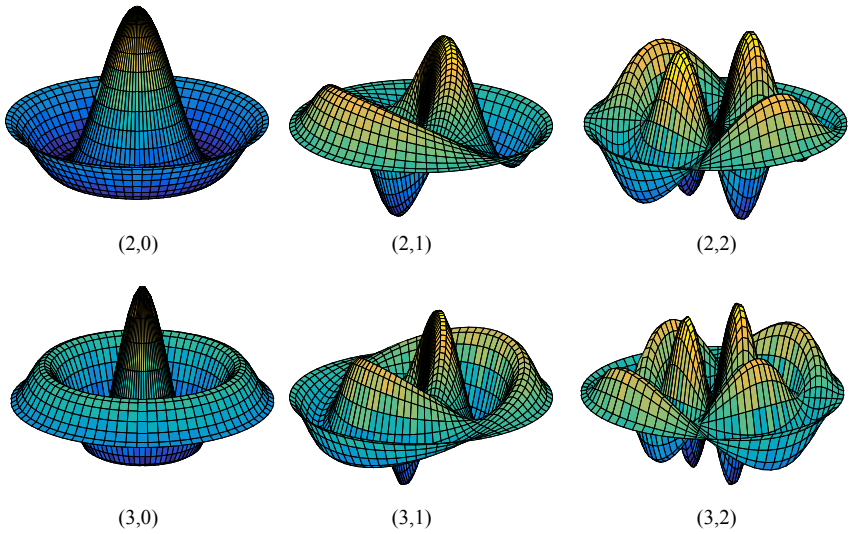


Figure 1.5: Higher vibration modes in a circular membrane.

Higher order symmetric mode components were reported as undesirable dips in the frequency spectrum [16], and higher order asymmetric components were observed as a result of the acoustic crosstalk [17]. Some researchers have exploited the presence of higher vibration modes; for example, in [16], extra load masses are placed on the CMUT membrane to match the frequency of the third mode, and the harmonic signal of this mode is detected using a multi-electrode structure [18] to enable a type of imaging technique called harmonic imaging.

The interaction between the mechanical and acoustical domains can be seen as an exchange of energies. During asymmetric excitation, the exchange of kinetic energy between the parts of the CMUT membrane involves only the near surface fluid and does not radiate significant acoustic pressure [19]. When operating the CMUT in immersed applications, the first vibration mode (symmetric) appears overdamped, producing a wide bandwidth characteristic of CMUTs; however, the second vibration mode (asymmetric) remains underdamped and it is still resonant, where each half of the membrane oscillate in opposite phase with one another.

The potential applications of asymmetric CMUTs have been investigated by former members in our research group, where the relation between the acoustic pressure and the differential signal in the left and right halves of the membrane is exploited to enhance a super resolution algorithm [20]. The authors also proposed the possibility to physically tilt and steer an ultrasound beam to enhance the output transmission power and the sensitivity of a CMUT array [21]. Further applications and planned work will be described later on in this document.

### 1.3.2 Modeling of CMUTs

The energy exchange between the electrical domain, the mechanical domain and the acoustic domain is present during the operation of a CMUT. In order to optimize the design, a critical step is to have a model capturing the dynamics of a CMUT cell in an accurate way. Depending on the purpose, there are different modeling tools available in the literature.

#### Analytical model

A common technique to analyze the behavior of a CMUT is an analytical model. One of the limitations of this kind of model is that it is only useful to analyze the mechanical part of a CMUT, or only a few isolated cases of the interaction between two domains. For instance, some authors have modeled the interaction between the electrical and mechanical domain without accounting the acoustic part [22]. Some others have simplified the electromechanical interaction when analyzing acoustic radiation in water [23]. To the best of the author's knowledge, there is only one work dealing with the mathematical coupling between the electrical, mechanical and acoustic domains [24].

#### Equivalent circuit model

The principle of equivalent circuits is the analogy between the electrical and mechanical domains. Depending on the convention, the forces in the mechanical domain are represented as currents in the electrical domain and the velocities are represented as a voltages [1, 25].

The first reports of equivalent modeling applied to CMUTs follows the

Mason's model [26], where an electrical port, a simple linear transformer and a mechanical port are coupled together to capture the electro-mechano-acoustical interaction. Many others have followed this same approach of modeling [2, 27], where the electrical port includes a capacitor and a resistor, and the mechanical port includes the mechanical impedance, a resistor and a constant acoustic load impedance. This kind of models is called a reduced-order (or small-signal) model because a linearization step is included in its development. In fact, the linear transformer in these models includes the bias ($V_{DC}$) voltage in the transformer ratio, limiting its validity around a fixed operation point.

More complexity has been added to these kinds of models, considering nonlinear effects [28, 29], the position-dependent expression of the capacitance and acoustic impedance [15, 17], taking into account the effect of collapse mode [30], the self-and-mutual acoustic impedance [31, 32], the effect of of different layers and residual stresses in the membrane [33], etc.

Some other models have used lumped parameters to create a macro-model (or large-signal model) [34–36]. These kind of models can capture the non-linearities associated with the normal operation of CMUTs in a more accurate way, such as the spring softening effect, produced when the DC bias voltage induces an increased mechanical tension in the membrane, downshifting the resonant frequency. The description of multiple vibration modes in a CMUT cell have been treated in the past [37], where equivalent circuits connected in parallel are used to describe the orthogonal vibration modes of a CMUT.

The majority of these macromodels can be implemented in SPICE[2] simulators. But there are other ways to implement them. For example in [38], the electromechanical interaction of a CMUT is described using VHDL-AMS code, treating the acoustic interaction as a constant impedance for air and water simulations. This kind of implementation is advantageous in the case where the CMUT and the driving electronics are to be fabricated on the same die, as it allows the complete integrated system to be simulated and gives the ability to optimize the parameters of the CMOS layout of the electronics along with those of the CMUT.

**Finite Element Model**

Another way of analyzing and modeling the behavior of a CMUT is with a Finite Element Model (FEM), where a software program computes the partial differential equations in each of the geometric divisions of the object (the finite element). This kind of modeling is the closest to the physical reality and produces the best results, but at the expense of long computational time and expensive simulation software.

Modeling with FEM has been done to calculate static and harmonic characteristics such as collapse voltage and resonant frequency [39], as well as dynamic behavior in immersion [40]. Some recent works employ a combination of two or more modeling techniques to produce high accuracy models. For example, [28] derives a 1-D model of fluid-loaded CMUTs from FEM simulations.

[2]Simulation Program with Integrated Circuit Emphasis

### 1.3.3 Fabrication techniques

The early stages of a CMUT dates back to 1990, when a research group created the first version of a Capacitive Ultrasonic Transducer by brushing a brass backplate with conventional tools to act as a bottom electrode and stretched a metallized membrane on top to act as top electrode [41]. The produced frequencies at that time were in the order of kHz, and one of their applications was as position sensors for robotic arms.

A few years later, similar versions of these transducers were developed using micromachining techniques. Cavities were created on silicon wafers to later stretch flexible dielectric films (such as kapton, mylar, or polyester) with a metallized area to act as top electrode [42, 43]. Using bulk micromachining techniques allowed them to obtain small features in the order of hundreds of micrometers in the cavities, enabling them to reach the MHz range. However, the main drawback of these approaches was that the controlability of the gap between the two electrodes was so poor that it did not allow them to produce transducers with uniform properties; moreover, they could not be vacuum sealed and experienced squeeze-film damping attenuation problems.

The first fully micromachined capacitive ultrasonic transducers were built in 1994 [27] and were called capacitive micromachined ultrasonic transducers (CMUTs). They used a sacrificial release process that has become the standard fabrication method for CMUTs. The cavity underneath the membrane is created by depositing or growing a sacrificial layer; once the material deposition for the membrane is done and some releasing holes are

patterned, the sacrificial layer is removed with an etchant, specifically chosen to remove the sacrificial material without damaging the membrane nor the substrate. Even though the fabrication process remains almost the same, the variation of materials and process controls makes a difference in the design and overall device yield.

Depending on the highest temperature used in the fabrication process; the fabrication methods can be classified as low temperature and high temperature [44]. If the CMUTs and the CMOS electronic circuitry share the same silicon substrate, the highest temperature throughout the process cannot exceed 400°C. Such a low temperature process allows the integration of CMOS devices within the same die (see for example [45]) and are called CMOS–compatible. All other types are simply called high-temperature processes.

There is a relatively new fabrication technique called wafer-bonding; it is based on a different approach to create the cavity using a combination of bulk and surface micromachining techniques [46]. In this approach, the membrane and cell cavities are deposited and patterned on separate wafers and fusion-bonded in a vacuum environment. Wafer-bonding simplifies the process, reduces the number of steps and the turn-around time, eliminates problems with membrane release processes, high stress, and porous films, and increases the yield, uniformity, and process control [44]. Nevertheless it requires high temperatures (1100°C) during the bonding mechanics [47].

In CMUTs, a high electromechanical coupling coefficient ($k$) leads to higher transducer sensitivity, improved bandwidth and therefore improved image resolution [48]. Efficiency levels reported for CMUTs can be as high

as 82% [49]. The wide bandwidth for CMUTs is also the inherent result of the CMUT cell structure; the thin membrane clamped at the rim has a low mechanical impedance, which facilitates better acoustic matching to the medium [50].

In an ultrasonic transducer array, the parasitic capacitance of the interconnect between an array element and its electronics is a limiting factor for the dynamic range and frequency bandwidth [51]; moreover one of the main problems in fabricating two-dimensional CMUT arrays is the addressing of the individual array elements [52]. A way to overcome these problems is to have the driving circuitry as close as possible to the CMUT array. A fabrication technique developed in 2001 called through-wafer interconnection addressed both of the problems; it basically adds an extra step to the wafer-bonding technology where through-wafer interconnects are preprocessed onto the silicon substrate before creating the CMUT using a bulk silicon micromachining process [51].

Fabrication techniques involving other materials and processes different from the conventional ones have been reported. For example, the fabrication of flexible CMUT arrays [53, 54]; or polymer-based CMUT fabrication for biocompatible applications [55, 56].

This polymer-based fabrication approach in particular, offers certain advantages, such as rapid fabrication, low cost and the possibility to be fabricated on flexible substrates. Nevertheless the reported operational voltages in [55], [56] were in the order of hundreds of volts, making them less attractive to be used in biomedical ultrasound industries [57].

### 1.3.4 Applications of CMUTs

CMUTs have the potential for improving certain imaging applications due to the flexibility of transducer geometries, suitability for high frequency imaging of small structures such as the eye, and space-limited applications such as intravascular ultrasound (IVUS). Fabricating such small devices using piezoelectric crystals would be technologically challenging.

Because large CMUT arrays can be lithographically defined and integrated with front-end electronics, they offer special advantages over piezoelectric arrays in building matrix arrays for 3D imaging applications; with experimental results reported in [58] and [59].

Due to their small size, CMUTs can be fabricated in arrays of different sizes and geometries, suitable to be mounted at the tip of a catheter for intravascular and intercardiac applications. Foward-looking ring arrays have been build and tested in [60] and [61]. CMUTs have also been used for therapeutic purposes such as High Intensity Focused Ultrasound (HIFU) [62] and [63]. CMUTs have also been employed in a pioneering super-resolution technique for biomedical applications [20].

Apart from biomedical applications, CMUTs have also been used in the area of gas sensing [64], fluid property sensing [65], non-destructive tests [66] and airborne applications [67].

An emerging section for ultrasound applications are the so-called conformal transducers, where transducer arrays are fabricated on flexible substrates attempting to be placed in contact with curved body surfaces (e.g. abdomen, neck) to provide a natural beam focusing. Several prototypes

have been fabricated [68], [69], nevertheless they reported interconnection problems during bending tests.

### 1.3.5 Disadvantages of CMUTs

Despite the fact CMUTs offer mayor advantages over their piezoelectric counterparts, they also have some important drawbacks. The main problem for CMUTs it the output power, which thereby reduces the SNR and penetration depth into tissues [70] and in turn degrades the sensitivity in reception. This has been tested experimentally [71, 72], obtaining 10dB less sensitivity for CMUT-based ultrasound probes compared to piezoelectric ones. Similar results regarding the penetration depth were obtained by Legros et. al. [73]; nevertheless, the CMUTs outperformed piezoelectric probes in terms of the signal-to-noise ratio when phased-array steering was used; this was attributed to the larger acoustic radiation field experimentally measured from CMUTs.

A way to increase the output acoustic power in a CMUT cell is to operate it in collapse mode, where the CMUT membrane is brought to contact with the substrate by a voltage beyond its pull-in voltage, and released to emit higher power, but frequent membrane-substrate contact causes issues with operation stability and reliability [18]. This approach was experimentally characterized [74] and theoretically analyzed [75], and an equivalent circuit was built for its analysis [76]. The output pressure can be also improved by adding an extra mass on the center of the membrane [77, 78]. Another option to improve the output pressure and the receiving sensitivity is to create non-conventional CMUT structures, such as dual-electrode structures

[18, 79], that uses separate electrodes for transmission and reception. In transmit, the membrane is biased by the electrodes close to the edges to increase the membrane deflection, and hence the output pressure; in receive, the center electrode pulls the membrane down to increase the receiving sensitivity.

A recent approach to increase the sensitivity is to use a so called $M^3$-CMUT, where a stack of two deflectable membranes are suspended over a fixed bottom electrode [80]. In this configuration, the two moving membranes deflect simultaneously in response to a bias voltage, which results in a smaller effective cavity height compared with the conventional capacitive transducers. Some others works attempt to increase the sensitivity of the CMUTs by having a concave bottom electrode to increase the total effective capacitance of the device [53].

When CMUTs are fabricated using polymer materials, because of the low density, their membranes are much thicker than the ones fabricated using polysilicon or silicon membrane. Since the top electrode is typically patterned above the membrane, large actuation voltages in the order of hundreds of volts are needed for actuation [81–83], which can be a potential barrier in human ultrasound imaging [57].

CMUT transducers also suffer from acoustic crosstalk, which is undesired acoustic interactions between membranes in fluid-couple operations. This crosstalk contributes to image degradation caused by Stoneley waves at the membrane-water interface and Lamb waves propagating in the substrate [84]. Work has been done to analyze and tackle this side effect [85, 86].

## 1.4 Integrating CMUTs with imaging systems

The CMUT probes including the transducer array and the front-end electronics are often built and packaged in-house for different applications, and are integrated into the imaging system where a control unit with the beamforming information, and the processing unit for the received signal are included.

The integration of CMUTs with front-end electronics presents a challenge given that it is the first input port of information, where signal-to-noise ratio (SNR) levels are important. In array operation, the parasitic capacitance of the interconnect between an element and its electronics is the limiting factor for the dynamic range and frequency bandwidth; therefore, it is preferred to have the electronics as close to the array elements as possible [51]. For piezoelectric 2D arrays, a considerable sacrifice in the element area is required if an individual addressing is needed. The advantage of CMUTs in this respect is the fabrication of 2D arrays using through-wafer interconnections [51] or trench-isolated interconnects [87], where individual CMUT cells can be electrically accessed from the back side of the substrate. Another method is to use low-temperature processes that allow the fabrication of CMUTs directly above pre-existing components such as amplifiers and beamformers [88].

## 1.5 Hypotheses and potential benefits

Considering the background of CMUTs in regards of modeling, fabrication and integration with electronics; we identified our basic hypotheses for this

project described below.

Among all the different ways to increase output power (and therefore the sensitivity and the SNR) in CMUTs mentioned in section 1.3.5, we believe that by using alternative fabrication materials we can enhance the performance of CMUTs at the same time as reducing the manufacturing costs. We also believe that the performance can be measured with accurate analytical models.

A great majority of the mathematical models for CMUTs are considered linear models since they use linear electric components for simulations. These non-linear devices require an accurate model in order to capture the rich dynamics in the electro-mechano-acoustical interaction; especially when analyzing asymmetric CMUTs.

As an extra possibility; we want to explore if it is possible to fabricate passive electronic devices (R, L, C) using the photopolymer SU-8. We believe that the electrical and mechanical properties of this polymer can be controlled by the addition of fillers, still maintaining its photopolymerization capabilities.

Therefore, we have identified three related potential benefits that can be integrated together to improve the performance of current CMUTs. These ideas will potentially solve a series of problems and open new opportunities in ultrasound imaging.

### 1.5.1 Development of multi-vibration mode large-signal model

As mentioned in section 1.3.2, equivalent circuit models are useful to capture the electro-mechano-acoustic interactions of CMUTs in an accurate way without the computational implications of FEM models. A detailed insight of the interactions between energies in symmetric and asymmetric CMUTs during transmission and reception can help us to optimize future designs and validate current theories regarding asymmetric CMUTs. There are only a few works dealing with higher vibration modes for CMUT membranes [89], [37], however, none of them can capture the energy interactions in asymmetric CMUTs.

Resonant sensors are considered very sensitive devices, because any subtle change in the resonant frequency can be easily detected [90]. The resonant nature of the asymmetric mode in water might have new applications such as sensing the variation in viscosity of fluid close to the membrane.

Equivalent circuit models offer a combination of analytical models without the time constrains of the FEM models. The problem is that many of these equivalent circuit models are based on early concepts following Mason's approach [26], which are considered linear models valid only around a fixed operational point. If we want to exploit the potential applications of asymmetric CMUTs discussed in section 1.3.1, it is imperative to have a model that can accurately capture their dynamics. The ongoing efforts to develop this model will be further discussed in section 2.2.

### 1.5.2 Rapid low cost fabrication of prototype transducers

The costs associated with the fabrication of silicon chips in a cleanroom environment can be expensive [91]; and taking into account that almost all of the current CMUT research groups use silicon as the fabrication material, a way to decrease these prices will be a breakthrough for the entire CMUT community. In order to reduce the fabrication costs per chip using cleanroom technologies, it is necessary to either use cheaper fabrication alternatives or mass produce them. A less expensive alternative is to use multi-user wafer fabrication processes such as PolyMUMPs, in which multiple users share a small area on a wafer run though fixed fabrication steps [92]; however the fabrication steps cannot be personalized and only a few fabrication runs are scheduled each year.

A silicon chip design is cost-reliable when mass produced; for example, MEMS devices such as pressure sensors or accelerometers have low commercial prices because of the millions of units fabricated every year. Many organizations forecast MEMS sensor volumes to exceed trillions by 2022 [93]; nevertheless this is not the prediction for ultrasonic transducers.

To create a perspective, the global ultrasound market was valued at $4.6 billion in 2012, and it is forecasted to exceed $7 billion by 2019 according to a report published in 2013 [94]. The average price of a single piezoelectric-based ultrasound system is about $115,000 USD [95]. Even though piezoelectric transducers dominate the current ultrasonic industry; commercially available CMUT-based ultrasound systems have started to emerge [9], [10], and several large corporation manifested their interest in

CMUT-based transducers [69], [68].

An inexpensive yet sensitive transducer could be a disruptor in the ultrasound industry, being able to widespread the use of ultrasound imaging even broader. One of the final goals of this project is to fabricate high-sensitive and low-cost CMUTs, using alternative microfabrication technologies taking advantage of the unique equipment present in the Microsystems and Nanotechnlogy (MiNa) laboratory. A few of the potential benefits of using these alternatives are to be able to manufacture large area CMUT arrays, the ability to create CMUT arrays on flexible substrates and much faster fabrication times. All these advantages will be further described in chapter 4.

### 1.5.3 Capability for a hybrid integration

A seamless integration of electronic components and CMUTs can be done if both can be fabricated at the same time. We will explore the idea of using the same fabrication materials as CMUTs to create electronic components. We plan to do this by modifying the physical properties of the materials using filers in the nanometer scale.

Parasitics arising from interconnecting paths between CMUTs and electronics decrease the overall SNR; this is especially true for 2D arrays for 3D imaging, where electrical routing is an issue. The performance of CMUTs might be boosted if interconnection lines and potential electronic components can be fabricated on the same substrate and as close as possible to the CMUTs using similar fabrication materials; especially when dealing with small footprint designs. This concept could be then extrapolated to flexible

substrates for portable applications; sharing the vision of some researchers about having a portable and flexible ultrasound systems as described in [69], [68].

## 1.6 Contribution and structure of the thesis

This thesis explores the idea of simulation, design, fabrication and characterization of capacitive micromachined ultrasound transducers fabricated using polymer materials (polyCMUTs). In chapter 2, the analytical model, finite element model and equivalent macromodel for a symmetric CMUT is developed. Chapter 3 expands this modeling theory to asymmetric CMUTs. In chapter 4, the fabrication and characterization of the first working and sealed polymer-based Capacitive Micromachined Ultrasound Transducer (polyCMUT) is presented, and the first B-mode image in the world using an array polyCMUTs is shown. Chapter 5 investigates the idea of enhancing technology (photopatterning) to create a functional (conductive) SU-8 to fabricate passive components on flexible substrates for the potential integration with polyCMUT arrays. Future work involving the fabrication of polyCMUTs on flexible substrates is discussed in Chapter 6.

# Chapter 2

# Equivalent circuit macromodel for CMUTs

As introduced in chapter 1, there are several ways to model the dynamics of CMUTs. Equivalent circuit models offer a combination of analytical models without the time constrains of the FEM models. The problem is that many of these equivalent circuit models are based on early concepts following Mason's approach [26], which are considered linear models valid only around a fixed operational point. This chapter proposes a non-linear equivalent circuit model based on energy-flow theory that is valid under any kind of excitation voltage.

## 2.1 CMUT modeling problem

The principle of equivalent circuits is the analogy between the electrical and mechanical domains. Depending on the convention, the force in the mechanical domain is represented as current in the electrical domain and the velocity is represented as a voltage [1, 25].

### 2.1.1 Mason model (MS)

Mason-like models similar to the one depicted in Figure 2.1 are widely used. The straightforward implementation and physical interpretation of these models makes them attractive for simulation, as they can be easily implemented in ordinary SPICE simulations. Nevertheless, Mason-like models couple the electrical and mechanical domains using a linear transformer, having the $V_{DC}$ bias voltage in the expression of its turns ratio. This linear behavior makes it valid only nearby a fixed operational point. This means that it is necessary to have *a-priori* information about the input signal, therefore, an arbitrary waveform with large variations in the DC component cannot be directly applied to the model without diverging from the operational point.

The general structure of a Mason model is depicted in Figure 2.1. In this linear model, the through and across variables are velocities and forces, represented as electrical voltages and electrical currents respectively. $C_E$ represents the electrical capacitance of the CMUT, $n$ is the transformer ratio given by the expression $n = U\varepsilon_0 A/(d_{\text{eff}} - w_q)^2$ (see Figure 2.8), $L_M$ is the membrane mass, $C_M$ is the spring constant and the negative capacitor $-C_E/n^2$ models the effect of spring softening. The electric impedance $Z_R$ captures the mechano-acoustical interaction between the CMUT membrane and the medium. The full details of this kind of model can be found in [48].

A disadvantage of Mason's model, is that it needs the deflection of the membrane for a given DC bias voltage as an input to accurately calculate the electrical parameters of the model [48], especially for the transformer's

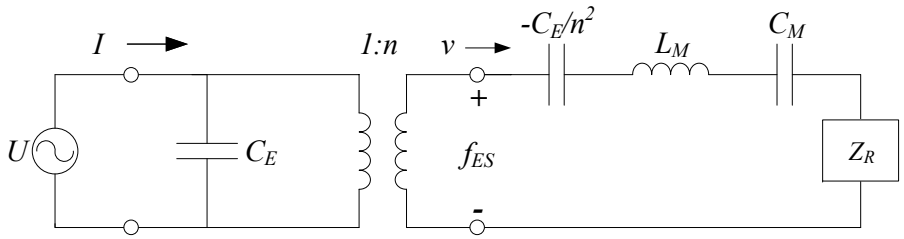


Figure 2.1: Typical Mason-like model. The electrical domain (left portion of circuit) is coupled to the mechanical domain (right) using a linear transformer. The acoustic interaction is done through the impedance $Z_R$

ratio. Another disadvantage of Mason's model is that it does not accurately capture the behavior of CMUTs when there is no DC bias voltage (pure AC). Since the electromechanical coupling is done though a linear transformer, the electrostatic force does not oscillate at twice the input frequency. Moreover, because of this linearity, this model cannot be used to predict the pull-in voltage of CMUTs, as the membrane deflection keeps increasing proportionally to the input voltage.

## 2.2 Equivalent circuit model of CMUTs

What is needed is a model that can capture the non-linearities associated with the operation of CMUTs without unduly raising complexity of implementation or computation. A large-signal model based on energy flow theory that includes the nonlinearities of CMUTs in the constitutive equations is proposed. This macromodel can also be complemented with system-level simulations; where the interactions involving the final device as well as driving circuitry such as voltage amplifiers and filters are often neglected

[96].

For the derivation of the proposed equivalent circuit model, we used the energy exchange point of view described in [1], where the different vibration modes of a membrane in a MEMS device are expressed by different subcircuits. Each sub-circuit has an electrical port and a mechanical port, and follows a typical MEMS parallel-plate equivalent circuit model with the following constitutive equations:

$$i = \frac{d}{dt}Q = \frac{d}{dt}CU = \underbrace{C(q)\frac{dU}{dt}}_{I_{CE}} + \underbrace{U\frac{dC(q)}{dq}v_q}_{I_{RE}} \tag{2.1}$$

$$f_q = -\frac{1}{2}U^2\frac{dC(q)}{dq} \tag{2.2}$$

The general structure of this equivalent circuit model is depicted in Figure 2.2, where $q$ is the displacement[3] of the membrane, and $C(q)$ is the electrical capacitance of the CMUT cell. The electrostatic input of the circuit is represented by two pairs of across-through variables $(U, I)$ and $(f_q, v_q)$, $U$ and $I$ are the across (voltage) and through (current) variables at the electrical port (left portion of the circuit). On the mechanical port (right side) we have $f_q$ and $v_q$, representing the force and velocity acting on the membrane.

The novelty in these equations is that the membrane velocity ($v_q$) appears intrinsically in Eq. (2.1). Given that the capacitance is dependent of the deflection $w_q$, the membrane velocity $v_q$ appears after performing the

[3] $q$ can be replaced with any other variable $(x, y, z)$ depending on the displacement direction; $q$ is treated here as general displacement direction following [1]

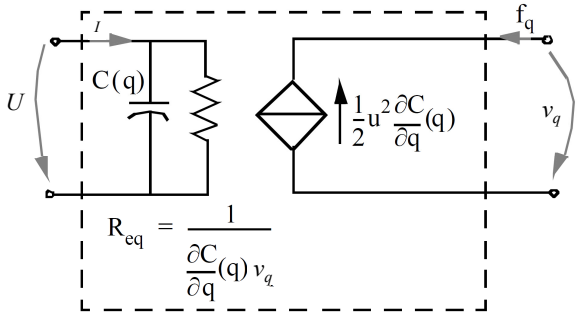


Figure 2.2: Basic parallel-plate equivalent circuit model [1]. With permission from the author.

derivative of the capacitance $C(q)$ with respect to time.

### 2.2.1 Parallel-plate model (PP)

Following a similar approach as in [89], we obtained the equivalent circuit model of a CMUT as shown in Figure 2.3.

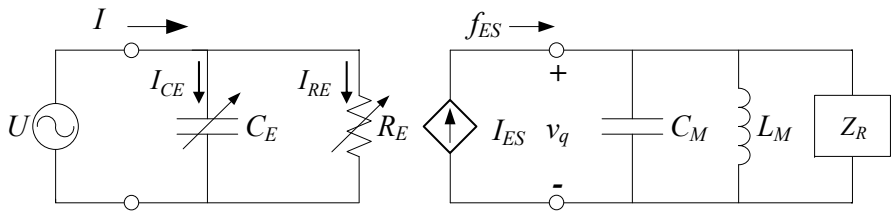


Figure 2.3: Mode equivalent circuit of a single cell CMUT. The electrical domain (left portion of circuit) is coupled to the mechanical domain by a dependent current source $I_{ES}$, representing the electrostatic force.

Eq. (2.1) represents the sum of the electrical currents present during the operation of a CMUT cell. The first term in this equations captures the electrical current flowing though the CMUT ($I_{CE}$), and it is modeled using

the variable capacitor $C_E$ on the electrical side, its value is given by:

$$C_E(q) = \frac{A\varepsilon}{d - w_q} \tag{2.3}$$

where $A$ is the area of the CMUT membrane, $\varepsilon$ the permittivity and $w_q$ is the membrane deflection.

The variable resistor $R_E$ on the left side of the circuit is derived when the input voltage $U$ is divided the second electrical current (second term) in Eq. (2.1). This resistor represents the energy that is being dissipated on the electrical domain and is being transferred to the mechanical domain; its value is given by:

$$R_E = \left(\frac{d}{dq} C_E(q) v_q\right)^{-1} \tag{2.4}$$

where $v_q$ is the membrane velocity. The dependent current source $I_{ES}$ on the mechanical side models the electrostatic force acting on the CMUT membrane; and is represented by:

$$I_{ES} = -\frac{1}{2} U^2 \frac{d}{dq} C_E(q) \tag{2.5}$$

The parallel equivalent capacitance $C_M$ is related to the equivalent mass of the membrane:

$$C_M = \rho_p h A \tag{2.6}$$

where $\rho_p$ and $h$ are the density and the thickness of the membrane respectively.

The parallel equivalent inductor at the mechanical port represents the spring constant ($k_q$) of the membrane, and is related to the in-vacuum resonant frequency $\omega_R$, calculated using the analytical formulas from [97]:

$$L_M = \frac{1}{k_q} = \frac{1}{\omega_R^2 C_M} \tag{2.7}$$

The radiation impedance from the medium acting on a CMUT cell is calculated following the results from [98]. The normalized radiation impedance in function of the dimensionless factor $ka$ is shown in Figure 2.4, using the equations:

$$\begin{aligned} Z_R &= \left[1 - \left(\tfrac{192}{(2ka)^5}\right)\left(F_1\left(2ka\right) + i \cdot F_2\left(2ka\right)\right)\right] \rho_m c A \\ F_1\left(y\right) &= \left(20 - y^2\right) J_1\left(y\right) - 7y J_0\left(y\right) - 3y \\ F_2\left(y\right) &= \left(y^2 - 20\right) H_1\left(y\right) + 7y H_0\left(y\right) - \tfrac{2y^2}{3\pi} \end{aligned}$$

where $c$ is the speed of sound and $\rho_m$ is the density of the medium, $J_0$ and $J_1$ are Bessel functions of the first kind of order zero and order one respectively, and $H_0$ and $H_1$ are Struve functions of the first kind of order zero and order one respectively.

In Figure 2.4, the real part corresponds to the real power radiated into the medium, whereas the imaginary part represents the energy stored in the medium due to the sideways movements of the medium in close proximity of the membrane [17].

Table 2.1 shows a direct comparison between the parameters of Mason-like models and the ones presented in this section. Electrical elements in Mason model are implemented as elements in series in the proposed model.

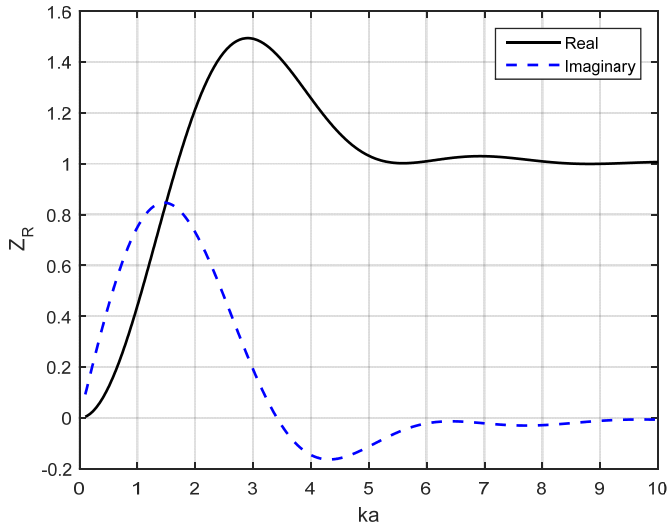


Figure 2.4: Simulated normalized radiation impedance for a single CMUT membrane clamped all-around.

### 2.2.2 Deflected Membrane model (DM)

It has previously been investigated that higher vibration modes are present at all times during the vibration of CMUT membranes, these modes can arise either from electrical excitation or from the mechano-acoustic interaction during receiving mode. A powerful technique known as the mode superposition (or mode participation) method [14] can be used to analyze the vibrations modes and deflections of a CMUT membrane. In this method, the total membrane deflection is treated as a superposition of different (and orthogonal) vibration modes; it allows the construction of arbitrary motion shapes of the plate with the sum of natural mode shapes weighted by scalar coefficients known as mode participation factors ($F_m$). The deflection of a circular and fully clamped membrane can be described by the equations:

Table 2.1: Equivalence between the variables used in Mason's model and this model

| **Parameter** | **Mason** | **This model** |
|---|---|---|
| Forces | Voltages | Currents |
| Velocities | Currents | Voltages |
| Electrical capacitance | $C_E$ | $C_E$ |
| Membrane Mass | $L_M$ | $C_M$ |
| Membrane Spring constant | $C_M$ | $L_M$ |
| Fluid loading | $Z_R$ | $1/Z_R$ |

$$w = \sum_{m,n} F_m \psi_m (r, \varphi) e^{-i\omega t} \tag{2.8}$$

$$\psi_m(r, \varphi) = \cos(m\varphi) \left[ J_m \left( \frac{\lambda_{mn}}{a} r \right) - \frac{J_m(\lambda_{mn})}{I_m(\lambda_{mn})} I_m \left( \frac{\lambda_{mn}}{a} r \right) \right] \tag{2.9}$$

where $a$ is the membrane radius, $\psi_m$ is the characteristic function that represents the $m^{th}$ natural mode of the membrane and $\lambda_{mn}$ is a dimensionless factor found in [97]. $J_m$ is the Bessel function of the first kind of order $m$ and $I_m$ is the modified Bessel function of the first kind and order $m$.

The Bessel functions included in the calculation of the membrane deflection equation (2.9) cannot be directly implemented in ordinary SPICE simulators. Because of this, we explored a further simplification of the equations involved in the model. The RMS deflection of the membrane was used to calculate the capacitance and the CMUT was treated as a parallel-plate capacitor. In this way, the Bessel functions invoked in (2.9) are no

Table 2.2: Simulation parameters

| **Parameter** | **Value** |
|---|---|
| Membrane radius ($a$) | 50$\mu$m |
| Membrane thickness ($h$) | 7.31$\mu$m |
| Cavity height ($d_0$) | 0.30$\mu$m |
| Membrane material | SU-8+Cr+Parylene-C |
| Equivalent flexural rigidity ($D$) | 1.78e-7 Pa·m$^3$ |
| Separation between electrodes ($d_{\text{eff}}$) | 0.97$\mu$m |
| Medium density ($\rho_m$) | 1000 Kg/m$^3$ |

longer necessary. This simplified version of the proposed model can be implemented in ordinary SPICE simulators; providing a simple yet realistic modeling of symmetric CMUTs. Figure 2.5 shows the simulated membrane deflection profile for the two approaches aforementioned (DM and PP). The central portion of the membrane in the DM model gets closer to the bottom electrode; whereas the areas closer to the rim get much less deflected. It will be shown that the parallel-plate implementation provides a reasonable approximation when compared to FEM and experimental results.

In this chapter, we focus our attention on the first vibration mode (fundamental) since it radiates acoustic power into the far field whereas higher modes only exchange energies locally [99]. The potential applications of higher vibration modes will be described in Chapter 3.

## 2.3 Simulations and experimental results

The deflected membrane model (DM) using equations (2.8) and (2.9) was implemented in MatLab-Simulink (Natick, Massachusetts, USA). The cir-

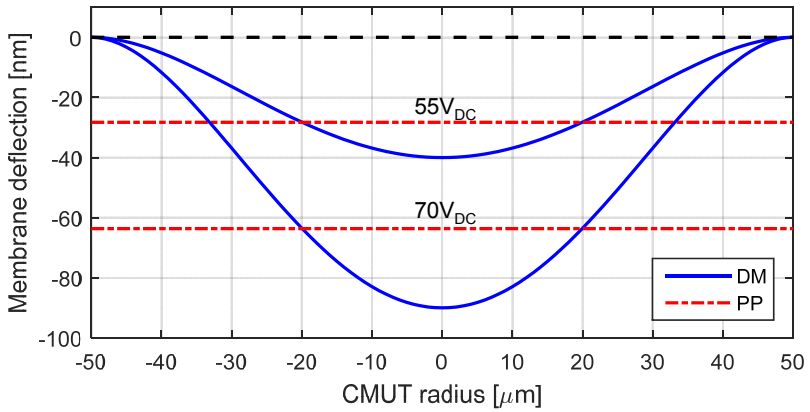


Figure 2.5: Membrane deflection profiles simulated for modes DM and PP under different bias voltages.

cuit implementation is shown in Figure 2.6. An embedded function had to be added to compute the membrane deflection using the modal participation theory, calculating the membrane deflection at each time step. The implementation of the equivalent macromodel circuit shown in Figure 2.3 corresponding to the parallel-plate approach was simulated in Multisim 13.0 (National Instruments, Austin, TX, USA); using virtual elements such as voltage-controlled capacitors and voltage-controlled resistors. For comparison purposes, an FEM model was created in Comsol Multiphysics (Comsol Inc., Burlington, MA, USA) and is shown in Figure 2.7, the CMUT cell sits on an infinite baffle surrounded by a water sphere with boundary conditions set to radiate spherical waves. For all the simulations, the parameters used are indicated in Table 2.2 and are further explained in section 4.4.

The physical CMUT cells were fabricated using a technology developed by our group and detailed in section 4.4. The CMUT cells were fabricated

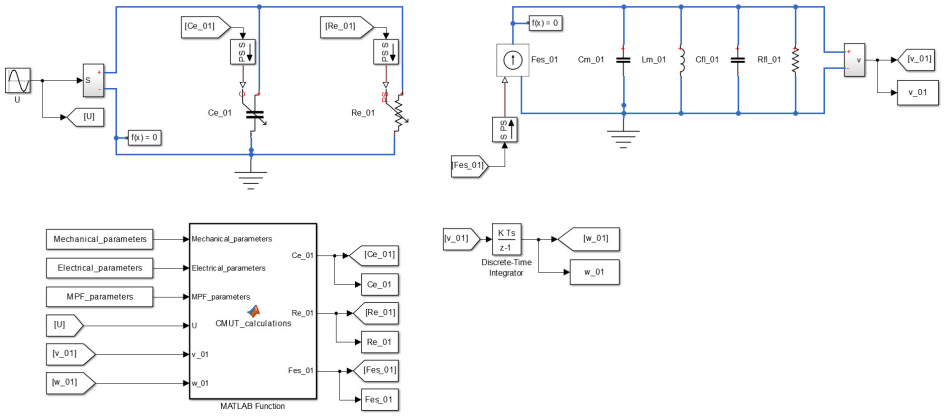


Figure 2.6: Implementation of the DM model for symmetric CMUTs in Matlab-Simulink, a script containing the implementation with Bessel functions is located in the subsystem at the lower-left corner.

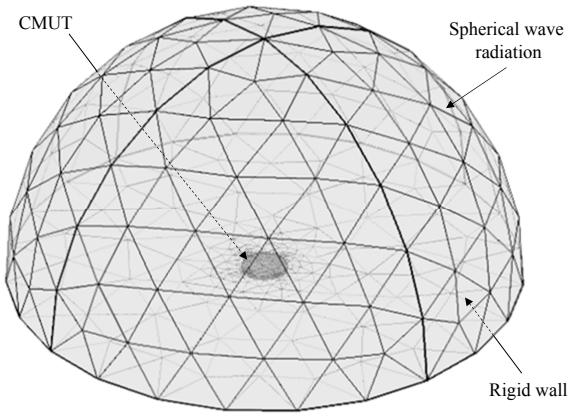


Figure 2.7: Model in Comsol of a single CMUT immersed in water. The membrane sits on an infinite baffle modeled by sound rigid walls. A semisphere with boundary conditions set to radiate spherical waves captures the effect of fluid loading.

using the photosensitive polymer SU-8. The membrane contains a metal electrode embedded between two layers of SU-8 as shown in Figure 2.8.

The purpose of this design is to keep the operational voltages low while still achieving the MHz operating frequency for biomedical ultrasound applications. The complete fabrication process is described in chapter 4.

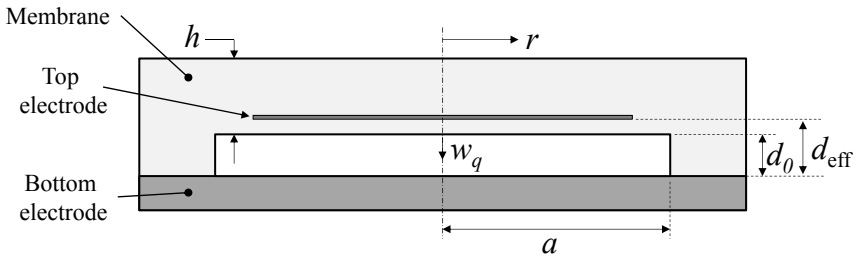


Figure 2.8: Diagram of the described polyCMUT, the top electrode is purposely embedded in the membrane to decrease the effective gap between electrodes.

Given that the physical membrane is fabricated using a stack of SU-8, chromium and parylene-C, we followed the methodology outlined in [100] to obtain the equivalent flexural rigidity ($D$) of the layered membrane.

### 2.3.1 Sine excitation

As mentioned in section 2.1.1; Mason-like type of models offer a quick implementation and are a useful tool to simulate CMUTs around a fixed operational point. For comparison purposes, a Mason model (MS) shown in Figure 2.1 was simulated using the same parameters for membrane mass, spring constant and radiation impedance. Figure 2.9 shows the effect of biasing Mason models under different voltages and compared to the proposed model. The membrane deflection gets amplified as it gets close to the pull-in voltage around 75V. All models agree at small DC bias voltages. The de-

flected membrane model (DM) captures the effect of capacitance variation in a more accurately way than the parallel-plate model (PP).

Another advantage of the proposed macromodel is that it captures the behavior of a CMUT cell under any kind of voltage without linearizing the circuit around an operating point as the Mason's model [26] does. The model is still valid even without a DC bias voltage applied, where the induced electrostatic force oscillates at twice the input frequency. Figure 2.10 shows the output of the system when a sinusoidal signal is applied without DC bias. This is an important contrast between the proposed model and Mason's model, where the electrostatic force maintains the same frequency as the input voltage regardless of the bias voltage applied.

### Frequency response

The experimental measurements were performed using a laser Doppler-vibrometer (LDV) OFV-5000 (Polytec, Irvine, Ca, USA). Figure 2.11 shows the comparison between the frequency responses of a CMUT cell operating in air. The normalized frequency response from the DM and PP models overlap. FEM simulations reveals that the proposed model captures the frequency behavior of the membrane in a very accurate way. The resonant frequencies of the simulated model (2.86 MHz) and the FEM results (2.88 MHz) stayed within 1.5% of the resonant frequency (2.84 MHz) measured experimentally. The FEM simulations presents a sharper resonant peak; this is because the damping from the fluid has less effect on the CMUT membrane in FEM simulations.

Figure 2.12 shows the frequency response of the CMUT cell operating

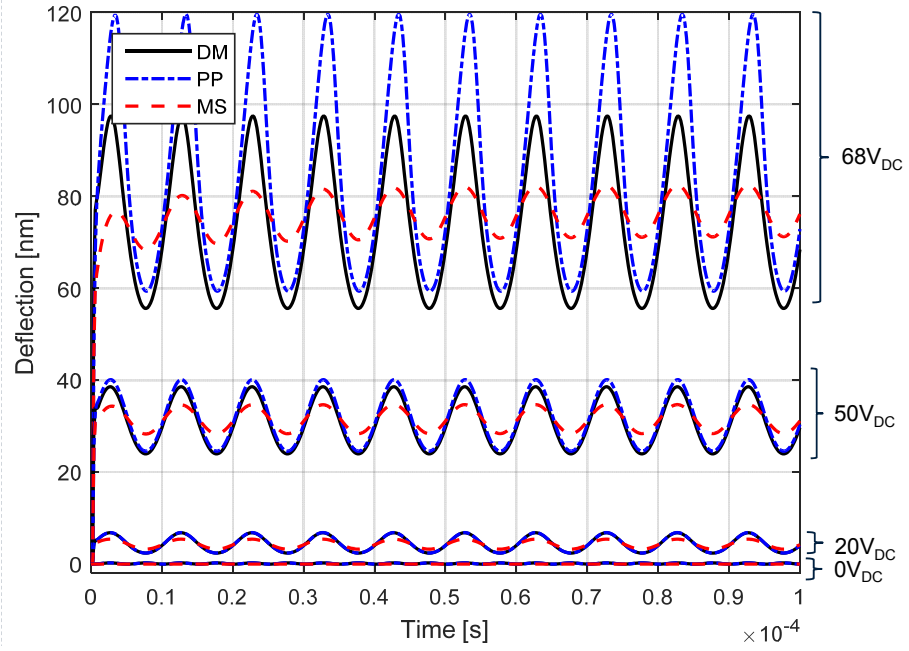


Figure 2.9: Simulated variation in the membrane deflection as the DC bias voltage is increased. The linear behavior of Mason model does not capture in an accurately way the membrane deflection at high voltages, where it gets amplified closer to pull-in.

in water. Because of the fluid loading, the simulated resonant peak is now located at 1.24MHz; very close to the resonant frequency measured experimentally (1.23 MHz). FEM simulations reveals a peak around 1.38 MHz; this discrepancy is likely caused by the boundary conditions specified in simulation, where the generated acoustic waves are set to radiate to infinity. The non-smooth shape of the frequency response measured experimentally is attributed to measurement artifacts, involving reverberations from the air-water boundary [101]. An extended discussion on this is presented in section 3.4.

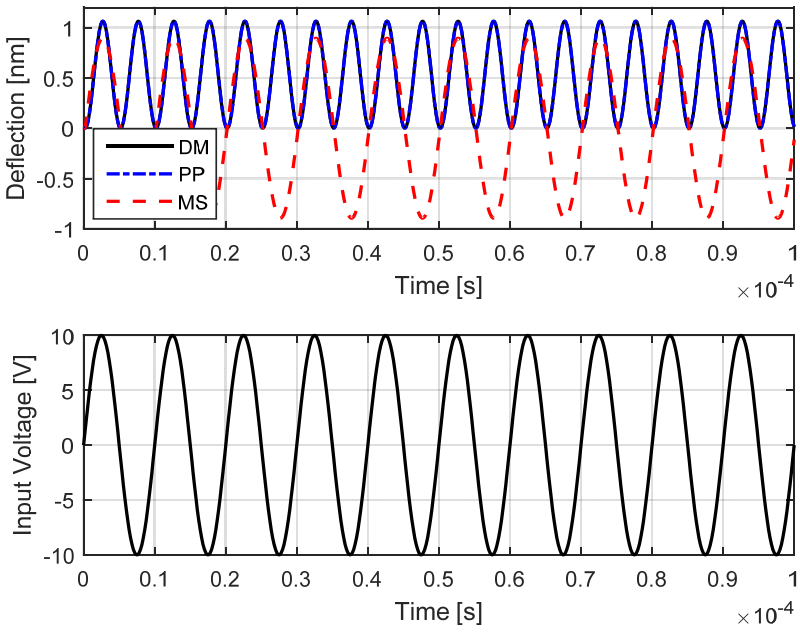


Figure 2.10: Simulated sinusoidal excitation of CMUTs without DC bias (pure AC). Using the proposed models (DM and PP), the membrane deflects at twice the input frequency as expected whereas Mason's model incorrectly follows the input frequency.

### Spring softening effect

The spring softening effect in CMUTs occurs when the DC bias voltage attracts the metalized membrane towards the bottom of the cavity. Since the two electrodes are now closer together, the electrostatic force increases in magnitude. The increase in this force can be interpreted as a decrease of the spring constant (decrease in frequency). The proposed macromodel can capture the non-linearities associated with the spring-softening effect in an accurate way.

Figure 2.13 shows the frequency response in air of the system when the

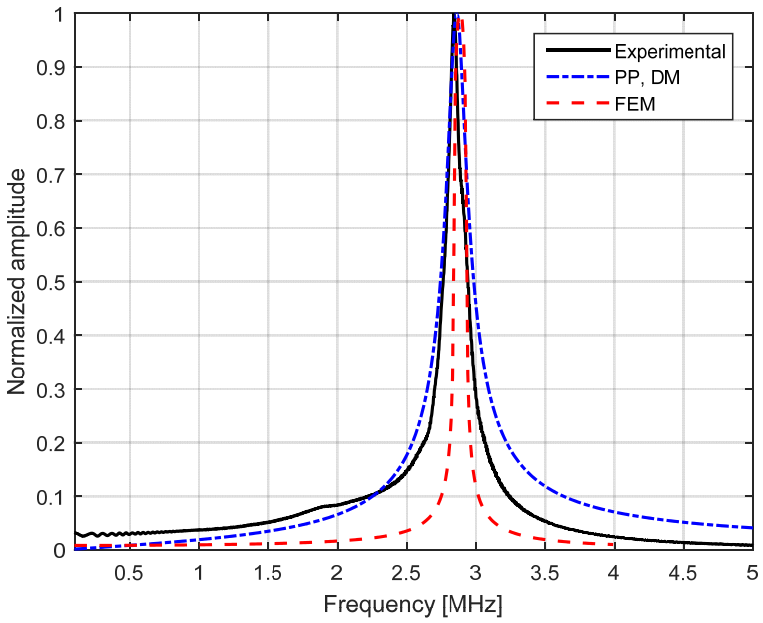


Figure 2.11: Comparison of the normalized frequency response of CMUTs with symmetric excitation in air.

bias voltage is increased closer to pull-in. The system is able to cope with large variations in the DC component "on the fly"; this contrast with the fact that the bias voltage is part of the transformer's ratio in Mason model.

### Pull-in detection

The mechanical stiffness of the membrane resists the effects of the electrostatic force acting on it. As the applied voltage increases, it reaches a point where the electrostatic force equals the restoring force of the membrane and the membrane is brought in contact with the bottom electrode. This is known as "pull-in".

The effect of pull-in detection was simulated for our model by applying a

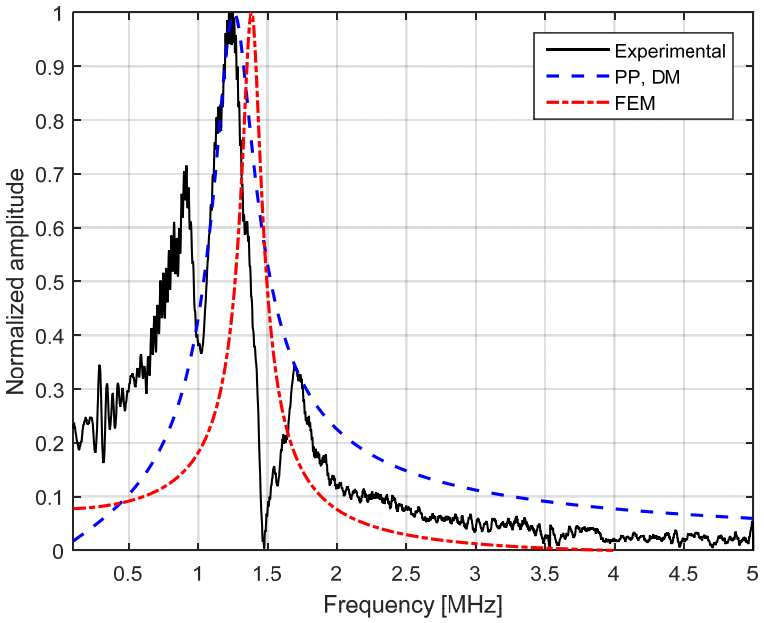


Figure 2.12: Comparison of the normalized frequency response of CMUTs with symmetric excitation in water.

gradually increasing voltage ramp. Figure 2.14 shows that the parallel-plate model and the deflected membrane model have a great accuracy even close to pull-in.

Both models PP and DM are able to capture the effects of pull-in and snap-back. The estimated and measured values of pull-in are specified in Table 2.3. It is important to mention that the prediction for the pull-in voltage using Mason's model is not possible given that the electrical transformer used maintains a linear behavior of the system regardless of the applied electrical signal. FEM simulations show that a pull-in voltage of 72.1V is expected. Some of the discrepancies are due to the fact that the real membrane is not fully metalized, moreover FEM models capture much

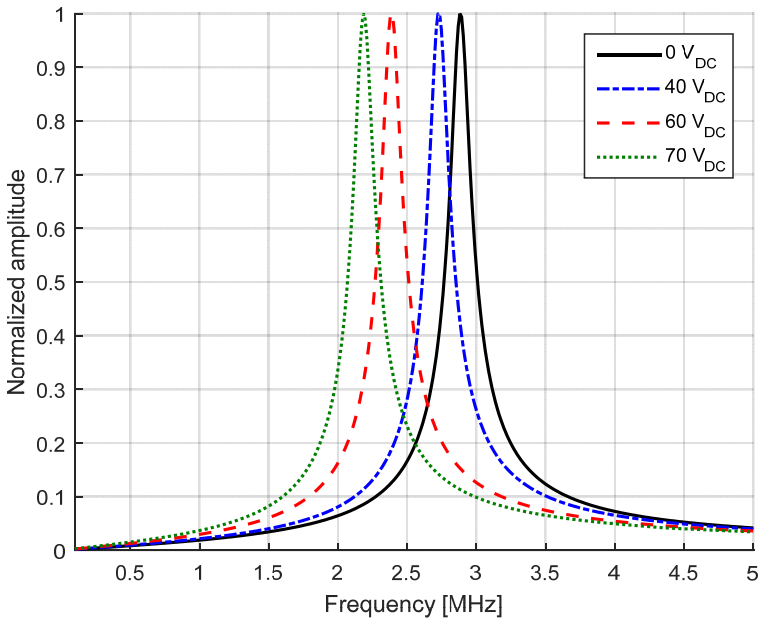


Figure 2.13: The proposed macromodel can capture the spring softening effect without adding extra electrical components to the circuit as in Mason's model

richer nonlinearities associated with CMUTs such as fringing fields effects.

An impedance analyzer Agilent E4294A (Santa Rosa, CA, USA) was used to detect the pull-in voltage experimentally. A linear sweep of DC voltage was applied between the terminals of the CMUTs. A change in the slope of the capacitance reading reveals that the pull-in voltage of this device is around 60V as shown in Figure 2.15. After pull-in, the central portion of the membrane is in contact with the bottom electrode, but the capacitance of the membrane keeps increasing since the areas on the membrane closer to the edges are being gradually attracted towards the bottom electrode.

The pull-in voltage measured experimentally is lower than the estimated

Table 2.3: Simulated and measured pull-in voltages

| **Model** | **Pull-in voltage [V]** |
|---|---|
| Deflected membrane model (DM) | 77.6 V |
| Parallel-plate model (PP) | 76.8 V |
| Mason (MS) | N.A. |
| Finite element modeling (FEM) | 72.1 V |
| Experimental results | ∼60 V |

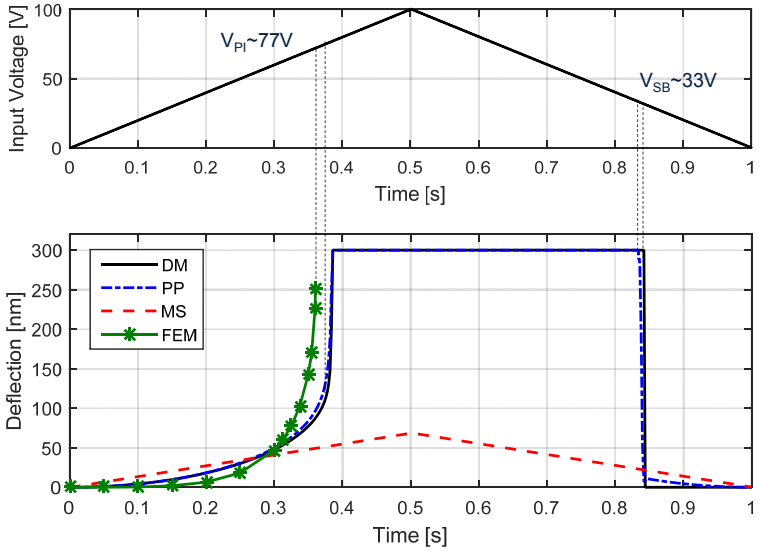


Figure 2.14: Comparison of membrane deflection when the bias voltage is gradually increased beyond the pull-in voltage. The linear behavior of Mason models is evident. The proposed model is able to capture the pull-in and snap-back operations.

by the simulations, this is attributed to the pre-biasing condition explained in section 4.5.3, where electrical charges trapped inside the membrane act as an intrinsic (built-in) bias voltage that decreases the pull-in voltage of the polyCMUTs and is currently not being captured by any existing model.

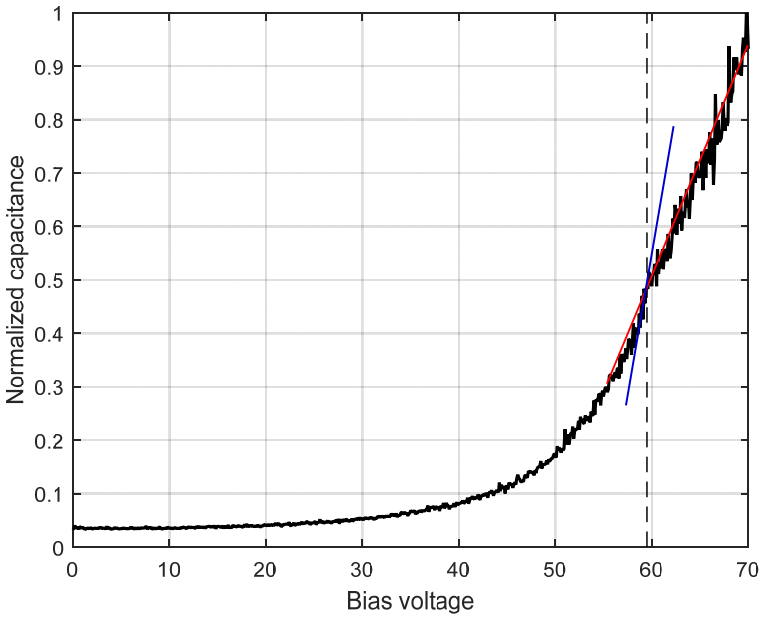


Figure 2.15: Capacitance measurement using an impedance analyzer when the DC bias voltage is gradually increased. A change in the slope in the capacitance reading reveals a pull-in voltage around 60V.

## 2.4 Discussions and conclusions

This chapter describes the development of a new type of model based on energy-flow theory. The non-linearities associated with the operation of CMUTs are captured in its constitutive equations and the model remains valid under any kind of excitation, even beyond the pull-in voltage, where the membrane is in contact with the bottom electrode. Two versions for this model were implemented. The first one treats the CMUT as a deflected membrane (DM) based on mode superposition theory; this captures the capacitance in a more accurately way as the center of the membrane deflects more than the areas closer to the edges; these equations can capture much

richer dynamics within the CMUT cells and will be used extensively in chapter 3. The second version treats the CMUT as a parallel-plate capacitor (PP), requiring much simpler equations for its implementation. From the simulation results we can deduce that the parallel-plate model can capture the behavior of CMUTs when compared to experimental results and FEM simulations of symmetric CMUTs. At low voltages, the results resemble the signals obtained using a typical Mason-like model; nevertheless, they diverge at large voltages given the linear behavior of Mason's model. It is important to mention that the simulation times for the proposed macromodel were in most cases around 3.5% of the time it took to simulate it in FEM software.

The experimental results in this chapter were obtained using polymer-based CMUTs (polyCMUTs), fully described in chapter 4. Even though there are some physical differences between polyCMUTS and traditional CMUTs fabricated using silicon nitride or polysilicon, the developed large-signal model is applicable for both cases; as its equations are based on vibration and energy-flow theory.

Chapter 3 is a side exploration of modeling of traditional CMUTs; focusing on the novel asymmetric operation. The motivation for this side track is to explore the resonant mode of vibration that originates from asymmetric operation.

# Chapter 3

# Equivalent circuit macromodel for asymmetric CMUTs

As mentioned in section 1.3.1 and depicted in Figure 3.1, symmetric CMUTs have one bottom electrode and one top electrode; whereas asymmetric CMUTs have one shared bottom electrode and two top electrodes electrically isolated from one another. Asymmetric CMUTs allow us to purposely excite non-axisymmetric modes of vibration in CMUTs that can be potentially applied to super-resolution algorithms [20] or physical beam steering and focusing [89].

When an asymmetric CMUT is immersed in fluid, the first vibration mode (symmetric) becomes overdamped, producing a wide bandwidth characteristic of traditional CMUTs; however, the second vibration mode (asymmetric) remains underdamped and it is still resonant, where each half of the membrane oscillates in opposite phase with one another. When a voltage is applied only on one bottom electrode in an asymmetric CMUT an effective tilted membrane is produced, as shown in Figure 3.2.

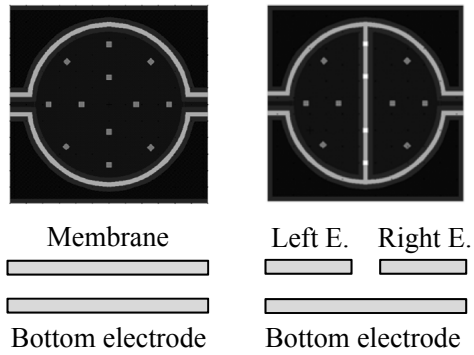


Figure 3.1: Top and cross-section view of a symmetric CMUT cell (left), and an asymmetric CMUT cell (right).

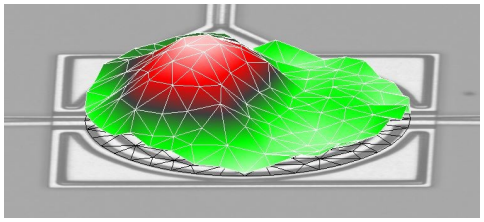

Figure 3.2: Measurement of the deflection of an asymmetric CMUT cell during asymmetric excitation. The result is a "tilted" membrane.

Resonant sensors are considered very sensitive devices because any change in the resonant frequency can be easily detected [90]. The resonant nature of the asymmetric mode in a fluid might have new applications such as sensing the variation in viscosity of fluids close to the membrane. This chapter explores the modeling of asymmetric CMUTs to understand the energy interactions between the domains involved.

When a nonuniform force is applied on the CMUT membrane, the overall deflection is the superposition of symmetric and asymmetric mode shapes. Asymmetric mode components are produced when an asymmetric force is

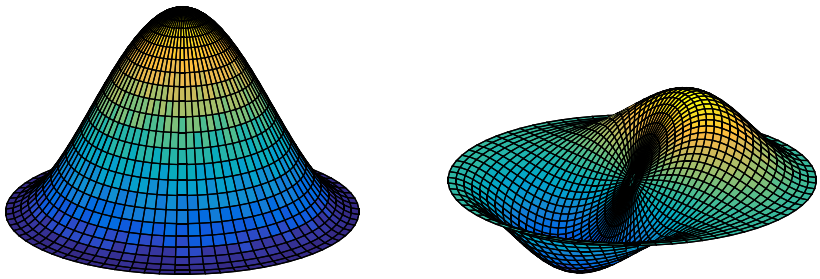

(a) (b)

Figure 3.3: First two natural vibration modes of a CMUT cell. **(a)** Mode (0,1) **(b)** Mode (1,1).

applied on the membrane, e.g., different electrostatic forces applied on the left and right sides of the membrane, or a difference in acoustic pressure during reception. The subscripts *(0,1)* and *(1,1)* in the form ($m$,$n$) refer to the number of nodal diameters ($m$) and the number of nodal circles ($n$) of the modes [14].

## 3.1 Equivalent circuit macromodel

As mentioned in section 1.3.2, equivalent circuit models are useful to capture the electro-mechano-acoustic interactions of CMUTs very accurately without the computational implications of FEM models. There are only a few works dealing with higher vibration modes for CMUT membranes [89], [37], however, they mostly deal with the first vibration mode of the CMUTs. The interactions between vibration modes in CMUTs have been modeled in [102], developing an equivalent circuit model based on Mason's theory and therefore valid around a fixed operational point. A detailed insight of the interactions between energies in asymmetric CMUTs during reception can

help us to optimize future designs and validate current theories regarding asymmetric CMUTs.

For symmetric CMUTs, each individual CMUT cell is typically modeled considering only the first vibration mode [15] as shown in Figure 3.3a; capturing the membrane deflection as a whole without distinguishing the details of the local dynamics of the membrane when asymmetric forces act upon it. Chapter 2 describes the development of a macromodel for symmetric CMUTs, taking velocities and forces as through and across variables; where each section of the circuit has two ports. This is sufficient to capture the behavior of CMUTs only when the first vibration mode *(0,1)* is in our interest.

An early version of an equivalent circuit model for asymmetric CMUTs appears in [89]. However, it had two mechanical output ports (one for each vibration mode) and only one electrical input port, limiting the application of arbitrary voltages on individual electrodes.

In this section, the development of a new macromodel with two electrical input ports and two mechanical output ports is described; in this way it is possible to apply independent voltages on each of the electrodes to predict the overall behavior of asymmetric CMUTs

### 3.1.1 Parallel-plate approach

Aiming to keep the simplicity of the parallel-plate model for symmetric CMUTs described in section 3.1.1, the asymmetric CMUT was initially considered as a parallel-plate capacitor as shown in Figure 3.4. Two assumptions for the development of this model are made:

1. The velocities on the left and right side for the first (symmetric) vibration mode *(0,1)* have the same magnitude and phase. i.e. $v_{L,01} = v_{R,01}$

2. The velocities on the left and right side for the second (asymmetric) vibration mode *(1,1)* have the same magnitude, but opposite phases. i.e. $v_{L,11} = -v_{R,11}$

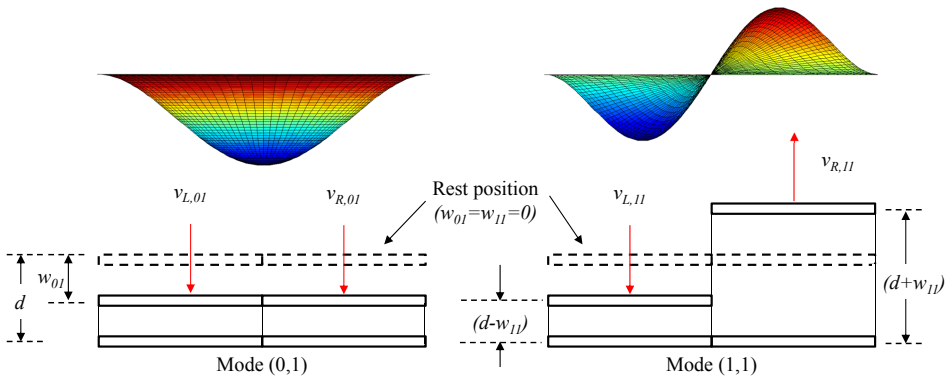


Figure 3.4: Deflections of an asymmetric CMUT membrane considering a parallel plate capacitor model.

Taking advantage of the orthogonality of the vibration modes [14] and following a similar approach as in section 2.2, an equivalent circuit model of an asymmetric CMUT was obtained and is shown in Figure 3.5.

The capacitors on the electrical side (left portion of the circuit) correspond to the electrical capacitance for each of the electrodes, and their value is given by:

$$C_{L,01} = \frac{A\varepsilon}{2(d - w_{01})}; \qquad C_{R,01} = \frac{A\varepsilon}{2(d - w_{01})} \tag{3.1}$$

$$C_{L,11} = \frac{A\varepsilon}{2(d - w_{11})}; \qquad C_{R,11} = \frac{A\varepsilon}{2(d - w_{11})} \tag{3.2}$$

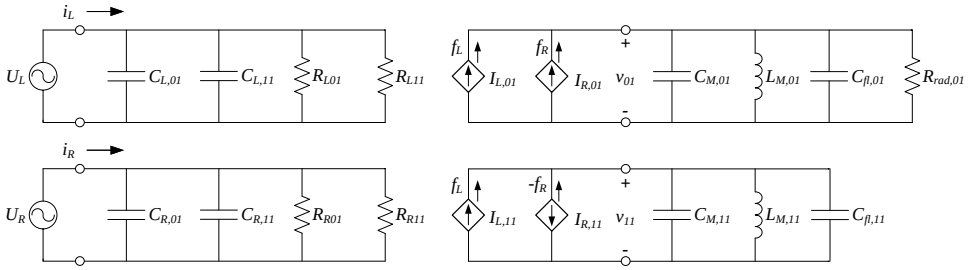


Figure 3.5: (0,1) mode and (1,1) mode equivalent circuit of an asymmetric CMUT.

where $A$ is the area of the CMUT membrane, $\varepsilon$ the permittivity and $w_{01}$ and $w_{11}$ are the membrane deflections during the *(0,1)* and *(1,1)* vibration modes respectively.

The resistors on this portion of the circuit represent the energy that is being dissipated on the electrical domain and is being transferred to the mechanical domain. Their values are given by:

$$R_{L,01} = \frac{1}{\frac{d}{dq}C_L(q)v_{q,01}}; \quad R_{R,01} = \frac{1}{\frac{d}{dq}C_R(q)v_{q,01}} \tag{3.3}$$

$$R_{L,11} = \frac{1}{\frac{d}{dq}C_L(q)v_{q,11}}; \quad R_{R,11} = \frac{1}{\frac{d}{dq}C_R(q)v_{q,11}}. \tag{3.4}$$

The dependent current sources on the mechanical side (right portion of the circuit) model the electrostatic forces acting on each of the electrodes of the CMUT membrane; represented by:

$$I_{L,01} = -\frac{1}{2}U_L^2\frac{d}{dq}C_{L,01}(q); I_{R,01} = -\frac{1}{2}U_R^2\frac{d}{dq}C_{R,01}(q) \tag{3.5}$$

$$I_{L,11} = -\frac{1}{2}U_L^2\frac{d}{dq}C_{L,11}(q); I_{R,11} = +\frac{1}{2}U_R^2\frac{d}{dq}C_{R,11}(q). \tag{3.6}$$

The parallel equivalent capacitances on the mechanical side are related to the equivalent mass of the modes:

$$C_{M,01} = C_{M,11} = \rho_p h A, \tag{3.7}$$

where $\rho_p$ and $h$ are the density and the thickness of the membrane respectively. The parallel equivalent inductors at the mechanical port represent the spring constants of the modes ($k_{01}$, $k_{11}$), and are related to the in-vacuum resonant frequencies $\omega_{01}$ and $\omega_{11}$ taken from [97]:

$$L_{M,01} = \frac{1}{k_{01}} = \frac{1}{\omega_{01}^2 C_{M,01}} \tag{3.8}$$

$$L_{M,11} = \frac{1}{k_{11}} = \frac{1}{\omega_{11}^2 C_{M,11}} \tag{3.9}$$

The fluid loading from the medium is treated differently here. In chapter 2, the acoustic impedance was treated considering the CMUT as a single cell operating in an infinite medium. When an array of CMUT membranes vibrate in phase, symmetry considerations lead to a single membrane vibrating in a waveguide with rigid walls, radiating a plane wave [28]. For this case, the mass loading from the medium can be computed from [14]:

$$C_{fl,01} = \frac{A\rho_m}{K_{01}} \tag{3.10}$$

$$C_{fl,11} = \frac{A\rho_m}{K_{11}} \tag{3.11}$$

where $\rho_m$ is the density of the medium and $K_{mn}$ is the structural wave number of the mode calculated as:

$$K_{mn} = \sqrt[4]{\omega_{mn}^2 \rho_p h / D} \tag{3.12}$$

where $D$ is the flexural rigidity of the membrane.

The radiation damping represented by a resistor on the mechanical side is significant for the (0,1) mode, and minimal for the (1,1) mode because the anti-symmetric pressure field does not propagate to the far field if the dimension of the membrane is much smaller than the acoustic wavelength [19]. The velocity potential for the non-axisymmetric modes is zero along the axis of the radiating CMUT; this is caused by the regions of the membrane vibrating out of phase for the non-axisymmetric modes [99]; therefore

$$R_{rad,01} = 1/\rho_m c A \tag{3.13}$$

where $c$ is the speed of sound in the medium.

This new macromodel has the same validity as the macromodel developed in section 2.2.1. When an equal voltage is applied on both electrodes, the CMUT exhibits a symmetric behavior, with the second vibration mode non existent in the frequency response. When the model is excited with an asymmetric signal, i.e., having the membrane and one top electrode grounded and applying a voltage on the other bottom top, an asymmetric vibration mode is produced.

### 3.1.2 Mode participation factors approach

The simplicity of the parallel-plate model approach makes it easy to implement in standard SPICE simulators; nevertheless it is not sufficient to capture the dynamics involved in asymmetric CMUTs. Asymmetric forces produce a different variation in the capacitance on both parts of the membrane; and it is not currently captured by the parallel-plate approach (PP) (see figure 3.6a). For this reason, mode participation factors theory [14] was used for the macromodel simulations.

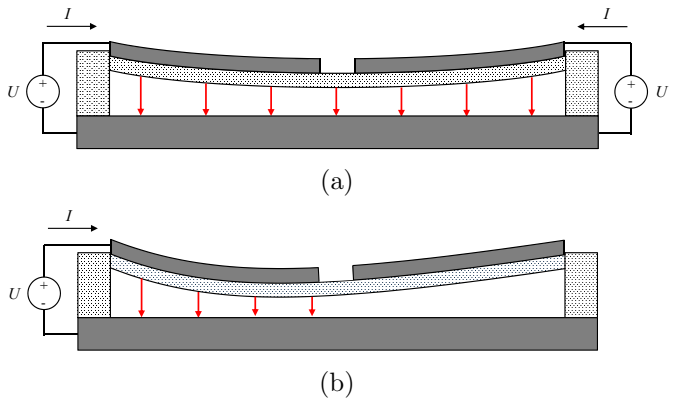


Figure 3.6: Deflection of the asymmetric CMUT membrane when (a) voltage is applied on both bottom electrodes, (b) "tilted membrane" effect when voltage is applied on one bottom electrode only.

This approach is especially useful to describe the electro-mechano-acoustic interaction when an overall asymmetric force deflects the membrane. Figure 3.6 shows the comparison of the membrane deflection in an asymmetric CMUT when the excitation voltage is applied on both top electrodes and on one single top electrode. The first case leads to the same vibration modes as a conventional symmetric CMUT, where the capacitance levels on

both electrodes have exactly the same value; however for the second case, a "tilted" membrane effect can be obtained (see also Figure 3.2), producing a variation in the capacitance levels for each electrode. In this case the capacitance value on the left is greater than the one on the right.

## 3.2 Simulations and experimental results

As covered in section 2.1.1, Mason-like models lack accuracy capturing all the non-linearities involved in the simulation of CMUTs. For this reason, only the results considering the deflected membrane (DM) model are presented. The implementation of the equivalent macromodel circuit shown in Figure 3.5 was done in Matlab-simulink and is shown in Figure 3.7. For comparison purposes, FEM simulations were implemented in Comsol Multiphysics (Comsol Inc., Burlington, MA, USA). The implemented model is show in Figure 3.8, where a 500$\mu$m water column with rigid walls boundary conditions sits on top of the clamped membrane. The other end of this column is set to irradiate plane waves. For all the simulations we considered the parameters indicated in Table 3.1.

Table 3.1: Simulation parameters for asymmetric CMUTs

| **Parameter** | **Value** |
|---|---|
| Membrane radius ($a$) | 60$\mu$m |
| Membrane thickness ($h$) | 7.82 $\mu$m |
| Air gap ($d$) | 0.52$\mu$m |
| Membrane material | SU-8-Chromium-Parylene-C |
| Equivalent flexural rigidity ($D$) | 2.308e-7 Pa·m$^3$ |
| DC bias voltage | 50V |
| AC driving voltage amplitude | 15V |

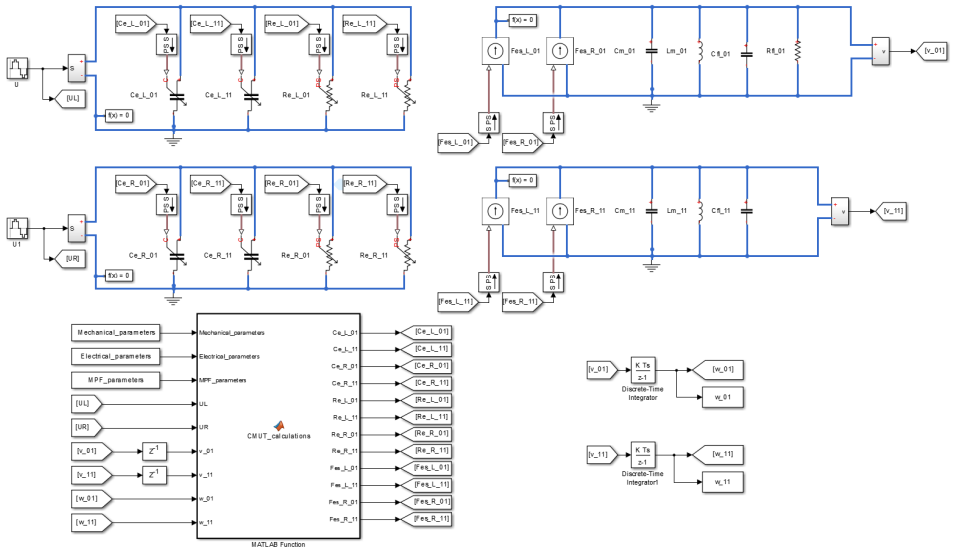


Figure 3.7: Implementation of the macromodel for asymmetric CMUTs in Matlab-Simulink, a script containing the implementation with Bessel functions is located in the subsystem at the lower-left corner.

The fabrication details of the asymmetric CMUT cells are specified in section 4.4. The CMUT cells were fabricated using the photosensitive polymer SU-8, where the membrane contains a metal electrode embedded between two layers of SU-8 for low actuation voltages.

### 3.2.1 Air operation

When a uniform voltage is applied on both of the top electrodes in an asymmetric CMUT cell, the frequency response of the device resembles that of a symmetric CMUT cell. Figure 3.9 shows the comparison between the frequency responses of an asymmetric CMUT cell operating in air when the same voltage is applied on both electrodes.

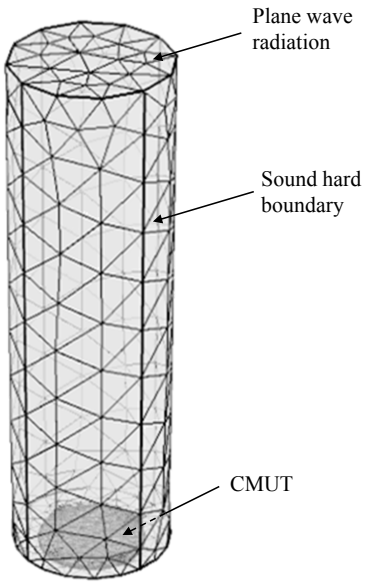


Figure 3.8: Model in Comsol of a single CMUT immersed in water. The membrane sits at the bottom of a water column to model array operation of CMUTs. The cylinder walls are set to sound hard boundary conditions. The other end of the cylinder is set to radiate planer waves.

All the vibration modes are present at any given time, but some of them contribute more than others to the overall deflection. In an asymmetric CMUT cell, when an excitation voltage is applied on one single electrode while the other is grounded, the second vibration mode *(1,1)* becomes more evident. Figure 3.10 shows how the second resonant mode is comparable in amplitude to the first mode *(0,1)*. The second resonant mode is also slightly downshifted in frequency.

There is a difference of 0.03MHz between the resonant frequencies predicted by our model and the ones from FEM simulations; compared to 0.19MHz between the ones from our macromodel and the ones measured

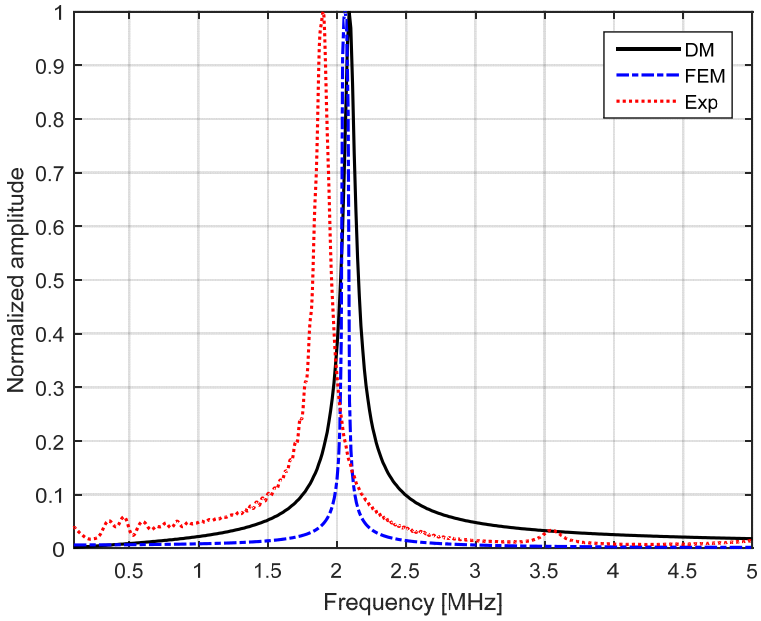


Figure 3.9: Comparison of the normalized frequency response of CMUTs with symmetric excitation in air.

experimentally for mode *(0,1)*. The discrepancy between simulation results and experimentation is attributed that there is a separation between the two electrodes in the physical membrane, affecting the overall mechanical stiffness in the membrane. For mode *(1,1)*, there is a difference of 0.23MHz between the frequencies from our macromodel and the ones from FEM, and a difference of 0.81MHz between the resonant frequencies from our macromodel and the ones from experimental results. Once again, the large discrepancy in the experimental results is attributed to the distribution of the added mass caused by the metal electrode on the membrane. This discrepancy could have been avoided by ensuring that the metal electrodes on the membranes located at the edges have the same effective mass than the

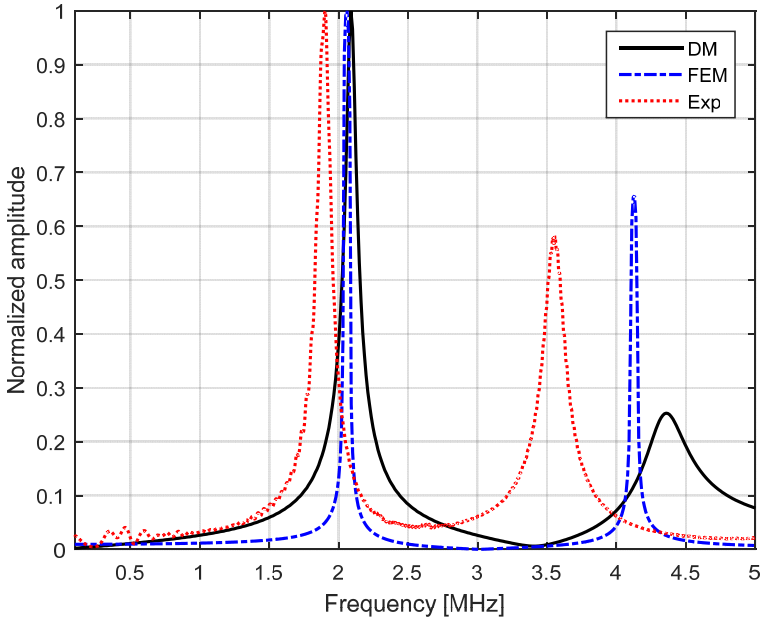


Figure 3.10: Comparison of the normalized frequency response of CMUTs with asymmetric excitation in air.

ones in the center.

### 3.2.2 Immersed operation

When the CMUT operates in a liquid medium, the fluid loads the membrane affecting its behavior. The first mode *(0,1)* appears overdamped, while the second mode *(1,1)* still shows a resonant behavior as shown in Figure 3.11. The location of the resonant peaks for this second mode in all the three cases present a larger separation. This is attributed to a more complex case of crosstalk between CMUT cells when they are immersed in fluid; moreover, in the real device, the top electrodes have a separation, and each half of the membrane is loaded with the effective mass of each top electrode.

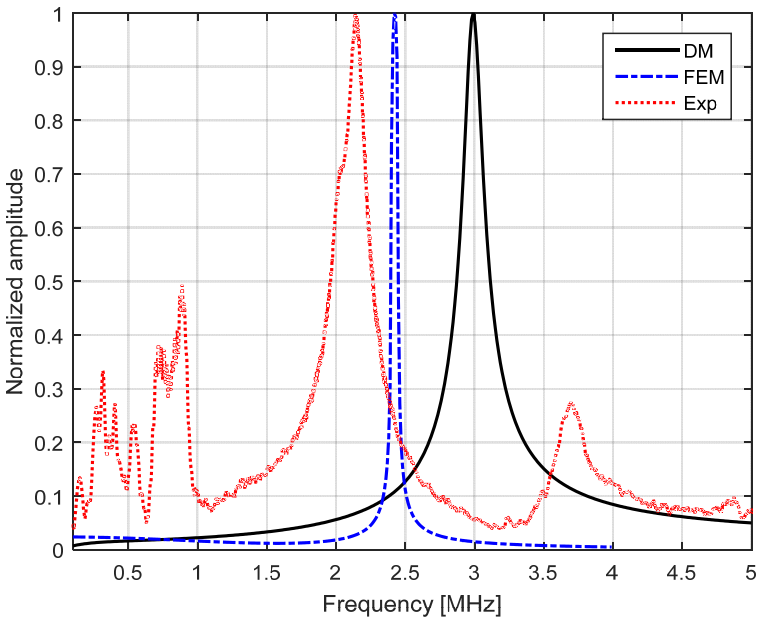


Figure 3.11: Comparison of the normalized frequency response of CMUTs with symmetric+asymmetric excitation in water.

Using the present macromodel, it is even possible to excite the membrane purely asymmetrically by adding a 180° phase delay in the applied sine signals for each electrodes coupled with a DC bias voltage as shown in Figure 3.12.

Another simulation was carried out to compare the variation in the capacitance on each electrode for the circuit developed in part 3.1.2 following the mode participation factors approach. The circuit was excited with a sinusoidal signal at 1MHz. Figure 3.14a shows capacitance levels on both sides of the CMUT when the voltage is applied to both electrodes, leading to an symmetric overall deflection. When the excitation voltage is applied on one single electrode the overall deflection resembles a “tilted” membrane,

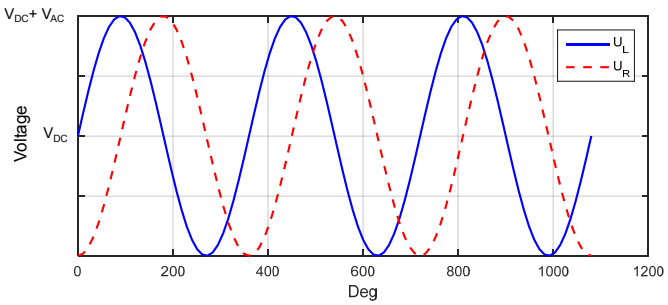


Figure 3.12: Excitation voltages in an asymmetric CMUT to produce a pure asymmetric excitation mode (only mode (1,1) present).

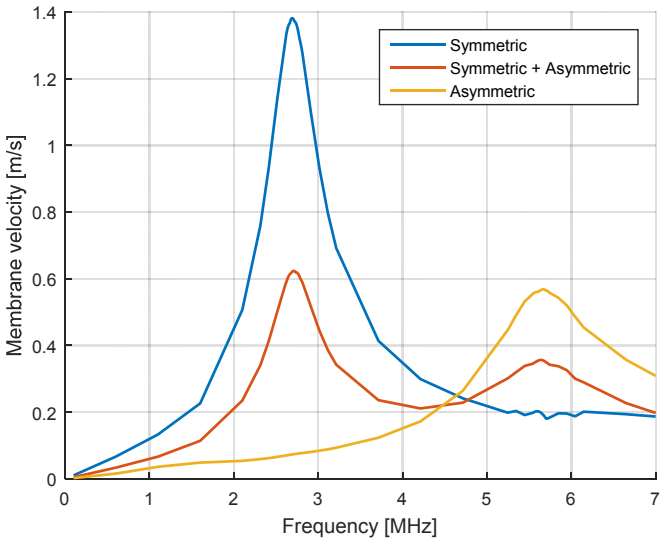


Figure 3.13: Comparison of different types of operation modes in an asymmetric CMUT.

producing a variation in the capacitance levels on each side as shown in Figure 3.14b.

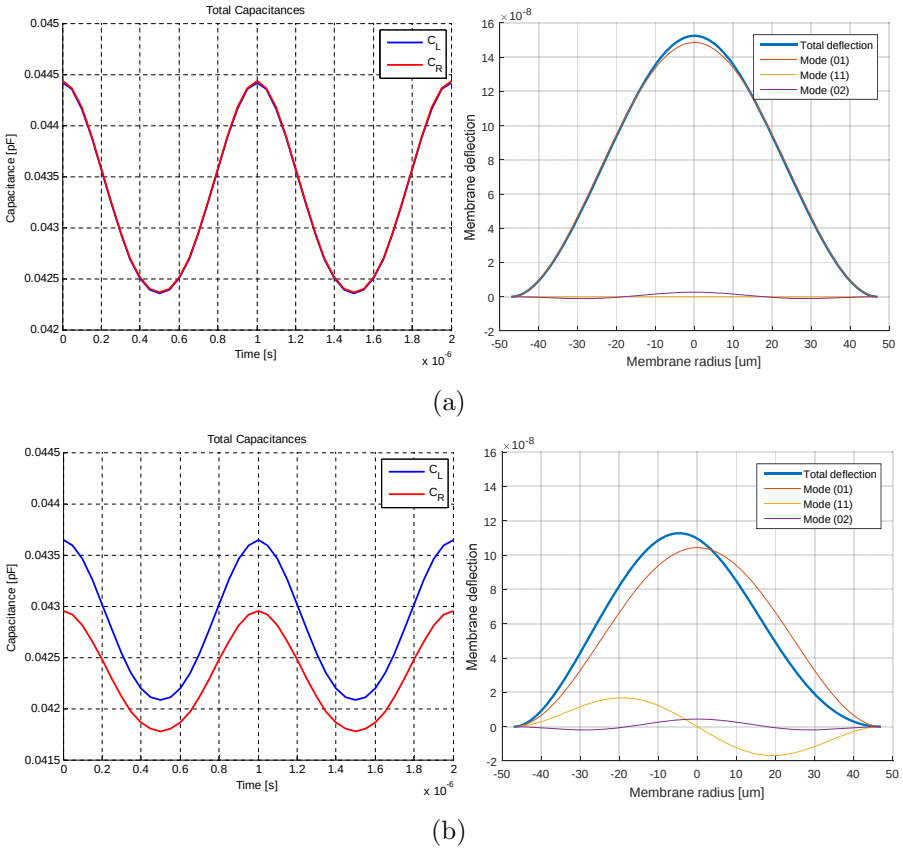


Figure 3.14: Capacitance levels on left and right electrodes of an asymmetric CMUT cell during (a) symmetric excitation and (b) asymmetric excitation.

### Spring softening effect

The asymmetric CMUT macromodel was tested to account for the spring effect. Figure 3.15a shows the spring softening effect for symmeyric excitation. Figure 3.15b shows the same spring softening effect when the membrane is excited asymmetrically. It is important to notice that a higher pull-in voltage is achieved when only one of the top electrodes is energized.

Being able to capture the electro-mechano-acoustic interaction in an

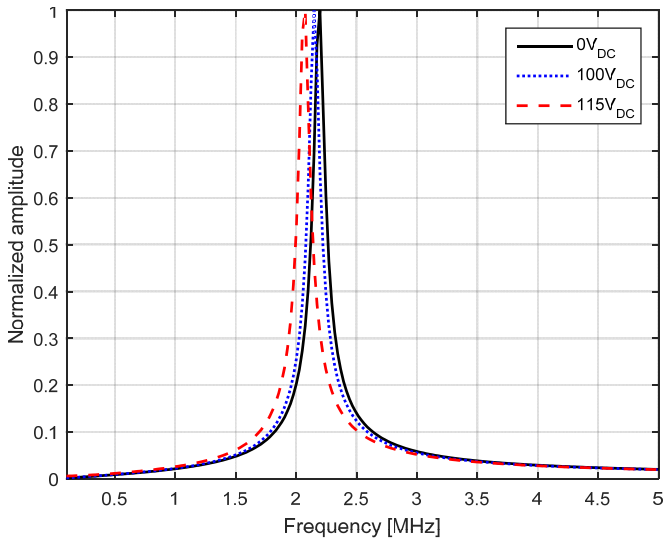


(a)

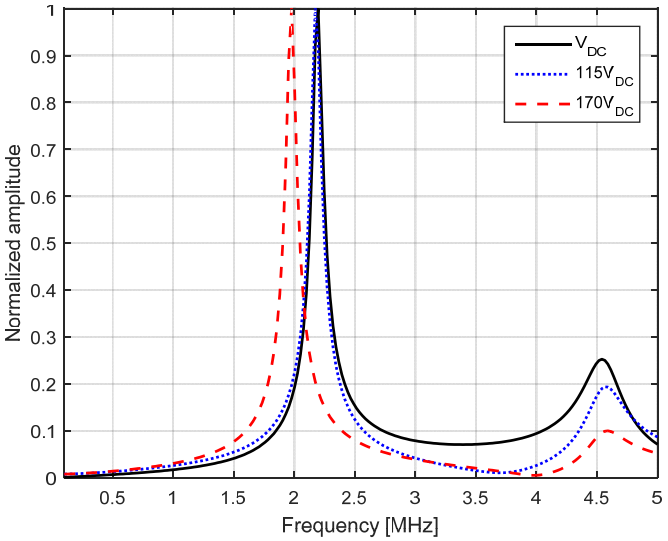


(b)

Figure 3.15: Spring softening effect of a CMUT cell (a) symmetric excitation and (b) asymmetric excitation.

asymmetric cell is not the only advantage of this circuit. Another advantage of this macromodel is that it captures the behavior of a symmetric and an

asymmetric CMUT cell under any kind of voltage without linearizing the circuit around an operating point as Mason's like models [26] does.

## 3.3 Pull-in detection

The effect of pull-in detection was simulated for our model by applying a gradually increasing voltage ramp. Figure 3.16 and 3.17 shows the simulation results compared to FEM data for both cases, symmetric and asymmetric excitation. FEM captures fringing field effects not captured by our model and captures a lower pull-in voltage. Once again, the pull-in voltage for asymmetric excitation is much higher.

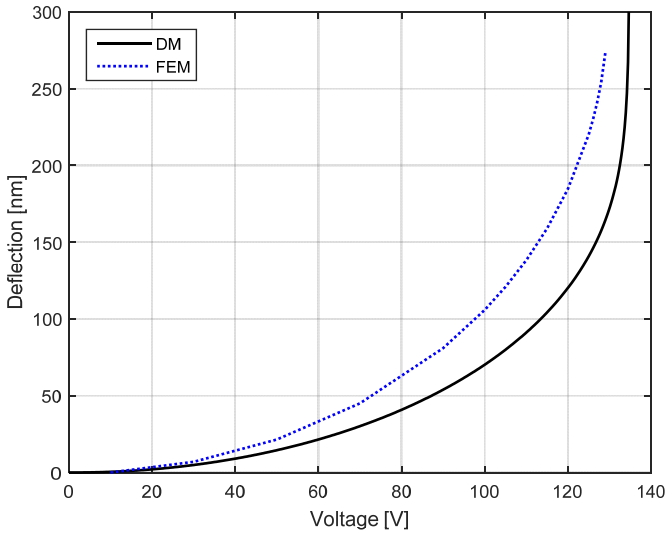


Figure 3.16: Pull-in detection in asymmetric CMUTs with symmetric excitation (same voltage applied on both top electrodes).

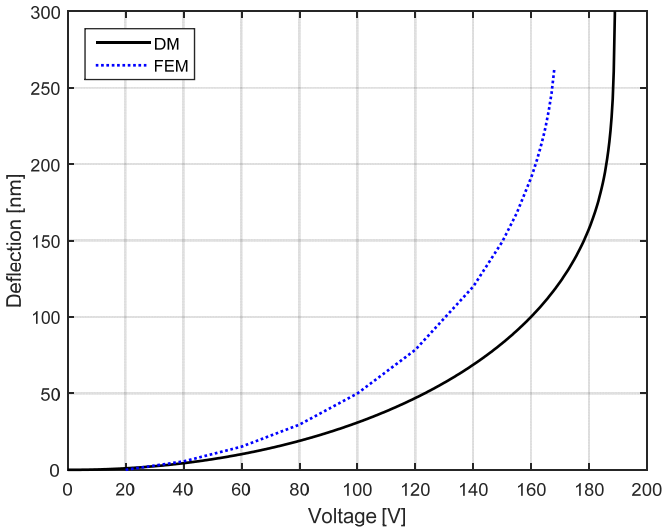


Figure 3.17: Pull-in detection in asymmetric CMUTs with asymmetric excitation (voltage applied on one top electrodes, the second top electrode is grounded).

## 3.4 Impedance analyzer measurements

The behavior of immersed CMUTs were tested using an impedance analyzer Agilent E4294A (Mountainview, CA, USA). The CMUT array was immersed in a container filled with mineral oil and biased with $40V_{DC}$. A frequency sweep was done to identify the changes in impedance produced by the vibration of CMUTs. The same ripple artifacts observed during experimental characterization in section 2.3.1 appeared in the measurements. It was noticed that the amplitude and separation of these ripples were reduced as the oil levels were increased. Figure 3.18 shows the reduction of ripples with higher oil levels; a DC bias was added during post-processing for clarity.

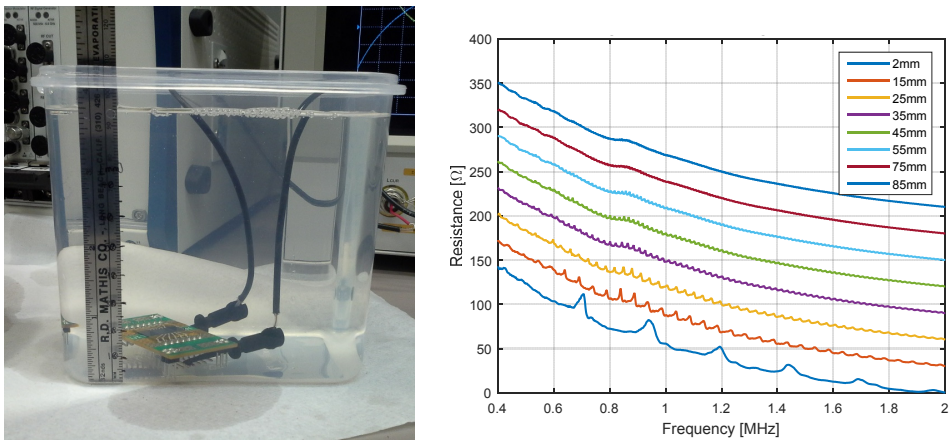


Figure 3.18: Impedance measurements of CMUTs immersed in mineral oil for different depths. The ripples in the measurements are thought to be originated by reverberations in the air-oil interface

It is inferred that the artifacts using a laser doppler vibrometer (LDV) would disappear with higher oil levels, nevertheless the LDV failed to obtain an accurate measurement when the oil levels were too high. Waves appearing on the surface of the liquid originated by mechanical noise background caused light diffraction problems.

## 3.5 Conclusions and Discussion

A large-signal model that accurately captures the dynamics associated with asymmetric CMUTs was developed. This equivalent circuit remains valid under different excitation voltages, as opposed to other equivalent models where the operational point is around a fixed DC bias voltage. We followed the mode participation factors approach to capture the different vibration modes of a CMUT membrane; when the CMUT is excited symmetrically

(same voltage applied on both top electrodes), the first vibration mode *(0,1)* dominates the overall deflection; when the device is excited asymmetrically (voltage applied on one single top electrode), the second vibration mode *(1,1)* becomes more evident and is comparable in magnitude with the first mode. The discrepancy regarding the real and expected resonant frequencies of the asymmetric CMUT was attributed to the physical differences in the real membrane. The fabrication process leads to a membrane with its borders not fully-clamped and with section of the membrane loaded with the effective mass of the top electrodes. Further research is being done around these devices in our facilities, exploring the advantages presented in section 1.3.1.

This completes the analysis of the operational modes for both symmetric and asymmetric CMUTs. Given the ample and direct application of symmetric CMUTs, we decided to analyze them experimentally while exploring new fabrication techniques using inexpensive materials. The next chapter returns to the main hypothesis that, with proper modeling, a polyCMUT can be designed, fabricated and validated.

# Chapter 4

# Polymer-based Capacitive Micromachined Ultrasound Transducers (polyCMUTs)

After completing the modeling and analysis of symmetric and asymmetric CMUTs using energy-flow theory in the previous two chapters, we simulated the behavior of CMUTs when different material properties and dimensions were used. We realized that softer materials could provide better performances than rigid ones; therefore, we explored the possibility of fabricating CMUTs using novel materials and techniques.

As mentioned in section 1.3.3, silicon nitride and polysilicon are the most popular materials for fabricating CMUT membranes, while chromium, aluminum and gold are typically used to pattern electrodes on top of these membranes. These materials are chosen mainly for their mechanical properties, such that the membranes can be as thin as possible, in order to minimize the effective gap between the bottom and top (or hot) electrodes. By decreasing the effective gap between electrodes, the electric field can be increased, and the impedance matching to the electronics can be improved

[47] . Once the desired operational frequency and the maximum biasing voltage have been identified, the CMUT membranes should be designed as thick as possible, given that their bandwidths linearly increase with thickness [103].

## 4.1 Motivation of using polymers as structural material

Photopolymers are inexpensive, can be patterned using ultraviolet (UV) light, and have been used for the fabrication of microelectromechanical systems (MEMS) devices [104, 105]. Their low density and high mechanical strength make them suitable for CMUTs because the impedance matching with the medium can be improved. Nonetheless, fabricating CMUTs using polymers is challenging because a thick membrane with a metal electrode on top is needed to reach the MHz region, contravening the required short gap between electrodes for low operational voltages and maximum sensitivity. Thus, despite some research in fabricating CMUTs using polymeric materials [81–83], the operational voltages were in the order of hundreds of volts, making them less attractive to be used in biomedical ultrasound industries [57]. Moreover, the mentioned devices were reported to be only operating in air.

Despite the advantages of polymers for fabricating CMUTs, the main limitation for their applications is the large effective gap between electrodes and the requirement to be properly sealed for operating in fluids. Our solution for this problem was to embed the electrode inside the membrane

to bring it closer to the bottom electrode, without sacrificing the overall thickness required to be in the MHz range.

Herein, we present in this chapter a new fabrication process for CMUTs using polymeric materials and demonstrate for the first time the use of an operational CMUT array in a liquid medium. This chapter is focused on the fabrication side of polymer-based CMUTs that can be produced in a basic microfabrication facility.

## 4.2 Structural materials

In addition to improvements in the effective bandwidth, sensitivity, and radiated output pressure, a proper selection of fabrication materials can lead to improvements in the fabrication process and, in turn, lower the cost. We specifically selected the photopolymer SU-8 2000 series [106] as a structural material for our applications, given its unique dielectric and thermal properties, as well as its low density, photopatternability, optical transparency, and mechanical flexibility.

## 4.3 Selection of sacrificial layer

A crucial component in the fabrication of the cavities required for CMUTs is the sacrificial layer, where a high selectivity of the etchant is required to properly dissolve the sacrificial layer without damaging the membranes.

Different materials have been used as sacrificial layers when working with SU-8. Song et al. [107] used overbaked positive photoresists to withstand the attack of solvents present in SU-8 to form electroplating molds,

and the sacrificial layer was later removed using plasma etching. Moser et al. [108] altered the chemical composition of SU-8 to make it more sensitive to UV light, and a standard SU-8 formulation was used as a sacrificial layer to create microchannels. Foulds et al. [109] patterned polydimethylglutarimide (PMGI) to be used as a sacrificial layer, using a combination of positive photoresists and repetitive sequences of near ultra violet (UV) and deep UV light exposures. Chiriaco et al. [110] created microchannels by patterning PMGI without using deep UV light; the masking material for PMGI was removed in acetone, leaving the sacrificial layer prone to damage since acetone also attacks the PMGI. Finally, different metals have also been used as sacrificial layers [111, 112], where they are either evaporated or sputtered, requiring long deposition times and leaving rough surfaces. Metals also require extra fabrication steps to be patterned for use as sacrificial layers.

### 4.3.1 Explored sacrificial materials

In the attempt of fabricating a polymer-based CMUT, several materials were explored as sacrificial layers. A potential candidate was a thermally modified photoresist S1813 used in [107]. This photoresist was overbaked at a higher temperature (150°C) than the specified in the S1813 datasheet (115°C) to withstand the attack of the chemicals present in SU-8 following [106]. After coating and patterning a layer of SU-8, the overbaked sacrificial layer could not be removed by organic solvents typically used for this purpose (acetone, PG remover). The sample had to be immersed in an ultrasound bath to partially remove this sacrificial layer, but the SU-8 structures

were damaged at the same time. Lower baking temperatures were tested with the same result. When low baking temperatures were used (120°C), the solvent present in SU-8 (cyclopentanone) started to attack the S1813, completely destroying the original patterns. Similar results were reported in [113].

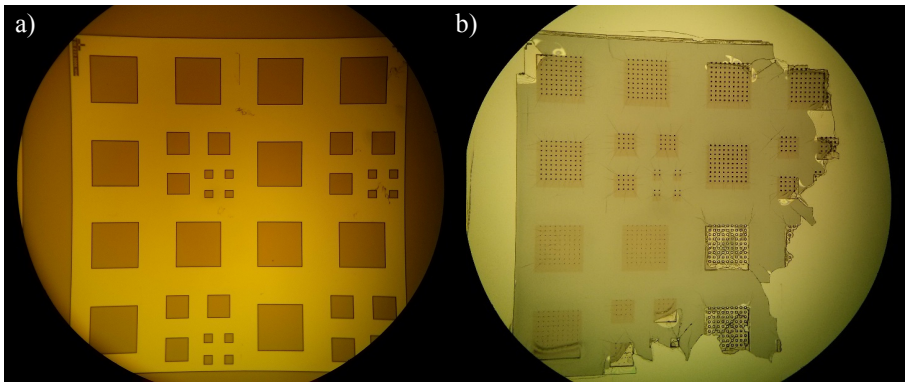


Figure 4.1: Overbaked S1813 as sacrificial layer. a) Patterned square areas using S1813 prior spin coating SU-8, these square areas will become the cavities of CMUTs, b) SU-8 structures patterned on top of the sacrificial layer, an ultrasound bath had to be used to partially remove the S1813 underneath, leading to damage of the membranes.

Water-soluble sacrificial layers have been reportedly used with SU-8 [114] to release large structures from rigid substrates. Two of these materials were tested in this project: poly-vynil acid (PVA) and poly-acrylic acid (PAA). These materials were acquired from Sigma-Aldrich (St. Louis, USA) and dissolved in di-ionized (DI) water at a concentration of 10%. The solutions were spin coated on silicon wafers and baked at 65°C to evaporate the solvent (water).

Since this material is not photosensitive, a masking material had to be

used to pattern the PVA and PAA using water. For the case of PAA, different masking materials were tested: the positive photoresists S1813 [106], AZP4110 [106], even a combination of SU-8 and PG-remover [106]. Nevertheless, a residual layer shown in Figure 4.2 was formed after removing the masking material. This was attributed to the difference in pH of the materials used as reported in [114]. A proper lithography step to fabricate membranes could not be used for this PAA.

When working with PVA, S1813 was used as masking material. It was possible to pattern sacrificial geometries. After depositing and patterning a layer of SU-8, the sample was immersed in DI water to remove the sacrificial layer. The etching was monitored over time, and after 24 hours, only a few cavities with short and wide etch channels could be etched, many of the samples remained with some PVA trapped inside and could not be removed without damaging the SU-8 structures on top. The results are shown in Figure 4.3.

### 4.3.2 Omnicoat

One of the main novelties of this work is the use of a well-known material in a novel way to create the CMUT cavities. Omnicoat [106] has been widely used as a lift-off material to release SU-8 structures from silicon wafers. It has an excellent selectivity during etching and enhances the adhesion of photoresists to different substrates. Despite these properties, Omnicoat is not photosensitive and the typical thickness during spin coating ranges from 5 to 15 nm. Since a sacrificial layer in the order of hundreds of nanometers is needed, we evaporated 85% of the solvents present in Omnicoat. Thus,

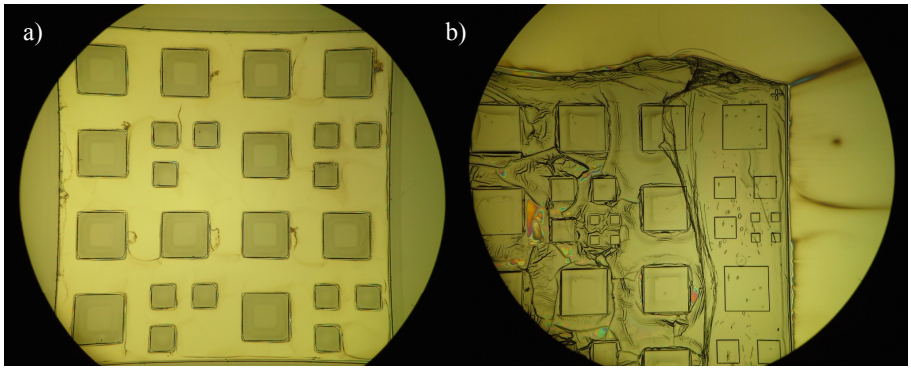


Figure 4.2: Poly-acrylic acid (PAA) as sacrificial layer. a) Patterned square areas prior spin coating SU-8, these square areas will become the cavities of CMUTs, b) SU-8 structures patterned on top of the sacrificial layer, an undesirable residual layer formed between the interface between SU-8 and PAA.

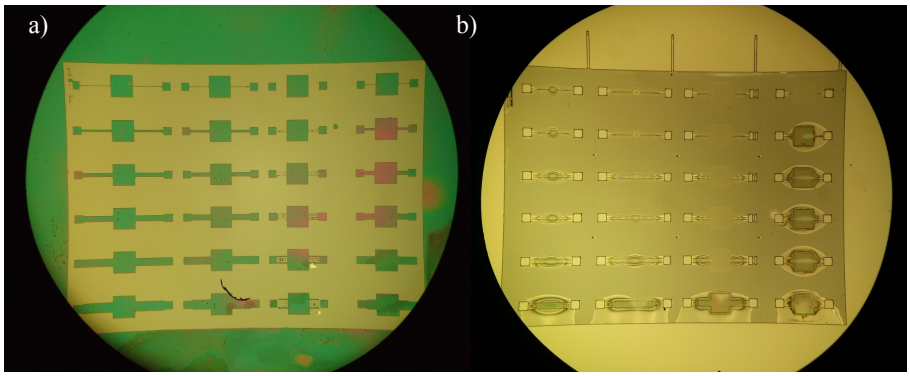


Figure 4.3: Poly-vinyl acid (PVA) as sacrificial layer. a) Patterned square areas with release channels prior spin coating SU-8, these square areas will become the cavities of CMUTs, b) SU-8 structures patterned on top of the sacrificial layer, the sacrificial material did not etch completely through the etch channels.

a much denser version of the same chemical was used for spin coating. Using this approach, we were able to increase the coating thickness from

15 nm to 300 nm in a single step at 1000 RPM. Multiple coatings could be stacked, or a higher percentage of the solvents could be evaporated if an even thicker sacrificial layer is desired. This might be useful in microfluidic applications where channels with different heights are typically used [115]. In our approach for CMUTs, the thickness of Omnicoat can be accurately controlled by spin coating; and it can be patterned at the same time as a masking material deposited on top. Omnicoat also has an excellent adhesion to different substrates, possesses excellent selectivity against solvents, and allows the substrates to be re-worked if necessary.

Figure 4.4 shows a test sample for Omnicoat during etching. It consists of an array of square cavities with different channel lengths and widths (Figure 4.4a). Figure 4.4b shows the array of square membranes covered by a thin layer of SU-8 with patterned openings for the releasing channels. Figure 4.4c shows the gradual etching of Omnicoat after immersion in the positive photoresist developer MF319. Figure 4.4d shows the complete removal of sacrificial material after 40 minutes. Even after complete etching of Omnicoat, the sample was left immersed in the developer for 48 hours. No damage was detected on the structures, and Omnicoat was finally selected as sacrificial material.

## 4.4 Fabrication of polyCMUTs

Figure 4.5 and Figure 4.6 depict the fabrication steps for the creation of polyCMUTs. A maskless lithographic system SF-100 (St. Petersburg, USA) was used for UV exposure given its rapid prototyping capabilities; however,

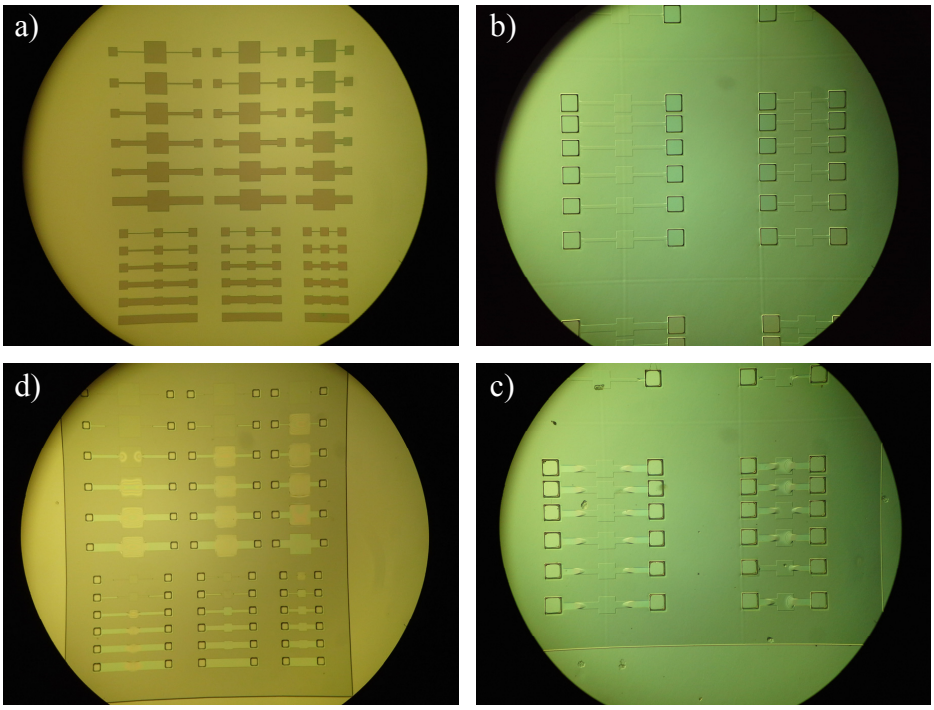


Figure 4.4: Experimentation with Omnicoat as sacrificial layer. a) Patterned Omnicoat structures, b) Layer of SU-8 deposited on Omnicoat structures with patterned holes to access the sacrificial layer, c) Omnicoat layer gradually being etched when the sample was immersed in developer MF319, d) Omnicoat sacrificial layer completely removed. SU-8 structures were not damaged even after 48 hours immersed in developer.

if needed, a standard mask aligner with photomasks can be used to replicate the results presented in this chapter.

The fabrication started with a clean and low electrical resistance silicon wafer that acts as the bottom electrode (<100> orientation, boron-doped, resistivity $< 100$ Ω·cm). We spin coated the concentrated version of Omnicoat (15% of its original volume) onto the wafer and baked it at 150°C for 3 min to obtain a 320nm sacrificial layer. A layer of positive photoresist

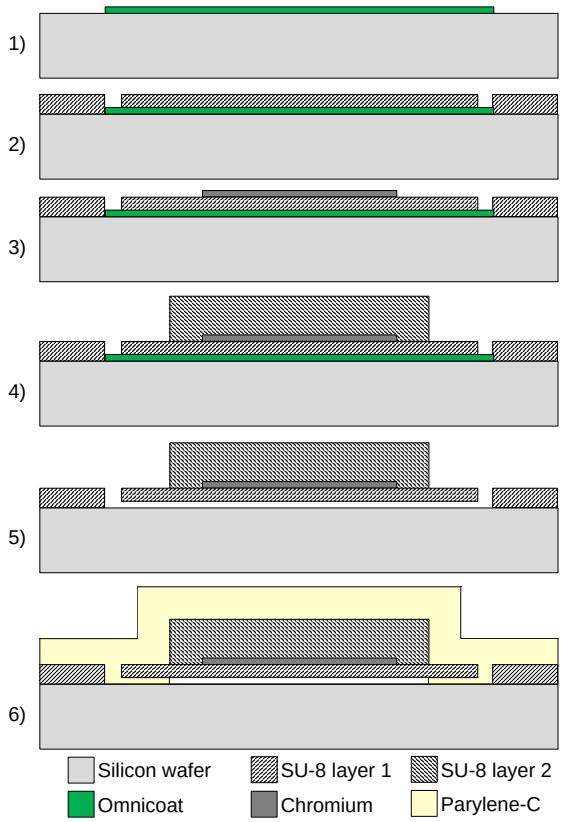


Figure 4.5: Cross-section view of the six fabrication steps used to create polymer-based CMUTs (polyCMUTs)

S1813 [106] was then deposited and patterned using UV light to create a masking layer to selectively remove the Omnicoat underneath. The sample was then immersed in alkaline-based MF319 developer [106] for 60 sec, simultaneously etching the exposed areas of both S1813 and the Omnicoat; the etching was stopped by rinsing the sample in DI water. The S1813 masking layer was then removed in acetone. Because of its excellent resistance to solvents, a patterned Omnicoat sacrificial layer was left intact

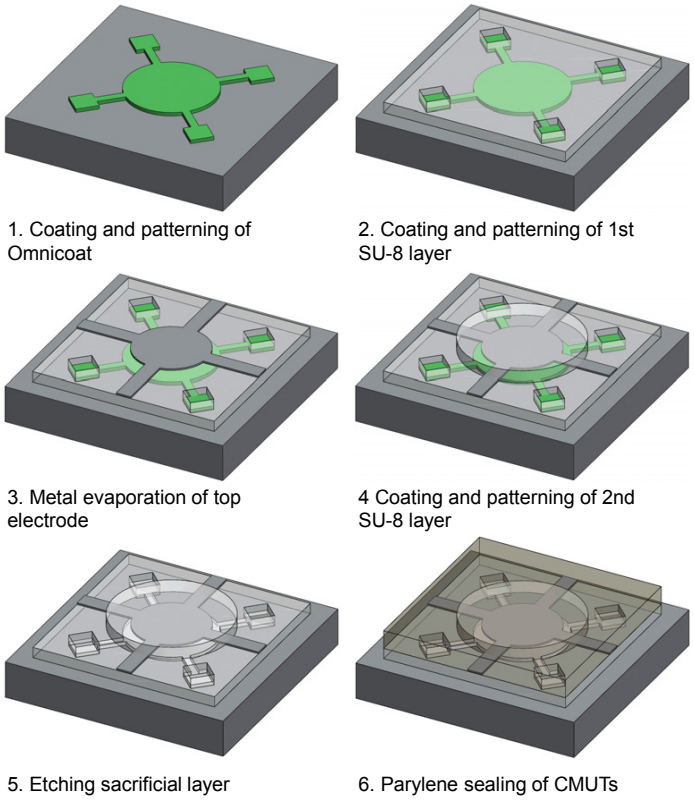


Figure 4.6: Overview of the six fabrication steps used to create polymer-based CMUTs (polyCMUTs)

without damage. A plasma etching step in $O_2$ for 1 minute is recommended at this time to completely eliminate all possible residues of Omnicoat left after etching and to increase adhesion of SU-8 to the silicon wafer. After plasma etching, the effective thickness of the sacrificial layer measured using a profilometer was 300nm.

A layer of SU-8 2000.5 was spun at 2000 RPM onto the sample to obtain a thickness of 0.67$\mu$m. The thickness facilitated conformal coating of the

Omnicoat areas that became the cavities and etch channels of our device. A short pre-baking step at 95°C was performed for 3min prior UV exposure. The membranes, etching via holes, and clamping areas of the CMUTs were patterned in UV light; and the sample was post-exposure baked and developed. The SU-8 layer acts as a mechanical support for the top electrode and as dielectric material to avoid any short circuit since the dielectric strength of SU-8 reaches as much as 50% of that of $SiO_2$ [116].

A layer of AZP 4110 photoresist was coated and patterned to act as a lift-off layer before evaporating on 570nm of chromium. Chromium was selected because of its excellent adhesion properties to SU-8 films and low electrical resistivity [117]. A metal evaporation was preferred over sputtering because of its directional deposition, which simplifies the lift-off process. Once the electrodes are properly patterned, a second layer of SU-8 2002 was spin coated at 1000 RPM to obtain a thickness of 2.40$\mu$m, thereby covering the previous stack of Omnicoat, SU-8 and chromium layers. After pre-baking, the sample was exposed to UV light to pattern the top part of the CMUT membranes, leaving open areas for the etching holes. The sample was cured at 150°C for 5 min and then gradually cooled down to room temperature. This annealing step removes any possible cracks created and increases the Youngs modulus of the SU-8 films [118].

The sample was then immersed in the developer MF319 [106]. This etchant penetrates through the etch channels and gradually removes the Omnicoat material underneath the cavities. The circular cavities have a radius of 50$\mu$m, and the etch channels are 5$\mu$m wide and 15$\mu$m long. After 3 hours, the Omnicoat sacrificial layer was completely removed. The sample

was then immersed in de-ionized water for 2 hours to displace the MF319 developer trapped inside the cavities. Finally, the sample was immersed in isopropanol to replace the water.

A Tousimis (Rockville, MD, USA) critical point dryer was used to completely release the membranes, avoiding any stiction problems [119]. In order to make our membranes watertight, a 3.67$\mu$m layer of Parylene-C was deposited in a low-pressure chamber, creating a sealed vacuum cavity inside the CMUT cell. In addition to providing excellent electrical insulation, Parylene-C is also biocompatible, optically transparent, has a low Youngs modulus, and has a coefficient of water absorption close to zero [120]. The dimensions of the fabricated CMUTs are specified in Table 4.1. The materials used, allows a visual inspection of the fabricated device, facilitating the identification of any possible defect.

Table 4.1: Parameters of fabricated polyCMUTs

| **Parameter** | **Value** |
|---|---|
| Membrane radius | 50$\mu$m |
| Sacrificial layer thickness | 0.30$\mu$m |
| Membrane SU-8 layer 1 thickness | 0.67$\mu$m |
| Top electrode thickness | 0.57$\mu$m |
| Membrane SU-8 layer 2 thickness | 2.40$\mu$m |
| Pasivation layer thickness | 3.67$\mu$m |

By using SU-8 and maskless lithography, a fully functional prototype was created in 17 hours. This compares favorable to multi-user wafer fabrication services, such as MEMSCAP [92], where multiple designs are combined and processed with fixed fabrication protocols and long turnaround times.

It is important to mention that the described fabrication process employs non-hazardous materials, i.e. only organic solvents are used during manufacturing (acetone, isopropanol, SU-8 developer, and positive photoresist developer). The health risks associated with an accidental prolonged exposure to these materials do not go beyond drowsiness or minor skin irritation. This contrasts with the hazardous gas silane required to deposit silicon nitride and silicon dioxide or the hydrofluoric acid (HF) to remove the sacrificial silicon dioxide layer in traditional CMUT fabrication [47, 121].

The final performance of the device is affected by several design parameters such as cavity height, membrane radius and thickness, electrode size, etc. Different designs with etch channels widths and lengths were tested in order to determine the optimum dimension for the polyCMUT array. The results are shown in Figure 4.7. The inherent resolution of the UV exposure system used allowed us to have release channels measuring 5$\mu$m in width and 15$\mu$m in length. Based on experimentation, a membrane radius of 50$\mu$m gave us an acceptable fill factor while maintaining a low risk of stiction during releasing.

The CMUT cavity was designed to account for the natural deflection of the membrane caused by the atmospheric pressure after vacuum sealing. The remaining gap should be large enough to allow the membrane to vibrate during normal operation given the maximum allowed voltage.

The thickness of the first layer of SU-8 depends on the maximum operating voltage of the CMUT, it should be as thin as possible to maintain a small effective gap between electrodes while providing a good electrical insulation to prevent any voltage breakdown in case the membrane is brought

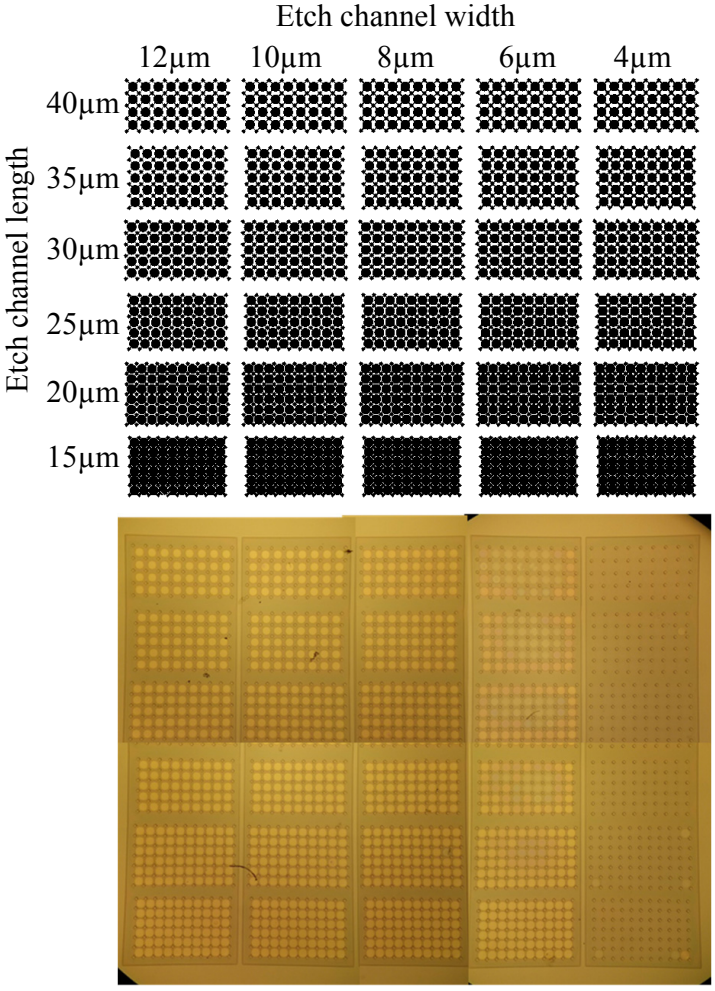


Figure 4.7: Experimental setup to assess the best geometry for sacrificial release channels. An array of circular membranes with releasing channels varying in length and width. Photolithography design (top). Fabricated structures (bottom). Optimum design was 5$\mu$m X 15$\mu$m release channels.

in contact with the bottom electrode. A thermal annealing of this layer removes any possible micro cracks and enhances the adherence of SU-8 to the substrate and to the subsequent chromium layer. A gradual cooling

procedure is recommended as it reduces the risks of delamination.

Chromium was chosen as the top electrode material based on the excellent adhesion strength to SU-8 [117] and to the fact that it requires one single masking layer during lift-off. The metalization radius was set to 46% of the membrane radius in order to increase the bandwidth of the final device [103]. This metal layer should be as thin as possible to minimize its effects on the mechanical properties of the membrane. A 500nm layer was sufficient to maintain a good electrical conductivity between electrodes. Having a layer too thin can result in resistive interconnection paths that, combined with the capacitance of the CMUT cells would behave as a natural low-pass RC filter that degrades the driving signals during excitation.

The thickness of the second SU-8 layer is tailored to the desired operational frequency of the device. Since the effective gap between the top and bottom electrodes (and therefore the operational voltage) is dictated by the cavity height and thickness of the first SU-8 layer, this design allows the fabrication of low-frequency and high-frequency CMUTs with constant operational voltages. This contrasts with the design in traditional CMUTs where the operational voltage increases with membrane thickness. A further discussion is treated in section 6.3.3.

During the design stage, the thickness of the sealing parylene-C layer should be taken into account as it has similar mechanical properties as SU-8. For example, a sealing parylene-c layer with a similar thickness as the second SU-8 layer increases the resonant frequency of the membrane by 85%. If a soft sealing material is to be used with more rigid materials such as polysilicon or silicon nitride then its effects on the final resonant

frequency will be minimal. On an extreme case, where the membrane is made out of even softer materials such as PDMS, then the parylene layer will have the greater influence in the resonant frequency of the device.

The adhesion of SU-8 to chromium is known to be exceptional, given that metals with smaller electronegativity tend to have better adhesion strength with SU-8 films [117]. There is however, a latent risk of delamination when two materials are bonded together. One of the first approaches of this project was to have open areas on the metallic electrodes to allow a better bonding between the two SU-8 layers forming the membrane. Figure 4.8 shows a picture of CMUTs fabricated with this approach. After the fabrication and characterization of these devices using different effective areas for the top electrode, we concluded that the performance of the CMUT cell has no evident impact regardless if open areas on the electrodes are patterned or not. This confirms the excellent adhesion between Chromium and SU-8 reported by [117].

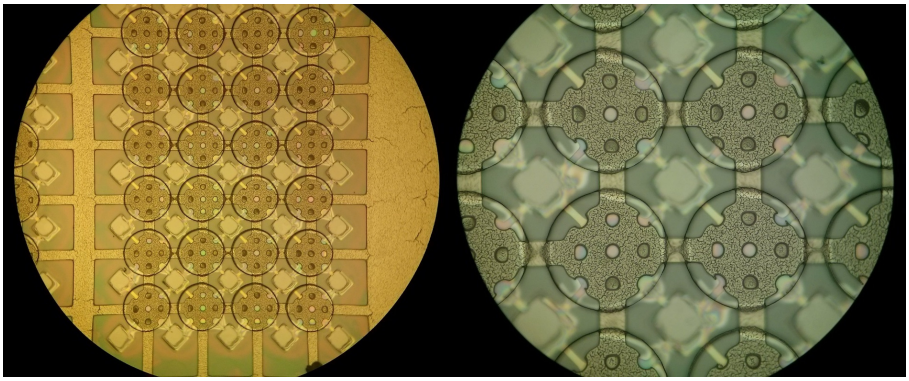

Figure 4.8: PolyCMUTs with embedded electrodes in the membrane. Electrodes with different effective areas were tested to assess the adhesion of chromium and SU-8. No delamination problems were encountered.

The final polyCMUT array had a series of modifications which we called generations. Departing from the conceptual design to the final prototype we developed six generations briefly described below and summarized in Figure 4.9.

- Generation 1 was a proof of concept that polymers (specifically the photopolymer SU-8) can be used to fabricate working CMUTs for immersed applications; the metal electrode is located on top of the membrane, requiring large actuation voltages. A pull-in voltage of 731V was predicted by the model developed in section 2.2.1.

- Generation 2 is a large array consisting of 24 asymmetric CMUT elements. We faced delamination problems during the fabrication given that the elements do not have a physical separation between them. The elements were so close to each other that we faced problems accessing them electrically, destroying the electrodes in many occasions. A 3D printed structure was used to contain the oil during immersion tests.

- Generation 3 is a smaller asymmetric CMUT array with only four elements and different membrane shapes and sizes, still, the electrode was positioned on top of the membrane. At this point, we considered the idea of relocating the top electrode as simulations revealed that the pull-in voltage could be greatly reduced while still maintaining the operational frequency in the MHz range.

- Generation 4 was used as a proof of concept that the top electrode can be embedded inside the membrane to decrease the effective electric

gap between electrodes. The embedded electrodes had openings for bonding the first and second SU-8 membranes, varying the effective electrode area from 50% to 100%. No delamination between the layers was presented during operation.

- Generation 5 is an array of five CMUT elements with buried electrodes, the array was diced and interconnected to a PCB before sealing the device in parylene-C; this avoided any damage to the CMUT electrodes during actuation.

- For generation 6, we included the effects of a layered membrane in our macromodel from section 2.2.1 to capture the effects of the sealing parylene-C layer in the estimated resonant frequency. We successfully fabricated a linear array of 64 and 128 polyCMUT elements; similarly, the arrays were dice cut and mounted on a customized PCB interface before sealing.

A customized PCB interface was designed using Altium designer (California, USA) and is shown in Figure 4.10. It was designed to allocate linear arrays of 32, 64 and 128 CMUT elements in a fan-out design. The electrical connections for each elements are located on alternate sides of the PCB, minimizing the potential electrical noise between elements.

In order to create an electrical interconnection bewteen the polyCMUT array and the PCB interface, a semi-automatic wire bonding machine West-Bond 747630E (Anaheim, CA, USA) was used. An aluminum wire with diameter of 25$\mu$m was used. Several adhesion problems were encountered when bonding the wire to the polyCMUT electrode. Figure 4.11 shows the

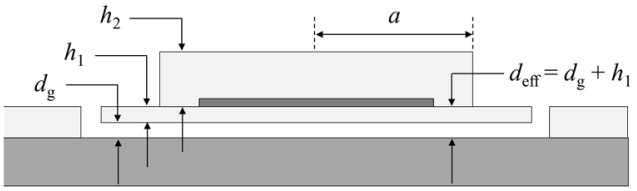


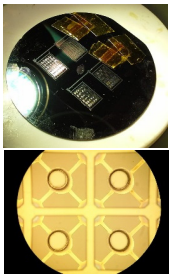

**Generation 1**
$a$ = 50µm
$d_g$ = 1.4µm
$h_1$ = 10µm
$h_2$ = NA
$f_R$ = 4.3MHz
$V_{max}$ = 584.8V
$FF$ = 9.1%
Proof of concept: CMUTs created with polymers

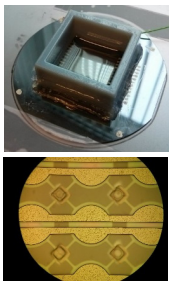

**Generation 2**
$a$ = 75µm
$d_g$ = 1.1µm
$h_1$ = 7µm
$h_2$ = NA
$f_R$ = 2.72MHz
$V_{max}$ = 154.4V
$FF$ = 19%
Asymmetric array, delamination problems

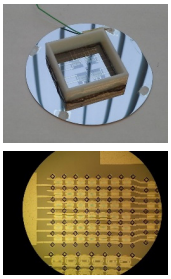

**Generation 3**
$a$ = 75µm
$d_g$ = 0.48µm
$h_1$ = 7µm
$h_2$ = NA
$f_R$ = 2.03MHz
$V_{max}$ = 152.8V
$FF$ = 26.7%
Asymmetric array with several membrane shapes

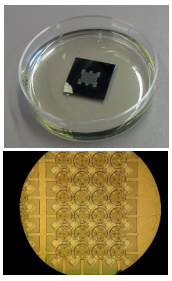

**Generation 4**
$a$ = 60µm
$d_g$ = 0.58µm
$h_1$ = 0.98µm
$h_2$ = 6.04µm
$f_R$ = 3.34MHz
$V_{max}$ = 96V
$FF$ = 35%
Proof of concept: Buried electrodes

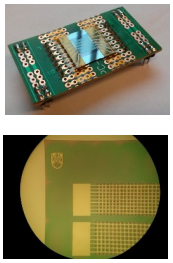

**Generation 5**
$a$ = 60µm
$d_g$ = 0.52µm
$h_1$ = 0.95µm
$h_2$ = 1.42µm
$f_R$ = 1.44MHz
$V_{max}$ = 77.6V
$FF$ = 37%
PolyCMUT array, 5 elements, different membrane size

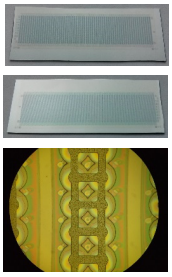

**Generation 6**
$a$ = 50µm
$d_g$ = 0.30µm
$h_1$ = 0.68µm
$h_2$ = 2.62µm
$f_R$ = 2.83MHz
$V_{max}$ = 48V
$FF$ = 58.9%
polyCMUT linear array, 64 and 128 elements

$FF$ = Fill factor, $V_{max}$=(0.8)$V_{PI}$

Figure 4.9: Table showing the different generations of polyCMUTs fabricated for this project. The fill factor in the elements was gradually increasing while lowering the operational voltage.

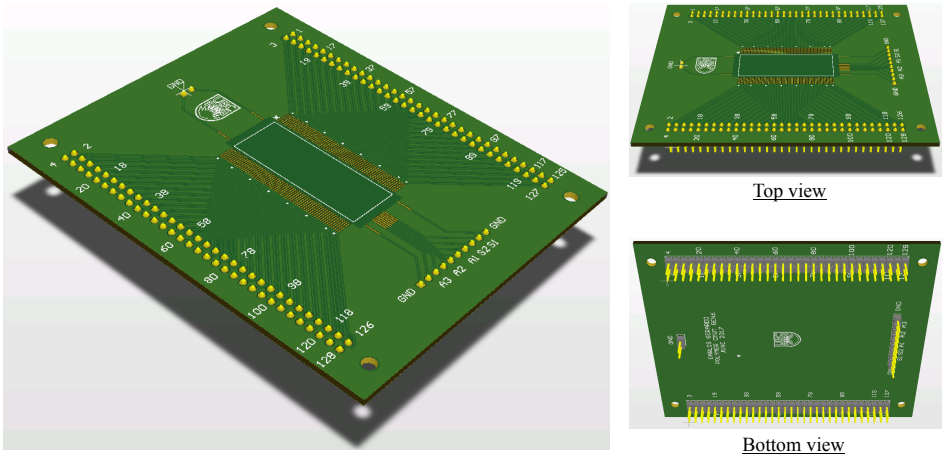


(a)

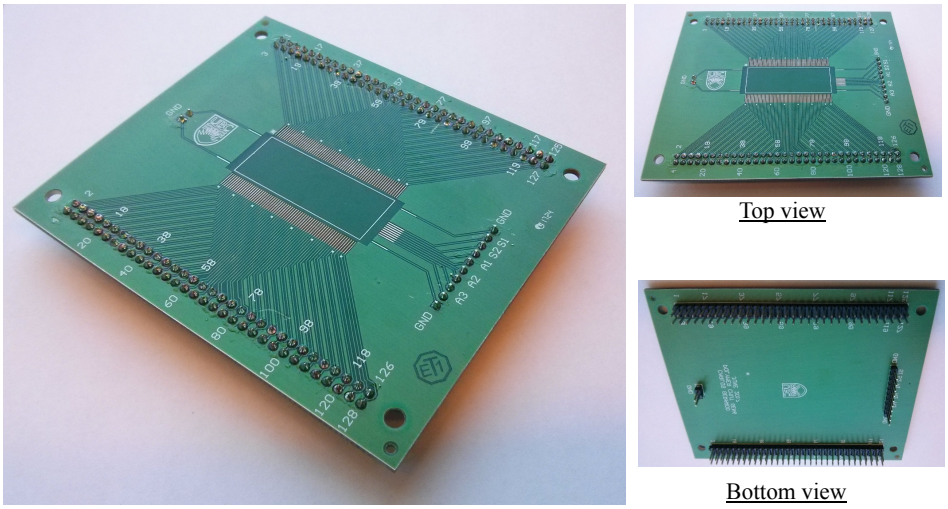


(b)

Figure 4.10: PCB interface for polyCMUTs linear array. Electrical connections located at bottom of board. (a) Render model designed in Altium, (b) Real prototype.

result when the wire bonder system was used. Since the bonding method is ultrasonic, the bonding tool applies a force and induce ultrasonic vibrations to deform the wire and attach it to the substrate. However, the results

indicate that the electrode thickness of this device (0.3$\mu$m) is too thin to withstand the bonding forces and vibrations. After modification of the force and the vibration time in the tool, only a few successful bonds were achieved, while the majority of the attempts ended in damaged electrodes as shown in Figure 4.11.

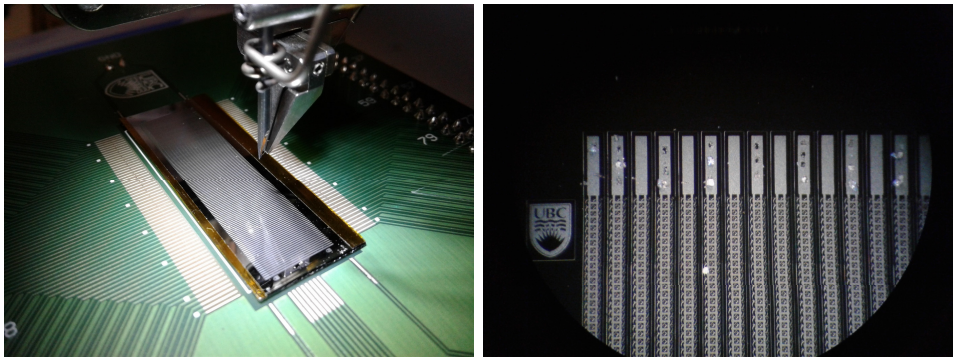

Figure 4.11: PolyCMUT linear array being wire bonded to interface PCB using aluminum wires. Forces on the bonding tool damaged electrodes on the surface of polyCMUTs with only a few successful bonds.

A different approach to create the electrical interconnections had to be performed for this prototype. Two pieces of thin polyamide film were used to create a physical bridge between the silicon chip and the PCB interface. Traces of silver nanoparticles ink were deposited to create electrical connections; this process was repeated multiple times to create a stack of silver ink layers until highly conductive traces ($\sim 4\Omega$) were obtained. The results are shown in Figure 4.12.

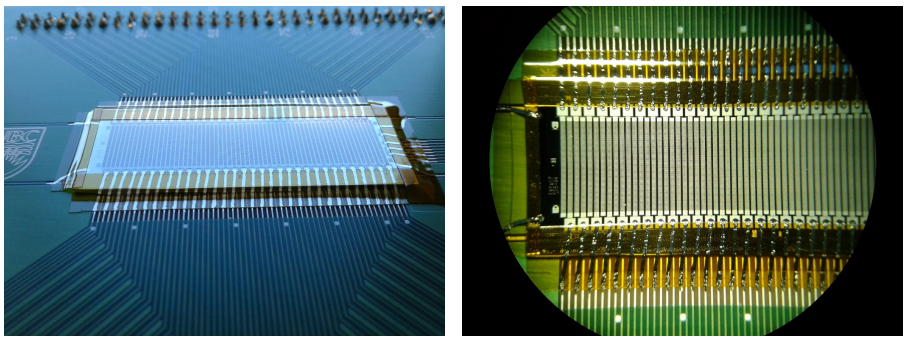

Figure 4.12: PolyCMUT linear array connected to interface PCB using flexible Kapton film and high-purity silver ink.

## 4.5 Results and Discussion

### 4.5.1 Optical characterization

Each CMUT element contains 4x75 polyCMUT cells with a pitch of 550$\mu$m between elements. The top electrodes on each element are interconnected in parallel. We characterized the frequency response of the sealed device in air using a laser doppler vibrometer OFV-5000 (Polytec, Irvine, CA, USA). The frequency response of the system and the first vibration mode are shown in Figure 4.14, yielding a quality factor of 40 in air. The predicted behavior using the developed model in section 2.2 is in good agreement. The topography of the final device was characterized using a white light interferometer (Polytec, Irvine, CA, USA) and is shown in Figure 4.15 with the thick SU-8 membranes of the CMUT cells displayed in blue.

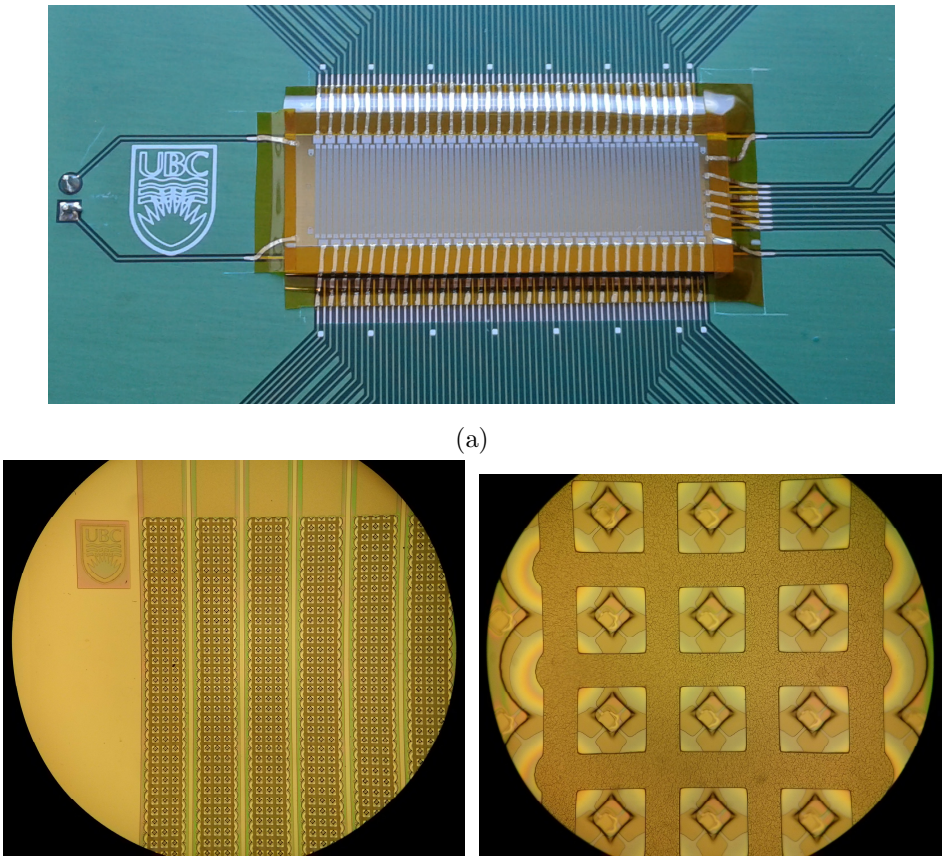

(a)

(b) (c)

Figure 4.13: (a) 64 element CMUT linear array mounted on PCB. (b) Six CMUT elements separated by a pitch of 550 $\mu$m. (c) CMUT cells showing interconnected top electrodes and cavities underneath, the optical transparency of SU-8 allows a visual identification of any possible defect.

### 4.5.2 Validation of operation

The CMUT array was immersed in a tank filled with mineral oil to avoid any electrical short circuits between wirings. A curved C5-2 broadband piezoelectric ultrasound probe (BK Ultrasound, Richmond, CA) was used as an acoustical source; using an aperture of 64 elements to send a focused

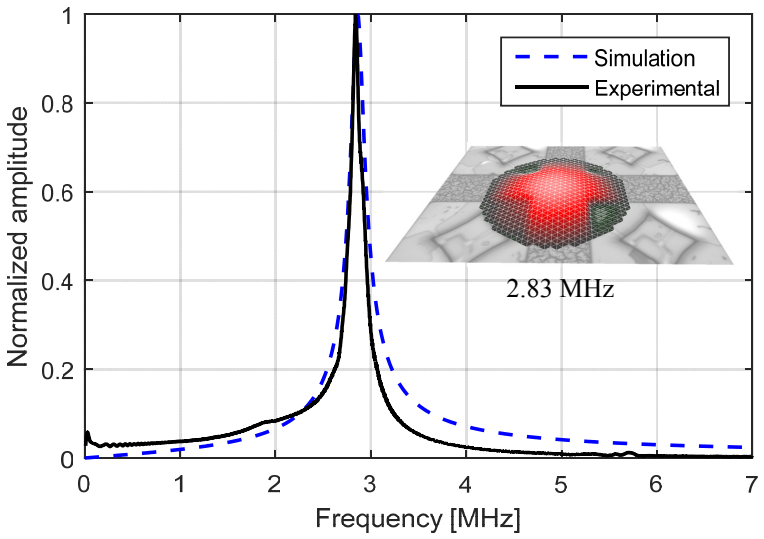


Figure 4.14: In air characterization of polymer CMUTs showing the first vibration mode at 2.83 MHz.

ultrasound beam to the polymer CMUT array placed 50mm beneath as shown in Figure 4.16.

A 50V square wave was applied to the piezoelectric transducer to generate a single focused ultrasound wave that arrives perpendicular to the CMUT membranes. The measured pulse on the CMUT is shown in Figure 4.17 under different biasing conditions. An external bias of 10V was applied through a bias-tee. The pre-bias condition is explained in the section 4.5.3.

The Fast-Fourier Transform (FFT) of the measured pulse reveals that the 6dB fractional bandwidth of this device is 101.6% around the center frequency of 1.525 MHz. This bandwidth for CMUTs is attributed to the relatively low fill factor of the design (59%), given that each individual cell pushes the fluid sideways, as well as in the normal direction. As a result,

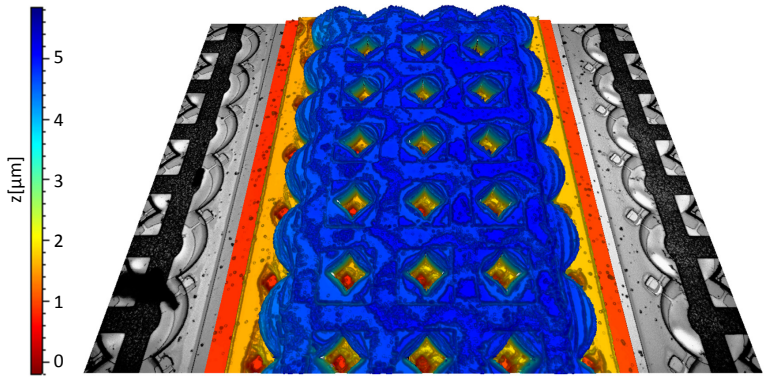


Figure 4.15: Static topography of a CMUT element using a white light interferometer.

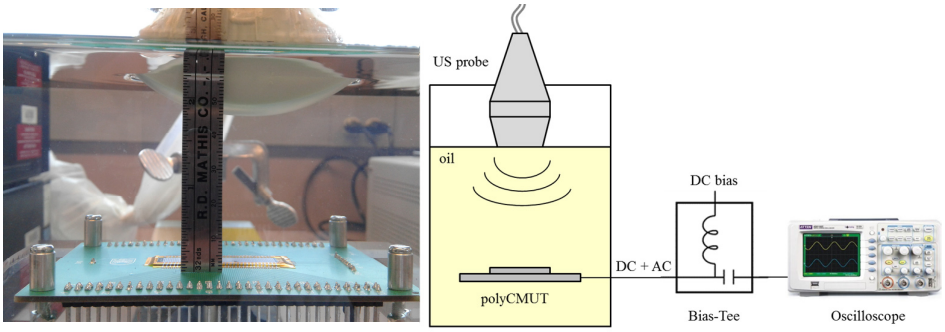


Figure 4.16: Experimental setup for polyCMUTs. An external piezoelectric probe used as acoustic source. The polyCMUT array was connected to bias-tee for echo detection.

the hydrodynamic mass of the fluid for each cell increases and, therefore, reduces the center frequency and bandwidth [12].

An endurance test was performed in order to asses the durability of the fabricated device. A 2MHz sine wave superimposed on a $10V_{DC}$ was used to excite the polyCMUT linear array using a pulse repetition frequency of 5 kHz. The piezoelectric probe acted as receiver and recorded the detected

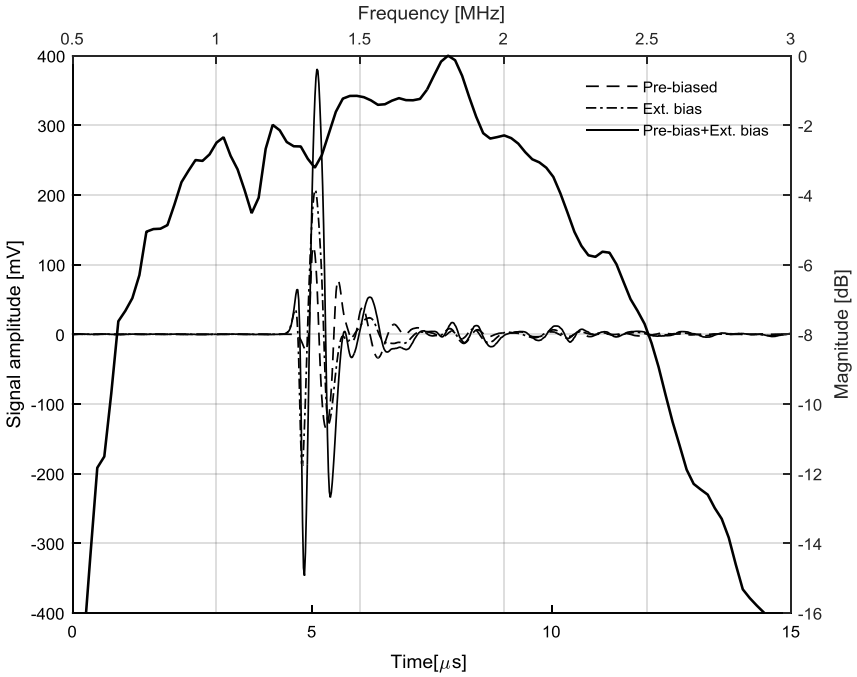


Figure 4.17: Acoustic response in mineral oil from polymer-based CMUT and FFT of received acoustic pulse showing a 101.6% fractional bandwidth.

pulses every 30 minutes for a period of 12 hours of continuous operation, the results are shown in Figure 4.18. Even though the polyCMUT array underwent over 200 million excitation cycles, the amplitude of the signals stayed within 95% of the maximum detected peak. Further endurance tests involving high temperatures and elevated voltages are still under way.

### 4.5.3 Pre-biasing

Charge trapping in CMUTs occurs when electrical charges are trapped in insulating layers in a CMUT membrane. This phenomenon was initially considered as a negative effect in CMUTs because it shifts the resonant

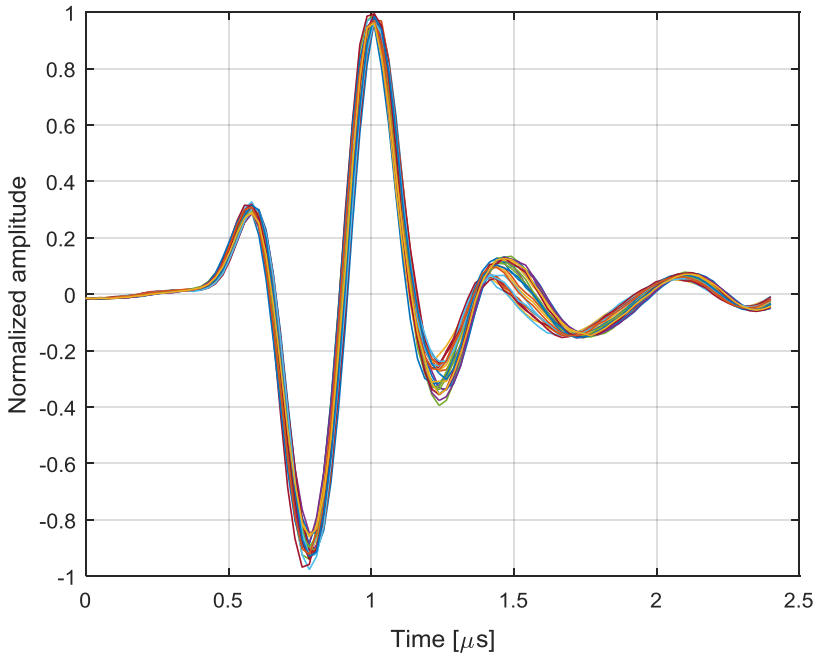


Figure 4.18: Ultrasound pulses generated by polymer CMUTs recorded every 30 minutes for a period of 12 hours. Signals stayed within 95% of the maximum detected peak

frequency of the membrane over time [122]. However, Park et al. [123] demonstrated that these electrical charges in CMUTs can be introduced in a well-controlled manner and used to operate a CMUT without any DC bias applied. The main benefit of having electrical charges trapped in the CMUTs is that they act as a built-in bias voltage, which suggests that only a small external DC voltage (compared to the required voltage if no trapped charges were present) is required to bring the membrane closer to the bottom electrode, i.e. the effective gap between electrodes is reduced, thereby increasing its capacitance. As this effective capacitance is increased, a small perturbation to the membrane deflection caused by external acoustic sources

will result in a large variation in the capacitance. Direct detection, without amplification of ultrasound waves coming from the same piezoelectric transducer described in the previous section, was possible thanks to this pre-biasing condition. Even though no external voltage is applied between the CMUT terminals, a 260mVpp echo signal was detected, as shown in Figure 4.17.

The first SU-8 layer described in the fabrication steps has a dual purpose. First, it serves as an insulation layer between the top and bottom electrode, preventing a short circuit in case the membrane is brought in contact with the bottom electrode. Second, the SU-8 layer acts as a novel charge trapping layer. For the first time, SU-8 was used to retain electrical charges, acting as a built-in bias voltage.

As determined by experimentation, electrical charges are trapped in the CMUT membrane and create an intrinsic (built-in) bias voltage. This contributes to the natural deflection of the CMUT membrane and, therefore, lowers the external DC bias voltage required for actuation and reception. Following a similar procedure as used by Park et al. [123], the CMUTs were "charged" by applying a DC voltage of 100V between the top and bottom electrodes for 5 minutes. During this time, the membrane collapsed against the bottom electrode, generating an electric field strength of 1.49 MV/cm. After removing the bias voltage, the CMUT was connected to an impedance analyzer to obtain a C-V curve. The symmetry point of this C-V curve revealed that an intrinsic (built-in) voltage of 8.9V was present. From this, an average trapped charge of 7.25 x 10-8 C/cm$^2$ was calculated. Larger intrinsic bias voltage could be experimentally obtained by charging

the CMUTs for longer periods of time, e.g. charging the CMUT for 210 min leads to a 30V pre-bias condition.

Figure 4.19 shows the different charging curves for the discussed poly-CMUTs. It can be appreciated that each charging cycle injects trapped charges in the membrane-electrode interface, creating the effect of an intrinsic bias voltage. This in turn decreases the pull-in voltage of the membrane as appreciated in the graphs on the right. This effect is completely reversible if the terminals on the charging station are inverted. Similar results were obtained in [123], where the authors successfully charged and discharged CMUTs.

The SU-8 membrane is naturally deflected towards the bottom electrode as a result of the atmospheric pressure. This serves to bring the top and bottom electrodes closer to each other, thereby increasing the capacitance. As the membrane become increasingly thin, this effect is increased [124]. Figure 4.20 shows the contribution of different effects towards the total deflection of the membrane. Atmospheric pressure is a major influence. Naturally developed by sealing the cavity in a vacuum chamber, atmospheric pressure deflects the membrane 82nm (27% of cavity height) towards the bottom electrode. The pre-biasing condition (built-in bias voltage) increases the deflection by 1.5%. Lastly, the contribution of the external bias voltage increases the total membrane deflection to a maximum of 32.1% of the cavity height.

By embedding the electrode inside the membrane, we were able to obtain a pull-in voltage of 65V, which contrasts with the 220V required when the metal electrode was placed directly above the CMUT membrane as in

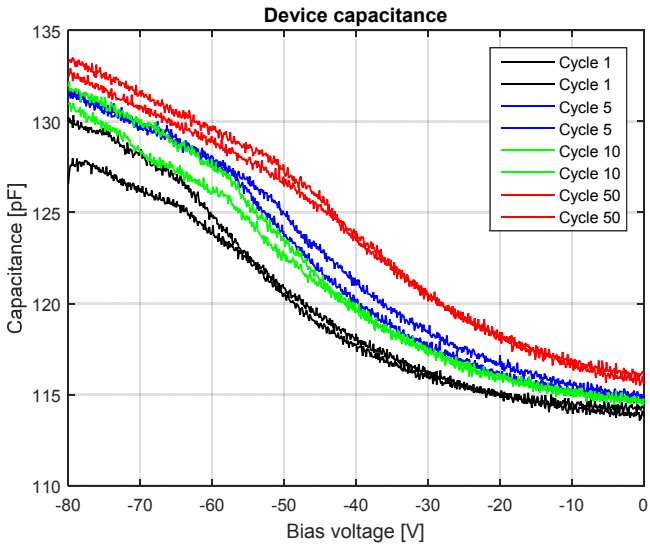


(a)

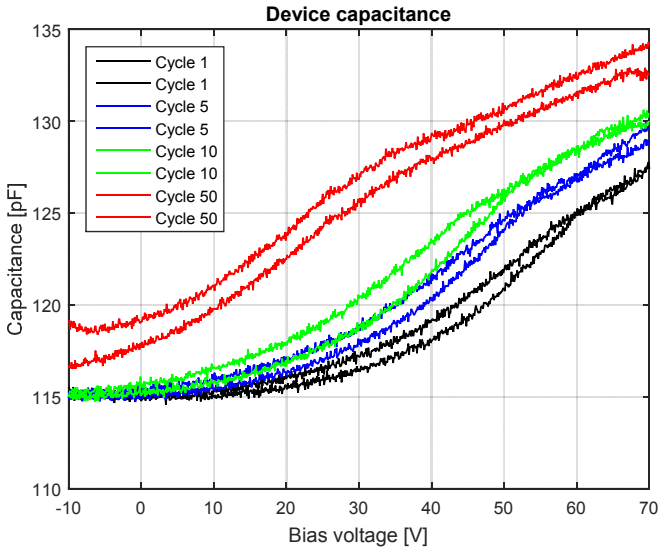


(b)

Figure 4.19: PolyCMUTs C-V charging curves. The intrinsic (build-in) bias is inferred from symmetry lines in C-V curves. (a) Negative charging, (b) Positive charging.

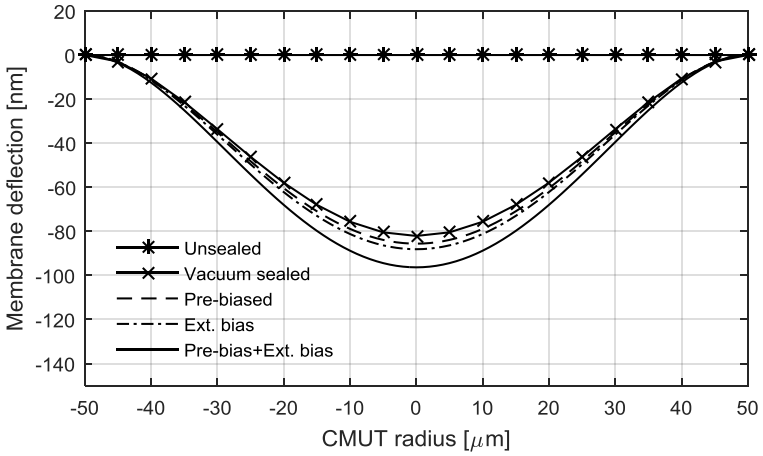


Figure 4.20: Contribution of different factors towards the total CMUT membrane deflection.

traditional CMUT designs.

### 4.5.4 B-mode imaging

The feasibility of using these polymer-based CMUTs for the creation of B-mode images was assessed. An array of 12 aluminum wires with a diameter of 600$\mu$m equally spaced by 5 mm was used as a target in a tank filled with mineral oil as shown in Figure 4.21a and 4.21b. The linear CMUT array was placed directly above the wires and excited by a 12 $V_{PP}$ square pulse that was oscillated at 2MHz and superimposed on a 10 $V_{DC}$ bias using a bias-tee. This external bias voltage was selected in order to avoid pull-in in case the CMUT was charged for a long period of time.

Only one CMUT element was used during transmit, thereby creating a quasi-cylindrical wavefront. The echoes created by the aluminum wires were captured by all other elements. For receiving, a 10$V_{DC}$ bias was applied

to the CMUT using a bias-tee. The echoes were measured by a digital oscilloscope, and averaged over 256 times to reduce electrical noise.

The received signals were later processed in MatLab (Natick, MA, USA) using synthetic aperture beamforming techniques [125]. A simple Hanning window was applied as apodization and no time-gain compensation (TGC) processing was used. A B-mode image generated using polymer-based CMUTs is shown in Figure 4.21c. Despite the unamplified measurement scheme, all of the 12 wires in the phantom can be identified to a depth of 85 mm. The signal profiles of the first 5 wires of the phantom were taken in order to assess the lateral resolution of the polymer-CMUT array as shown in Figure 4.21d, the full width at half maximum (FWHM) revealed a resolution of less than 1.5mm.

As a simple comparison, the same wire phantom was scanned using two different commercial piezoelectric probes. We used a C5-2 curved linear array and an L14-5 linear array, both from Ultrasonix (Richmond, BC, CA). The results are shown in Figure 4.22. Although not a direct comparison, this test was intended to highlight the potentials of this new technology. The commercial piezoelectric-based required high voltages ($\sim$100V), have integrated sensitive electronics and voltage amplifiers; whereas our technology uses low voltages and no amplification electronics.

A slight modification in the process can lead to the fabrication of poly-CMUTs on flexible substrates. Polyimide is a good candidate for this purpose given its elevated thermal stability, strong chemical resistance and potential biocompatibility [126, 127]; moreover it has an excellent adhesion to metals and SU-8 films [117, 128, 129]. This polyimide film needs to be

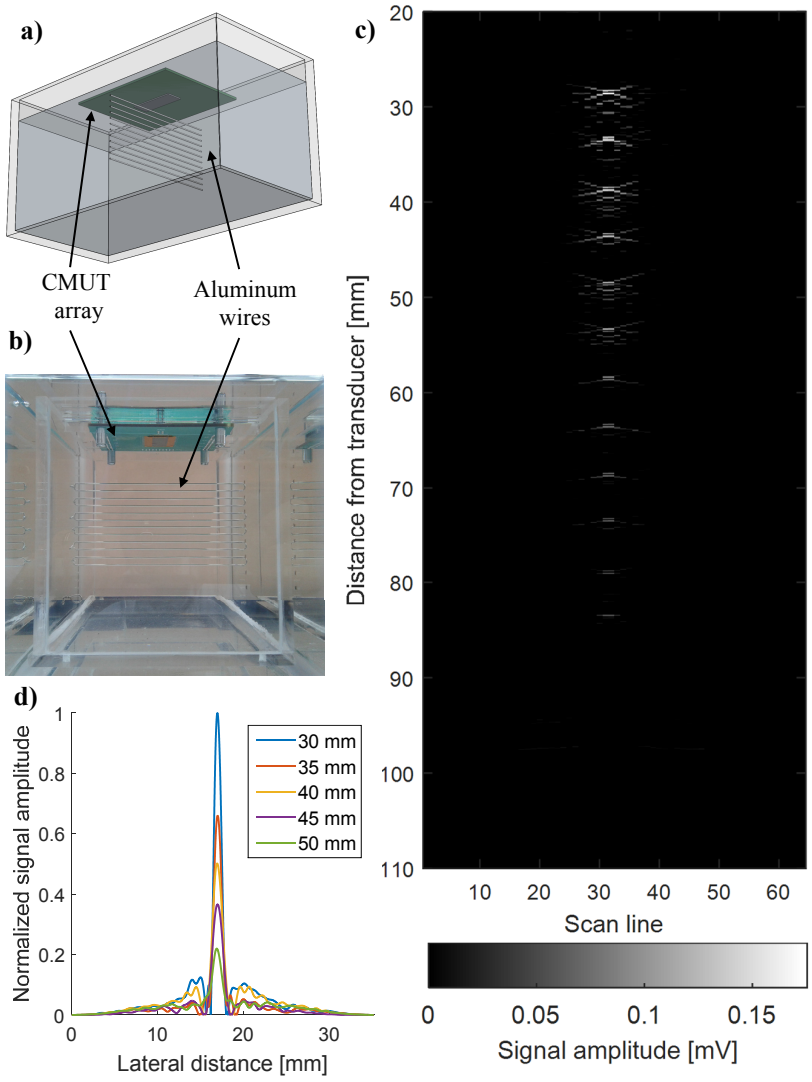


Figure 4.21: (a) Diagram of the wire phantom used; 12 aluminum wires spaced by 5 mm. (b) Photograph of the actual wire phantom immersed in mineral oil. (c) B-mode image of a wire phantom using a linear array of polymer-based CMUTs using a display dynamic range of 30 dB. (d) Assessment of the lateral resolution, the FWHM for the first 5 wires down to a depth of 50 mm was less than 1.5 mm.

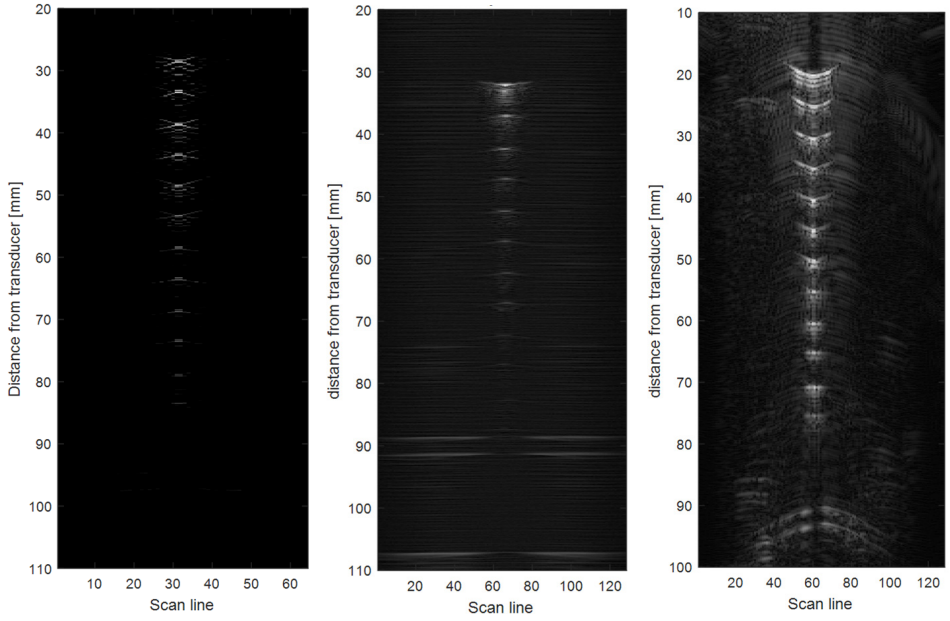


(a) (b) (c)

Figure 4.22: B-mode comparison of a wire phantom array using (a) poly-CMUT linear array, (b) Commercial L14-5 piezoelectric probe, (c) Commercial C5-2 piezoelectric probe.

temporary fixed to a rigid carrying substrate prior to implementing the fabrication steps outlined in this chapter. A quick experiment was performed to asses the fabrication of SU-8 structures on Kapton films. Figure 4.23 shows calibration features patterned in SU-8 using a maskless lithographic system. A full fabrication approach involving polyCMUTs is still under investigation.

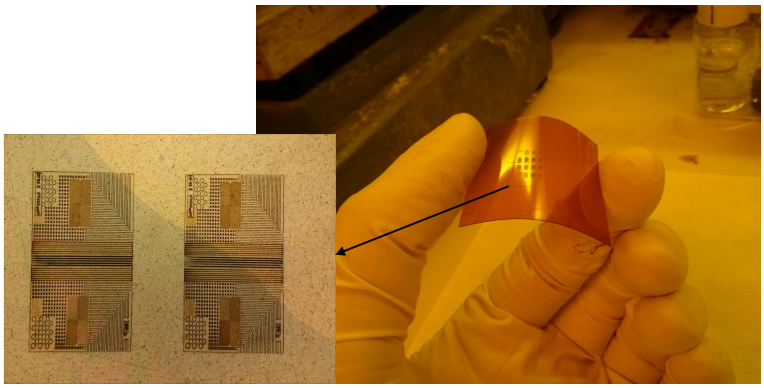

Figure 4.23: Adhesion test of calibration featured patterned in SU-8 on flexible Kapton film.

## 4.6 Discussions and conclusions

This work provides a proof of concept that a polymer can be used to fabricate CMUTs for biomedical imaging. Having the top electrode embedded inside the membrane led to low operational voltages comparable to traditional CMUTs fabricated in polysilicon or silicon nitride. A 64 element CMUT linear array was successfully operated and characterized, leading to the first demonstration of a B-mode image created with polymer-based CMUTs.

An advantage of using Omnicoat as sacrificial material is that the deposition method is simple and controllable. The thickness of this layer can be reduced to a few tens of nanometers if desired, leading to potentially increased sensitivity and even lower operational voltages. This is the first demonstration where a condensed version of Omnicoat is selectively patterned and used as sacrificial layer for SU-8.

By encapsulating the electrode inside the membrane, instead of being on top, polymer-based CMUTs (polyCMUTs [4]) were able to obtain low operational voltages and frequencies that were comparable to traditional CMUTs fabricated in silicon nitride or polysilicon.

The total estimated amortized manufacturing cost for the prototype polyCMUT array presented is below $100 USD. This is due to both the low cost of the materials used and the minimal manufacturing equipment required (mask aligner, metal evaporator, critical point dryer). Because the device is vacuum-sealed, the effective capacitance of the device is naturally increased by the atmospheric pressure as it deflects the membrane 27% of the total cavity height. Preliminary results indicate that these polymer-based CMUTs can be pre-biased such that they can be operated even as passive devices (no external power) during reception and with low excitation voltages ($10V_{DC}$ + $12V_{AC}$) during transmission.

The materials and solvents used during manufacturing have low toxicity, and the sealing layer covering the device is considered to be biocompatible. The maximum process temperature used was 150°C, meaning that polyCMUTs can be potentially fabricated directly on top of substrates containing pre-existing components, such as beamformers and Tx/Rx switches. No acoustic matching layers were used. A novel sacrificial layer with high etching selectively was used, that can be spin or spray coated over rigid or flexible substrates, for wearable applications. The manufacturing process can be theoretically scaled up to roll-to-roll fabrication, decreasing the

[4] A patent application was filed and the results of this chapter appear on [130]. Also see www.polycmut.com

costs even further.

The materials used were selected in such a way as to manufacture CMUTs inexpensively, minimize the fabrication steps, and obtain similar dimensions comparable to traditional CMUTs [47]. This work highlights the benefits of using a simple fabrication process with inexpensive materials coupled to basic microfabrication equipment. Although SU-8 photopolymer was used for this study, any other polymer or soft material can in principle be used for the fabrication of CMUTs. The important factor is to maintain a small effective gap between the electrodes of polyCMUTs for low operational voltages and high sensitivity. A full acoustic characterization for the presented polyCMUTs is yet to be done. Performance tests for these devices are under way to create a pre-biasing mathematical model.

This technology has the potential to be extended to flexible substrates intended for conformal and wearable health monitoring systems [68, 69]. This contrasts with traditional fabrication approaches that use a combination of semiconductors and metals as structural materials. Although flexible CMUT arrays have been derived from rigid substrates [131, 132], problems have been reported with electrical interconnections of individual elements getting cracked. An advantage of this design is that the low temperature process (max 150°C) can be seamlessly integrated with CMOS compatible processes for closer integration with electronics. SU-8 can also be easily coupled with other materials, such as polydimethylsiloxane (PDMS) or polymethylmethacrylate (PMMA), for microfluidics applications [133, 134].

A variation of the proposed fabrication methodology is to create the same version of polymer-based CMUTs using wafer-bonding technologies for

SU-8, as reported by Joseph et al. [135]. The fabrication methodology can also potentially be extended to roll-to-roll technology [136], where CMUT cavities and membranes are defined on separate flexible substrates and then bonded together under a vacuum environment. This could decrease production times and costs even further, with the possibility of fabricating ultra-low-cost ultrasound transducers.

This chapter presented the design, fabrication and characterization of polymer-based CMUTs. Even though both designs for symmetric and asymmetric cells were tested, we emphasized our efforts into the symmetric CMUTs. This is because the symmetric mode can be readily developed into an ultrasound imaging system with standard front-end and back-end hardware, including standard beamforming techniques.

Now that we have demonstrated that we can create polyCMUTs using the photopolymer SU-8, we consider next whether we can alter the properties (functionalize) SU-8 for other related purposes. The next chapter shows a new method to functionalize SU-8 to create electronic components on a flexible substrate.

# Chapter 5

# Polymer-based fabrication techniques for integrating electronic subsystems

Parasitics arising from interconnecting paths between CMUTs and electronics decrease the overall SNR. The performance of CMUTs might be boosted if interconnection lines and potential electronic components can be fabricated on the same substrate and as close as possible to the CMUTs using similar fabrication materials. This chapter explores the possibility of fabricating polymer-based interconnection lines and planar electrical components on flexible substrates to be coupled with CMUTs.

The advantages of having embedded components on substrates is that polyCMUTs can be fabricated right above them, creating a direct interconnection and minimizing the footprint. This is advantageous if the target is to have a small-size and low-power ultrasound imaging system. Before a full integration can take place, it is necessary to assess the viability of fabricating interconnection lines and passive components using materials other than metals.

## 5.1 Functionalized materials

Composite materials exhibit properties that cannot be found with metals, polymers or ceramics alone. In particular, metallic nanoparticles embedded in polymers have become increasingly popular because of their ability to maintain the electrical properties in the metallic range while maintaining the flexibility and some unique properties of polymers such as bio-compatibility, chemical resistivity, optical transparency, photo-sensitivity, etc. These composites materials do not have the drawbacks of pure metals such as high density, low chemical resistance and complex manufacturing process.

The electrical conductivity of these composite materials depends strongly on the type of filler and the proportion and average size of the particles. As outlined by [137], the large surface area of small particles allows conductive SU-8 to be obtained with a lower concentration of particles. The point in which the polymer matrix with fillers starts to become electrically conductive is known as the percolation threshold [138]. After this point, an increased amount of conductive fillers in the polymer matrix leads to a smaller increase in the electrical conductivity.

Photoresists are good candidates to be mixed with these metallic particles; they are chemically inert, mechanically stable and can be easily spin coated. Photoresists, such as epoxy-based SU-8 [106] have a broad range of use, such as fabricating high-aspect ratio structures, molds and microfluidics channels. The incorporation of particles in the nanoscale range can be used to tailor specific electrical, optical, or mechanical properties, broadening the applications for this material.

Conductive SU-8 can be obtained by mixing silver nanoparticles [137, 139], carbon black powder [140, 141], single and multi-walled carbon nanotubes [142–144], graphene [145], conductive organic components [146], gold and even diamondoids [147]. Depending on the type of filler, the mechanical, optical and electrical properties of the fabricated device are affected [147].

One of the main limitations of the addition of metal nano-particles in SU-8 is the increase of light absorbance, reducing the photo-polymerization depth. In this work, silver was selected as metallic filler for its low absorption in the near UV range, as outlined in [148], allowing us to obtain thin conductive traces.

Some of the reported applications of conductive SU-8 include strain sensors [149, 150], pressure sensors [144], biochips for electrografting [141], and as conductive material for inkjet printable applications [143]. Preliminary work involving circuit interconnection lines has only been reported in [151], where the conductive mixture of silver and SU-8 was deposited using a scraper and then back-side exposed through a quartz substrate; the patterned traces had a resistance variation from 800$\Omega$ to 10k$\Omega$ due to the inhomogeneity of the composite structures. The fabrication of passive elements using functionalized (or conductive) SU-8 has not yet been reported in the literature.

A new fabrication approach to create planar passive devices and circuit interconnects with the possibility of miniaturization is presented, it is also shown how this technique can lead to obtain highly conductive lines as small as 5$\mu$m; leading to the potential fabrication of sensing and communication

devices such as in [152]. The feasibility of fabricating planar resistors and capacitors on flexible substrates using the developed functionalized SU-8 is explored. This approach simplifies the standard commercial fabrication process of such devices, where they are normally fabricated by selectively etching metallic foils glued to flexible substrates. This technique also enables the fabrication of such devices on substrates that are sensitive to the conditions present in evaporation or sputtering systems for metal deposition; moreover fewer fabrication steps and required equipment are necessary when compared to traditional lift-off metal patterning techniques, translating into lower fabrication costs.

Typically, the number of passive components in a PCB is higher than the number of active components such as operational amplifiers and integrated circuits; therefore a high number of electrical interconnections are needed to wire these devices together, sometimes needing multiple layers for a proper connection. Embedded passive components can be fabricated between these layers to simplify the design and to reduce footprint. Further advantages include higher reliability, better electrical performance, decreased number of electrical interconnections and lower cost [153]. Perhaps the most important advantage of having passive elements on flexible substrates is that they meet the needs of the emerging flexible wearable devices manufacturing industry, an area forecasted to grow almost 67% in the next 3 years [94].

Because of its unique mechanical properties after curing, SU-8 has been widely used as structural material for the fabrication of microelectromechanical systems (MEMS) devices [154], allowing the creation of cantilevers, beam arrays and membranes. One of the goals of our research group is to

create operational MEMS devices and circuit interconnections using conductive SU8, allowing a hybrid integration with commercial integrated circuits and components; therefore we selected SU-8 as the material for passive components, circuit interconnections and the MEMS devices themselves. Some preliminary results have been published in [155], where suspended beams and membranes fabricated with conductive SU-8 are electrostatically actuated.

Being able to spin deposit and photo-pattern at high resolution conductive areas is of special interest for the microfabrication community, as it increases the flexibility in the fabrication process in areas of MEMS and microfluidics, where temperature-sensitive materials and processes are used and they would be otherwise incompatible with conventional metal deposition processing. Moreover, adhesion of metals to polymers is poor, requiring adhesion promoters to be used prior to metal deposition [156].

Modern electronics often require surface mounted elements to be attached to flexible circuits. The current flexible electronics industry allows circuits to be built using interconnection lines as small as 25$\mu$m using copper traces with a spacing of 50$\mu$m between lines [157]. These parameters usually come from the restrictions involved in their fabrication process (deposition and patterning of masking layer, wet etching using aggressive chemicals, etc). Our approach for the fabrication of circuits involves three major steps: spin coating of the sample using functionalized SU-8, UV exposure and sample development. An extra electroplating stage is beneficial for structures requiring a very low resistance value, such as inductors, interconnection lines or RF fractal antennas [158].

### 5.1.1 Functionalized SU-8 Preparation

Guided by the results obtained in [137] and [139], a formulation containing 25 wt % silver dispersed in SU-8 2005 was prepared by our research group. Silver nonparticles with an average size of 80nm were purchased from ACS Materials (Medford, MA, USA) and SU-8 2005 was acquired from Microchem (Newton, MA, USA). An accurate concentration of the mixture was obtained using a sensitive microbalance to incorporate the desired weight percentage of silver nanoparticles into the SU-8.

The silver nanoparticles were gradually introduced into the SU-8 while a high-speed mixer was used to evenly disperse the particles and minimize silver aggregation. This agitation process created unwanted air bubbles, which were later removed by immersing the sample in an ultrasound bath for 30 minutes. To avoid any silver sedimentation at the bottom of the vial, a spin bar and a magnetic stirrer at moderate speed was used to maintain a good dispersion of the particles in the sample prior spin coating. Some research groups use pre-treated silver nanoparticles to enhance dispersion in the mixture [138]; a few others add a small percentage of surfactant or extra solvents into the mixture to have a uniform distribution of nanoparticles [147].

The addition of silver nanoparticles into the SU-8 increases the viscosity of the mixture, increasing the expected film thickness. For example, the film thickness of ordinary SU-8 2005 spun at 1000 RPM on a silicon wafer was 7.2$\mu$m, and it increased to 10.6$\mu$m after the addition of silver particles for the same spinning conditions.

Several experiments were performed by varying the concentration of silver in the SU-8 with increments of 5%; where the percolation threshold was detected to be around 20%. After experimentation, we noticed some variation in the conductivity of the patterned traces in different locations of the same sample. We mitigated this phenomenon by using a slightly higher concentration of silver nanoparticles of 25% in the mixture. As a consequence, the conductivity became much more controllable, especially for fine traces; nevertheless the minimum patterned features increased in size as well as the required exposure dose. Initial experiments revealed a standard variation in the sheet resistance of $\pm 8.2\Omega/\square$ when a concentration of 20% was used. After the concentration was increased to 25% the standard variation in the sheet resistance dropped to $\pm 5.8\Omega/\square$. When the concentration of silver was 60% it was not possible to achieve any patterned traces on the substrate even when high UV doses were used; at this point the concentration of nanoparticles was so high that the UV light could not penetrate the entire thickness of the layer so it could be adhered to the substrate.

### 5.1.2 Sample processing

For the fabrication of planar inductors and capacitors, a piece of Kapton film (DuPont, Delaware, USA) with a thickness of 137$\mu$m was fixed to a silicon wafer for processing. Kapton was used because of its well known thermal resistance and electrical insulating properties; this particular thickness of kapton was chosen as it allowed an easy manipulation of the sample without inducing any damage. The sample was later spin coated with the prepared functionalized SU-8 2005 at 1000RPM for 30 seconds. A soft bak-

ing step on a hotplate at 95°C for 5 minutes was sufficient to evaporate the cyclopentanone solvent present in the SU-8, leaving the sample ready to be exposed.

The photomask design was exposed using a maskless lithographic system SF-100 Xpress from Intelligent Micropatterning (St. Petersburg, FL, USA), having a resolution of 0.6$\mu$m. The maskless lithographic system used for this project takes a photomask design in DXF format and divides it into exposure frames of 1300x800$\mu$m. During the exposure process, the frames are stitched by overlapping areas of 20 pixels per side. In order to avoid stitching defects we adjusted the stitched area exposure with a grayscale value of 178 for the side areas and 155 for the corner areas according to [159], enhancing the surface uniformity.

After exposure, the sample was post-exposure baked for 5 additional minutes and then developed for 1 minute in SU-8 developer in a gentle agitation environment. A short rinse in acetone and isopropanol helped to remove silver residues from the substrate. In preliminary work, we noticed that by spinning and baking a layer of ordinary SU-8 2005 before depositing the conductive SU-8 improved the adhesion of the fabricated devices, it also allowed us to achieve a smaller gap between features since the silver residues were able to be washed away more easily.

## 5.2 Experimental results

In order to calculate the sheet resistance of our conductive SU-8 films we used a cloverleaf design shown in Figure 5.1 following [160]. A four-probe

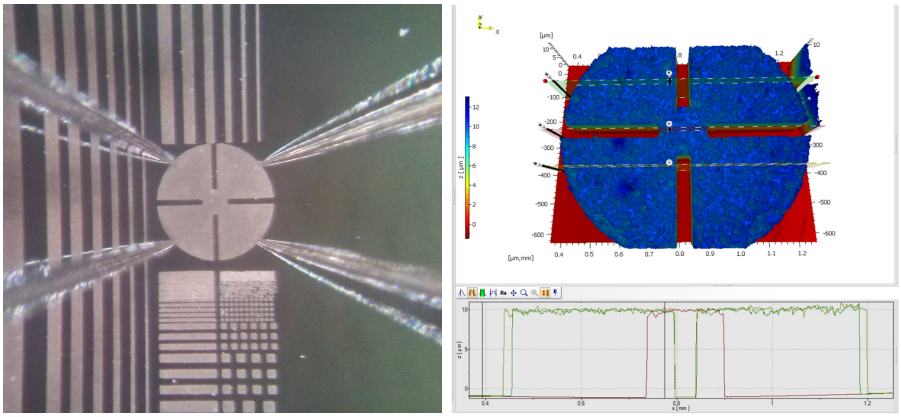

Figure 5.1: Cloverleaf design with conductive SU-8 for sheet resistance measurement. The topography on the right was measured using a white light interferometer.

measurement was used to measure the voltage drop on one side of the test structure due to a variation in the DC current flowing on the opposite side as shown in Figure 5.2. We determined that the sheet resistance of our conductive SU-8 layer (without electroplating) is 11.17 Ω/□ which matches the results obtained by [138].

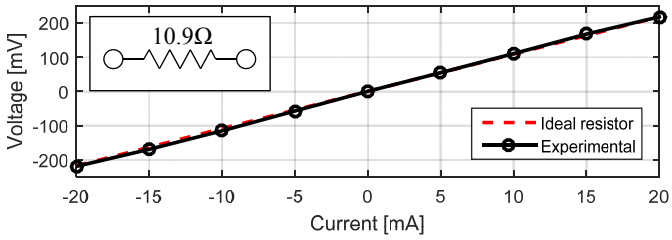


Figure 5.2: I-V graph showing a linear behavior for structures patterned using functionalized SU-8.

Designs of planar resistors and capacitors were fabricated using our func-

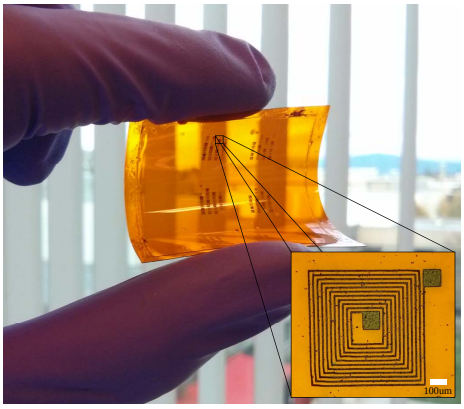


Figure 5.3: Array of microinductors fabricated using conductive SU-8 with the proposed fabrication technique. Microinductor with 5$\mu$m lines and 20$\mu$m spacing shown in the inset.

tionalized SU-8 on Kapton films. The last step in our fabrication process is to hard bake the patterned features at 200°C for 2 hours to increase the conductivity of the traces as described in [138]. We successfully fabricated microinductors by electroplating copper on the SU-8 traces to increase the electrical conductivity. By using a maskless lithographic system to directly pattern the interconnection lines, instead of a masking layer for etching, conductive lines as small as 5$\mu$m in width shown in Figure 5.3 were obtained.

We designed an RC array to be used as a low-pass filter built on a piece of Kapton film. The final resistor and capacitor are shown in Figure 5.4a. The silver nanoparticles dispersed in the SU-8 matrix can be seen in detail in Figure 5.4b.

We connected the RC circuit to act as a low-pass filter, a sinusoidal voltage with an amplitude of 10V was used as input. The frequency re-

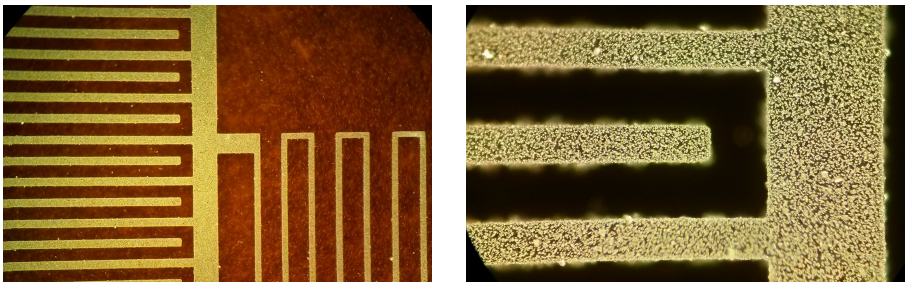

(a) (b)

Figure 5.4: **(a)** RC filter showing the capacitor on the left and the resistance path on the right. **(b)** Dark-field view of a capacitor finger showing the silver nanoparticles embedded in the SU-8 matrix.

sponse of the system is shown in Figure 5.5; where the measured cut-off frequency of this filter was 52kHz; a 20dB/dec attenuation clearly show the behavior of a first-order system. The estimated values for resistance and capacitance including the interconnection cable parasitics are 270kΩ and 11.33pF respectively.

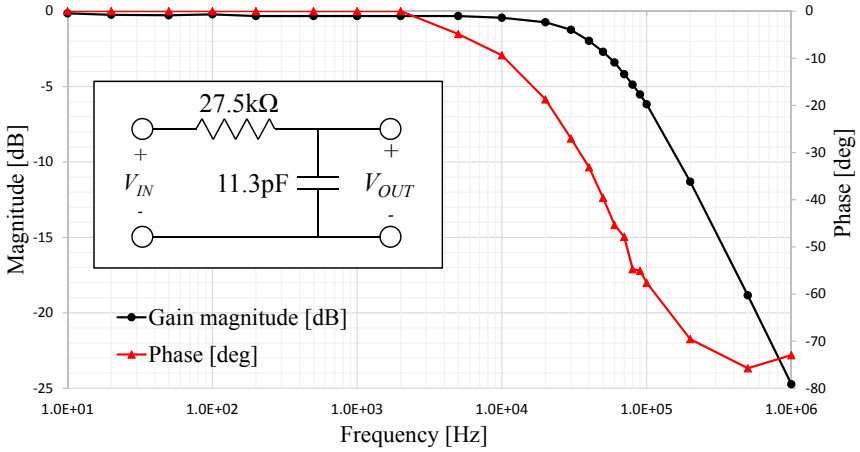


Figure 5.5: Experimental frequency response of a low-pass RC filter fabricated using conductive SU-8 on Kapton film.

A laser-based measurement scheme [161] can be used to assess the silver particle distribution on the sample, but it requires specialized equipment currently unavailable in our laboratory. For this purpose, we obtained dark-field images of unexposed conductive SU-8 in different regions of a sample, including the center and areas close to the edges. The silver particle density in the image was estimated using image processing techniques from [162], where the variation in density between different images was less than 3.5%. Figure 5.6 depicts the distribution of silver in the center of a sample compared to an area close to the edge.

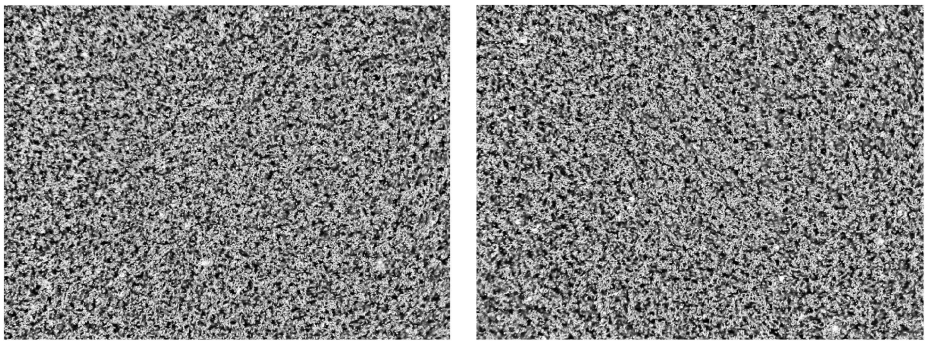

(a) (b)

Figure 5.6: Dark-field microscope images showing the dispersion of silver nanoparticles in different locations within a sample **(a)** Center of sample. **(b)** Area close to the edge of sample.

### 5.2.1 Copper electroplating

Conductive traces patterned using functionalized SU-8 can be used as a seed layer during an electroplating process to increase the electrical conductivity of the devices. To monitor the copper growth, a line with functionalized SU-8 measuring 100$\mu$m in width by 10mm in length was patterned; we

then immersed the sample in an electroplating bath maintaining a current of 1mA. The electrical resistivity and the topography were measured over time; a cross-sectional view of the electroplated line is shown in Figure 5.7. Figure 5.8 shows the rapid decreasing of the resistivity during the first minute of electroplating.

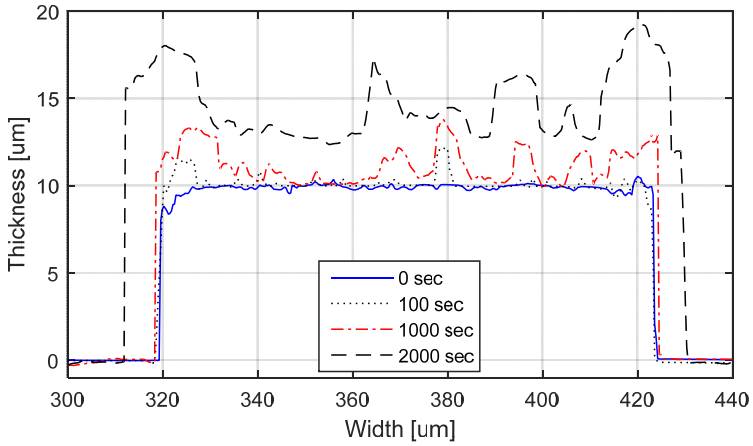


Figure 5.7: Cross-sectional view of the conductive line monitored for different electroplated times

### 5.2.2 Inductors fabrication

A copper electroplating process allowed us to decrease the electrical resistivity of planar inductors fabricated with functionalized SU-8. A low series resistance is necessary to create inductors with high quality factors. The electroplating time and current intensity allows the tuning to the desired conductance.

As an example of this fabrication approach, we replicated the design of a commercially available NFC (Near Field Communication) microantenna

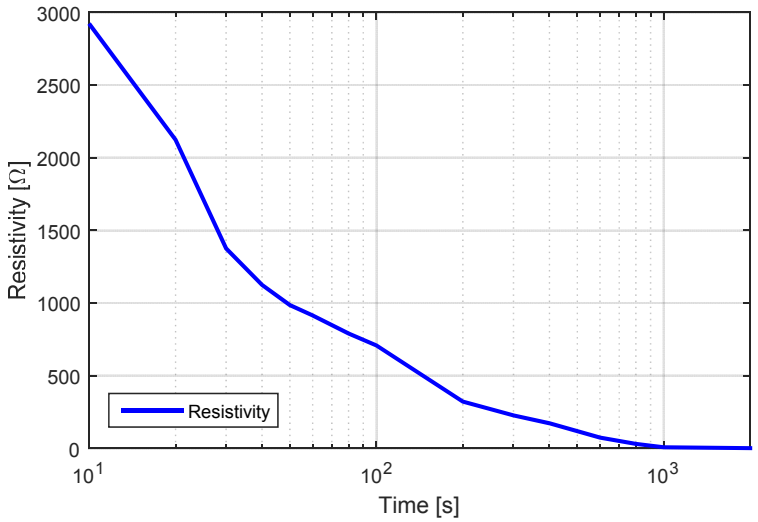


Figure 5.8: Resistivity variation of a 100$\mu$m conductive SU-8 line for a 1mA electroplating current.

[163] using our functionalized SU-8; this particular design has 9 turns of 80$\mu$m paths with 120$\mu$m spacing. The sample was electroplated for 2.5 hrs maintaining a low current of 1mA to improve the quality of the final copper layer. Figure 5.9 shows the final device as well as the details of the traces. Before electroplating, the sample had a series resistance of 34.6k$\Omega$; after electroplating the electrical resistance dropped to 10.2$\Omega$.

The topography of the inductor traces was measured using a white light interferometer (Polytec, Irvine, CA, USA). Figure 5.10 shows images of the same traces before and after the electroplating process. The outermost terminal of the coil was connected to the cathode in the electroplating setup. The deposition of copper began closest to the negative terminal and gradually propagated towards the center of the coil, meaning that the outermost

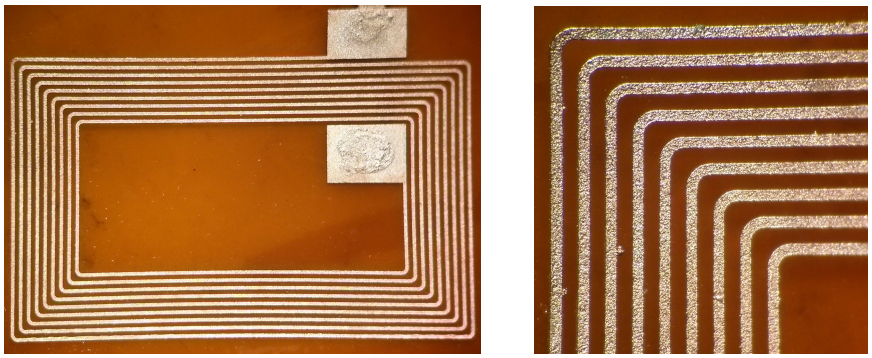

(a) (b)

Figure 5.9: **(a)** NFC antenna fabricated with functionalized SU-8 as a seed layer after copper electroplating.**(b)** Detailed view of electroplated traces.

turns of the inductor are slightly thicker and wider than the inner ones: 3$\mu$m is the maximum size difference in width.

The electrical impedance of the antenna was measured using an impedance analyzer (Agilent E4294A). Figure 5.11 shows the comparison of the frequency response of the fabricated structure and the commercial NFC antenna. The measured inductance of the commercial version was 1.29$\mu$H while our inductor had a very similar value of 1.27$\mu$H when electroplated for 2.5 hours. To decrease the series resistance even further, the sample was electroplated one more time for a total of 3 hours; obtaining an inductance of 1.32$\mu$H. The small discrepancy in the inductance values is likely due to the variation in geometry after the electroplating step; the tracks increased their width by 7.5$\mu$m while the spacing between lines decreased. Moreover the final thickness of our fabricated antenna is 18.5$\mu$m whereas the thickness of the commercial version is 70$\mu$m. By controlling the electroplating time and current it is possible to tune the desired electrical conductivity of

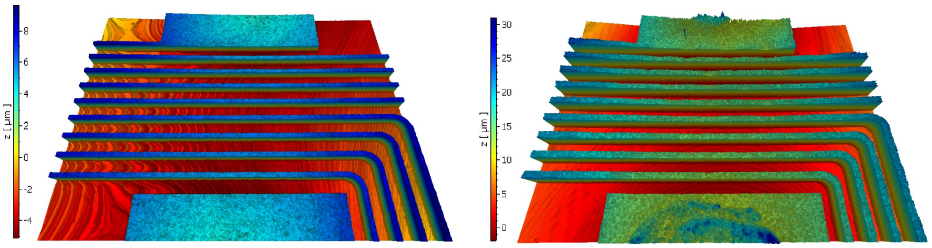

Figure 5.10: **(a)** Topography of replicated NFC antenna design before electroplating. **(b)** Topography after electroplating.

lines, adding flexibility to the fabrication process.

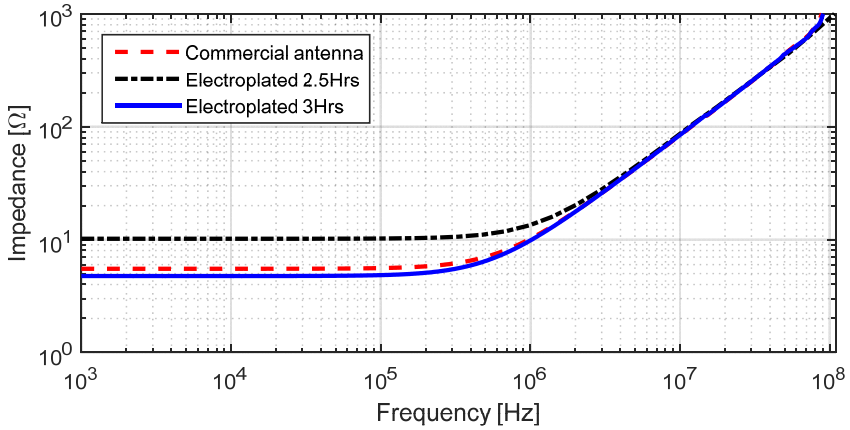


Figure 5.11: Frequency response of fabricated NFC antenna with electroplated copper on top of conductive SU-8.

As an example of miniaturization, a microinductor comparable in size with a commercial chip microinductor [164] was successfully fabricated. It has 5$\mu$m lines with 20$\mu$m spacing in between as shown in Figure 5.12a. The microcoil was fabricated using the same approach as the NFC antenna, except that the electroplating current was 50$\mu$A for 30min due to the size of the structure and the thin traces. The electrical resistance of the microin-

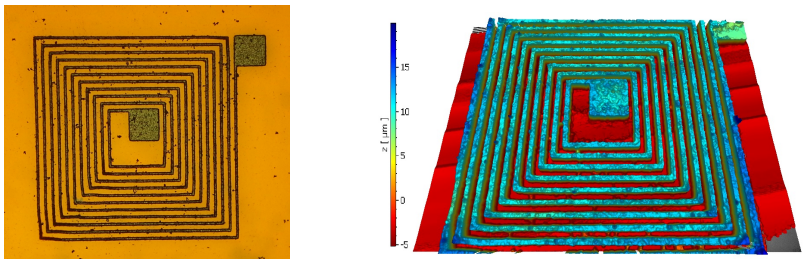

(a) (b)

Figure 5.12: **(a)** Microinductor with 5$\mu$m line width and 20$\mu$m spacing fabricated with condcutive SU-8. **(b)** Topography measurement after electroplating

ductor was measured in a microprobe station, having a value of 17.9Ω.

This minimum limit of 5$\mu$m is related to the adhesion between the flexible substrate and the functionalized SU-8 and not to the exposure equipment which has minimum resolution of 0.6$\mu$m, so even smaller traces are feasible on other substrates or when flexibility requirements are lower. The silver nanoparticles embedded in the SU-8 matrix creates a rough surface on the back side of the patterned traces due to light scattering, decreasing its adhesion to the substrate. It was noticed noticed during our experiments that longer exposure times led to a better adhesion of conductive tracks to the substrate. A potential application of patterning such small conductive lines would be for the fabrication of fractal RF antennas [158], where a geometry is recursively replicated to increase its effective electrical length in a lower area.

### 5.2.3 High-density interconnections

The proposed fabrication process can be used to pattern high-density interconnection lines comparable to those in the flexible PCB industry [157]. Figure 5.13 shows an example of a ball grid array (BGA) fan-out circuit, having 96 electrical connections at the center with a pitch of 300$\mu$m; these dimensions are typical of commercial FPGA or microprocessors. It is worth mentioning that the layer thickness obtained with this conductive SU-8 was designed to be thick enough to fabricate MEMS devices with it, observing a strong correlation between viscosity of SU-8 and achievable minimum linewidths.

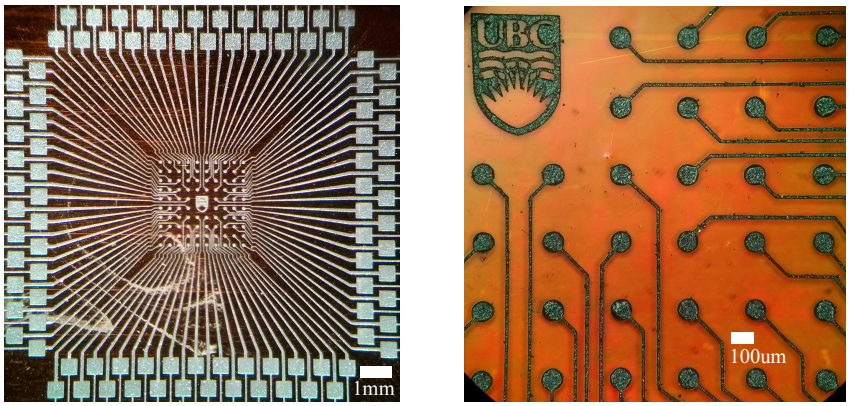


(a) (b)

Figure 5.13: **(a)** BGA fan-out interconnection circuit. **(b)** Detailed view of the center of the array.

The average electrical resistivity between the center connections and the external terminals was 35k$\Omega$; after electroplating the sample for 1.5 hours maintaining a current of 1mA the average resistivity was decreased to 31$\Omega$. Based on the resistivity values, equivalent interconnections fabricated in

gold and platinum would have a resistance 9.4Ω and 40.7Ω respectively; meaning that the resistivity of our electroplated SU-8 structures lies in the same order of magnitude as common metallic materials used for interconnections [165].

### 5.2.4 LC resonant circuit

The performance of a fully electroplated LC resonator circuit as shown in Figure 5.14 was tested. The inductor has 20 turns with 80$\mu$m traces and 80$\mu$m spacing in between. The capacitor has 70 fingers with 50$\mu$m linewidth and 60$\mu$m spacing. After the electroplating process, the spacing between fingers in the capacitor was reduced to 51$\mu$m, increasing the overall capacitance value. The inductance and capacitance values measured independently were 3.15$\mu$H and 3.35pF respectively. Figure 5.15 shows the impedance measurement of the circuit where the resonant and anti-resonant peaks expected of a series LC circuit can be clearly identified; an enlarged section of the high-frequency range is depicted in Figure 5.17.

### 5.2.5 Bending effects

Planar devices on flexible substrates are subjected to repeated bending. When a sheet is bent, the outer surface experiences tensile stress and the inner surface compressive stress, while a plane inside the sheet (called the neutral plane) experiences no stress at all. When films are very thin relative to the substrate the simple approximation below describes the relationship between the effective film strain $\varepsilon_e$ and radius of curvature $r$, where $d$ is the thickness of the substrate [166]

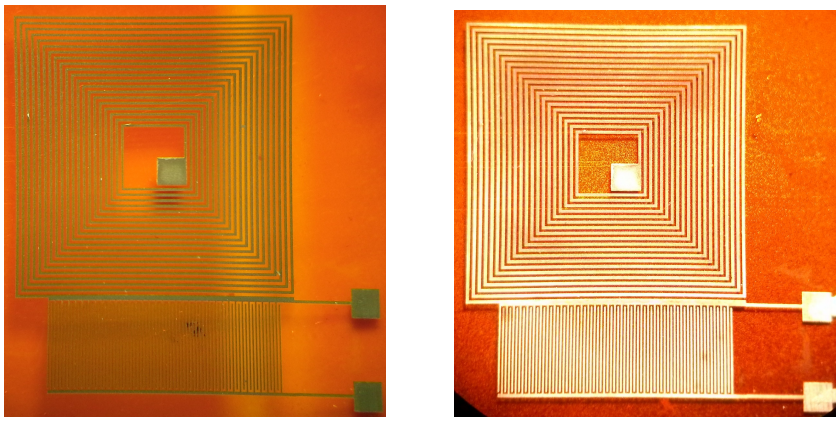

(a) (b)

Figure 5.14: **(a)** Patterned LC circuit before electroplating. **(b)** LC circuit after electroplating, the copper thickness around the conductive SU-8 is 4.5$\mu$m.

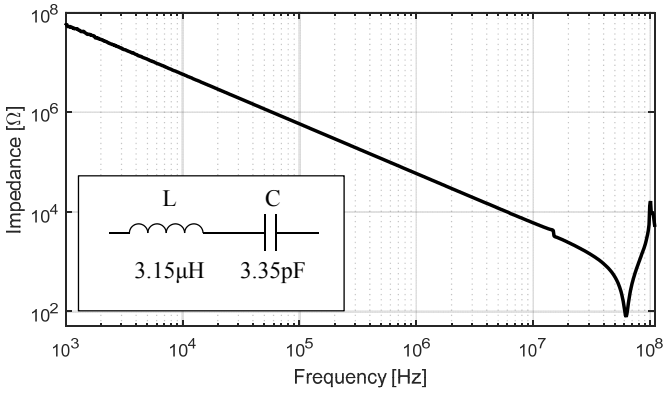


Figure 5.15: Broad frequency response of the fabricated LC circuit with electroplated copper on top of conductive SU-8 with measured values shown in inset.

$$r = \frac{d}{2\varepsilon_e}.$$

In the case of a film deposited on a substrate then $d = d_{film} + d_{substrate}$. When the substrate and the film have different Young's moduli, $(Y)$ and the coated film has a higher value than the substrate, the neutral plane is shifted toward the film reducing the strain by a factor specified in equation (5.1) [167]

$$\epsilon_e = \frac{(d_{film} + d_{ubstrates})(1 + 2\eta + \chi\eta^2)}{2r(1+\eta)(1+\chi\eta)}, \tag{5.1}$$

where $\eta = d_{film}/d_{substrate}$ and $\chi = Y_{film}/Y_{substrate}$. Given the process parameters of our samples, we considered a maximum strain of less than 2% for our calculations based on the results of [118]. A correction factor due to the difference of Young's moduli for 18.5$\mu$m of SU-8 ($Y \sim 4$GPa) on a 137$\mu$m Kapton film ($Y \sim 2.5$GPa) is 0.944 [167]; being 4.5mm the minimum bending radius to avoid fracture of our tracks.

To measure the effects of repetitive bending, we created a similar fixture as in [166] shown in Figure 5.16. The NFC antenna sample presented in section 3.3 was attached between a fixed and a movable plate guided by metal rods to guarantee a parallel displacement; the radius of curvature is controlled by adjusting mechanical stoppers on the testing bench.

The sample was bent at 15, 10, 5 and 4.5mm radii for 1, 10, 100 and 1000 times. The average variation in the inductance stayed below 1% from its initial value. For a bending radius below 3mm, tensile stress caused the conductive tracks to fracture.

As a complimentary experiment, the effects of compressive stress were tested; we bent the LC circuit sample presented in section 5.2.4 at 15, 10 and

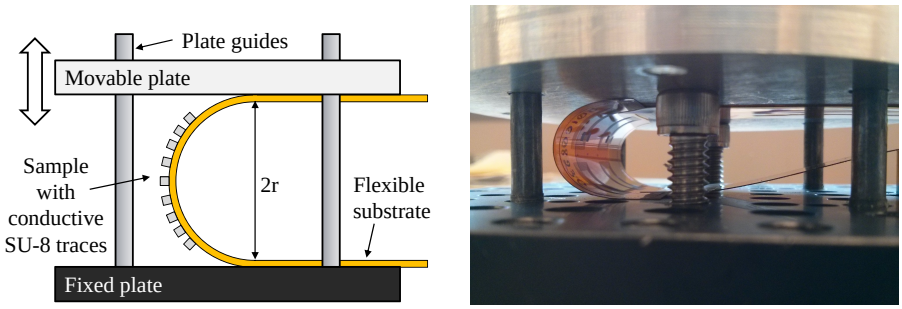


(a) (b)

Figure 5.16: **(a)** Mechanical setup for bending test. **(b)** Bending test of LC circuit when bending radius is 15mm.

5mm radii. Figure 5.17 shows the relative insensitivity of the impedance of the circuit after repeated bending; the variation in capacitance and inductance stayed below 2.5%. After bending the sample 10 cycles at a radius of 5mm, some of the electrical traces started to peel-off the Kapton substrate as shown in Figure 5.18 but the sample was still functional; after 100 cycles several of the traces started to fracture rendering the sample unusable.

The Kapton film used as substrate shrinks by 0.35% when heated to 200°C; this low shrinkage percentage on the substrate produced no delamination nor evident damage on the patterned SU-8 layers even after bending; nevertheless attention is required should substrates with higher shrinkage percentage be used as they might compromise the minimum achievable resolution of patterns, for instance high-density polyethylene (HDPE) and thermoplastic elastometers (TPE) films exhibit shrinkage rates beyond 2.5%.

It is important to mention that the presented fabrication approach is not limited to flexible substrates; some of the example devices shown were also fabricated on rigid substrates (silicon wafers and glass slides).

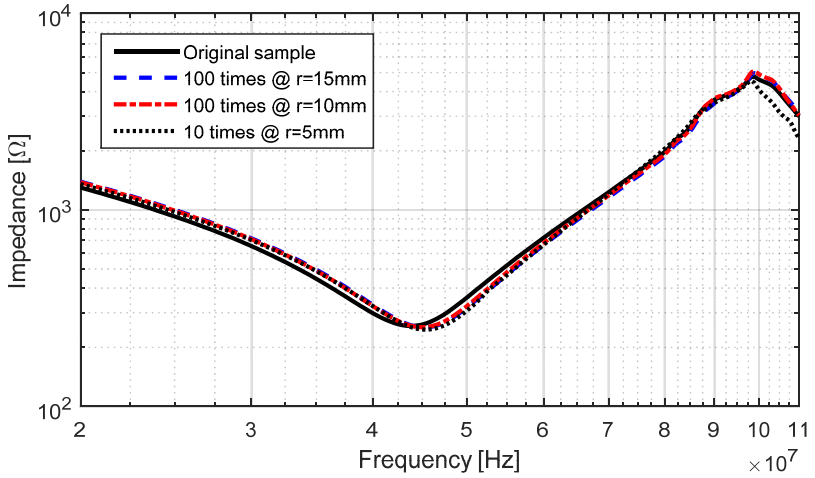


Figure 5.17: Frequency response of the fabricated LC circuit with electroplated copper on top of conductive SU-8 for different bending radii.

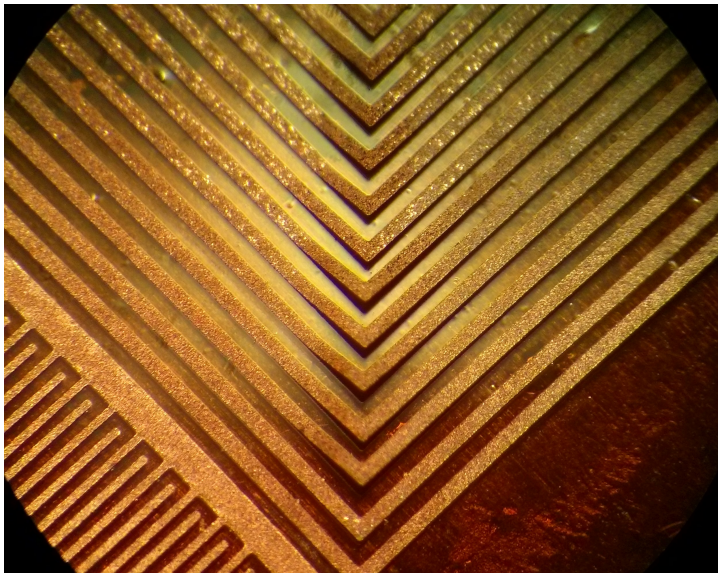

Figure 5.18: Electroplated copper traces peeling off the substrate after 10 bending cycles when r=5mm.

## 5.3 Hybrid integration of conductive SU-8 and CMUTs

For future work, we plan a hybrid integration of planar devices fabricated with functionalized SU-8, off-the-shelf components and die elements mounted on flexible substrates. As preliminary work, we were able to solder a surface-mounted capacitor between two electroplated tracks on functionalized SU-8 as shown in Figure 5.19. Also as future work we plan to include dielectric materials for multi-layer fabrication of interconnection circuits.

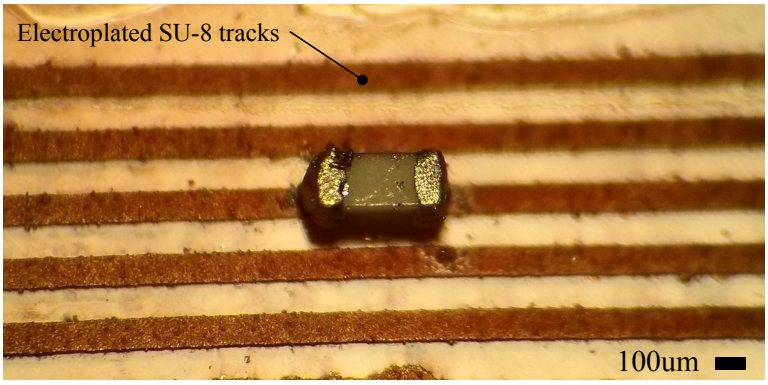


Figure 5.19: Surface-mounted capacitor soldered between electroplated tracks on functionalized SU-8.

### 5.3.1 Optimum energy transfer using embedded passive components

A matching network using the characteristic impedance of a circuit can be used as a way to minimize the electrical losses in ultrasound systems [168]. This is implemented using a matching network of inductors between

capacitive elements (CMUTs or piezoelectric crystals) and the front-end electronics to guarantee the maximum transmission of energy. This idea could potentially be realized by leveraging the fabrication of microinductors using conductive SU-8 introduced in this chapter.

## 5.4 Conclusions and discussions

The successful fabrication of planar passive devices and circuit interconnects on a flexible piece of Kapton using conductive SU-8 with silver nanoparticles embedded at a concentration of wt 25% was presented. This technology uses essentially the same raw material used for the fabrication of polyCMUTs (SU-8). Such components can be the building blocks of more complex sensing schemes such as filters and wireless sensors. To the best of the author's knowledge, this is the first report of functionalized SU-8 used to fabricate such planar devices and the first on flexible substrates. A demonstration of a miniature inductor design was presented, where conductive line traces as small as 5$\mu$m in width were obtained.

It is worth mentioning that all of the fabricated devices presented do not have a protective layer on top and are directly exposed to air. The fabricated devices were robust against bending even at small radii. The minimum bending radius could potentially be further reduced by adding a protective layer such as parylene-C or SU-8; thereby enhancing the adhesion of the conductive traces to the substrate. An extra advantage is that these components can easily be manufactured in the inner layers of flexible substrates, occupying less footprint where space is critical in sensing

applications.

In summary, this chapter highlights the novelty of using conductive SU-8 and electroplating for the fabrication of passive elements and circuit interconnects on flexible substrates. Conductive SU-8 can be used as an alternative to metal deposition when the substrate is sensitive to the environment of metal evaporators and sputtering systems; moreover functionalized SU-8 can be used as electrical connections for elements that do not require a high electrical conductivity such as capacitive devices.

A UV mask aligner was the only required equipment to pattern conductive tracks and so it allowed us to continue with the electroplating step in a conventional laboratory using a simple and inexpensive electroplating system; representing a potential reduction in the fabrication costs. This couples smoothly with the fabrication of ultrasound transducers in Chapter 4, where polyCMUTs were fabricated using inexpensive materials and minimum equipment.

# Chapter 6

# Conclusions and future work

## 6.1 Summary of the thesis

Piezoelectric-based transducers have dominated the ultrasound industry since the 1930s, with Capacitive Micromachined Ultrasonic Transducers (CMUTs) posing to be the replacement for this technology, as they offer higher bandwidth, better integration with electronics, comparable output power and the possibility of fabricating large 2D arrays for 3D imaging. Despite having a few disadvantages such as lower output power and cross-coupling effects, there is a large research community dedicated to improve CMUTs and bring them closer to real commercial devices that can compete with their piezoelectric rivals, with a few commercially available devices already in the market [9, 10].

Currently there exist two main methodologies of fabricating CMUTs, the first one involves surface micromachining, where layers of different structural and sacrificial materials are deposited and selectively patterned and etched using photolithography techniques leveraged from the CMOS industry. The second one is called wafer bonding, in which the cavities and membranes of wafers are created on separate substrates and then bonded together under vacuum and high temperatures. Even though the first version of a CMUT

was created in 1994, the fabrication technology has remained more or less the same. Both of the fabrication methods require specialized equipment in a cleanroom environment with numerous fabrication steps. So a new fabrication method is needed with simpler equipment and fewer fabrication steps.

CMUTs are typically modeled as equivalent circuits capturing the interactions between the electrical, mechanical and acoustical domains. A great number of models still use the basic linear model developed by Mason in 1948 [26]. These linear models present a few disadvantages, given the fact that they use a linear transformer to capture the nonlinear behavior between the electrical and mechanical domains. The summary of the thesis is as below, organized by chapters.

In chapter 2, we presented the development of a large-signal model (macromodel) for CMUTs based on energy-flow theory. This type of model captures the accuracy of analytical model without the simulation constraints faced by FEM models. The macromodel compares favorably against linear models based on Mason's theory widely used by the CMUT research community. We developed two versions of the derived circuit. The first model treats the CMUT as if it were a parallel plate capacitor, leading to a straightforward implementation in SPICE simulators. The second one used mode participation factors theory [97], giving a more accurate representation of the deflected membrane in a CMUT. Because this more complex model uses Bessel functions in its equations, it could not be implemented in standard SPICE simulators and had to be implemented in Matlab-Simulink (Natick, Massachusetts, USA).

Simulation results were compared against FEM simulations and experimental measurements. Our model is capable to accurately predict the behavior of CMUTs in air and water. The small discrepancy between the predicted resonance frequency of our model and the measured experimentally was attributed to the clamping conditions and geometry of the electrodes of the real device. The proposed model is also able to predict the pull-in voltage in an accurate way. We highlighted the difference of our model compared to the widely used Mason-like model [26]; where a linear transformer used led to modeling inaccuracies at voltages close to pull-in.

The same energy-flow theory was applied to develop a macromodel for a special kind of CMUTs called asymmetric CMUTs and was presented in chapter 3. These devices have two top electrodes and a shared bottom electrode. This allows the deliberate excitation of non-axisymetric vibration modes. Some of the applications of these asymmetric CMUTs are in super resolution algorithms [20] and physical beam focusing and steering [89]. Mode participation vibration theory [97] was used to analyze the interactions between vibration modes of a CMUT membrane. The simulation results are in good agreement with FEM simulations and experimental results.

Chapter 4 described the development of a new polymer-based CMUT termed *polyCMUT*. The main challenge was to create a fabrication recipe aiming to produce low-cost CMUTs using the fewest number of fabrication steps and equipment and yet obtaining a device comparable in performance with existing CMUTs designs.

The selection of structural and sacrificial materials was critical and re-

quired numerous and time-consuming experiments and extensive literature review. The photopolymer SU-8 was selected as structural material given its dielectric and thermal properties, as well as its low density, photopatternability, optical transparency and mechanical flexibility. After finding a potential sacrificial material (Omnicoat) totally compatible with the fabrication steps using SU-8 as structural materials, the first generation of polyCMUTs was created. After the first prototype was sealed in parylene-C and successfully operated in oil we concluded the first proof-of-concept that polymers can be used to fabricate CMUTs that can operate in liquid medium.

Despite this milestone, a major problem was still remaining. We used a thick SU-8 membrane with a metal electrode on top to reach the MHz region for ultrasound imaging. This first design had a very large effective gap between electrodes, requiring hundreds of volts for actuation. We solved this problem by adding an extra fabrication step; allowing us to embed the top electrode in the membrane and to decrease the effective gap between electrodes; therefore, achieving low actuation voltages (below 50V).

The selected materials allowed us to fabricate fully functional prototypes in less than 24 hours with material costs below $100 USD. After five generations of polyCMUTs we successfully fabricated a 64 element linear array. This array was later mounted on an interface PCB and obtained the first B-mode image in the world created with this technology and synthetic aperture beamforming techniques.

An advantageous effect of embedding the top electrode inside the membrane was to have what we called a “pre-bias” condition, in which the

membrane behaves as if it had an intrinsic (built-in) DC bias pulling the membrane towards the bottom electrode. This effect allowed us to directly detect ultrasound waves without the need of external power, i.e. using the polyCMUT as passive device during reception. We attribute this effect to electrical charges trapped in the interface between the SU-8 membrane as the metal electrode as proposed in [123]. After experimentation we observed that the polyCMUT can be "charged" and "discharged" by connecting it to a high voltage. More experimentation is needed to fully understand the physics behind this effect.

It is important to mention that the materials and solvents used during manufacturing have low toxicity, and the sealing layer covering the device is considered to be biocompatible. The maximum process temperature used was 150°C, meaning that polymer-based CMUTs can be potentially fabricated directly on top of substrates containing pre-existing components.

This work presented in chapter 4 highlights the benefits of using a simple fabrication process with inexpensive materials coupled to basic microfabrication equipment. Although SU-8 photopolymer was used for this study, any other polymer or soft material can in principle be used for the fabrication of polyCMUTs. The important factor is to maintain a small effective gap between the electrodes of polyCMUTs for low operational voltages and high sensitivity.

Chapter 5 describes the fist steps in the attempt of interconnecting passive components and CMUTs on flexible substrates. The main motivation for this chapter is to fabricate interconnection lines and passive devices using similar polymer-based materials; aiming to reduce parasitics in the

integrated system.

A potential and direct application of this integration would be a matching network consisting of an array of inductors that counter-react the capacitive effects from CMUTs; this would provide a maximum energy transfer between polyCMUTs and electronics, increasing the SNR.

Composite materials exhibit properties that cannot be found with metals, polymers or ceramics alone. In particular metallic nanoparticles embedded in polymers maintain the electrical properties in the metallic range while maintaining the flexibility and some unique properties of polymers such as bio-compatibility, chemical resistivity, optical transparency, photosensitivity, etc. In this chapter, we attempt to use this kind of material to fabricate inductors and capacitors as a proof of concept that they can be potentially fabricated at the same time as polyCMUTs.

SU-8 was selected for its mechanical and photo patterning properties. In the attempt of creating a conducive polymer, we tested different conducive nanoparticles in combination with SU-8. We tested carbon black nanoparticles, the conductive organic chemical PEDOT:PSS (poly(3,4-ethylenedioxythiophene) polystyrene sulfonate), carbon nanotubes and silver nanoparticles. After numerous experiments, we selected silver nanoparticles for its conductivity properties and the homogeneous dispersion in SU-8.

The limit in which the concentration of conductive fillers in a polymer starts being electrically conductive is known as percolation threshold; for the case of silver nanoparticles and SU-8, this limit is around 20% of the weight. Maintaining a homogeneous silver-SU-8 mixture had its own challenges, as the silver tends to sediment at the bottom when still. If the mixture is

agitated too slow, it creates silver agglomerations, but if it is agitated too fast, it traps air bubbles that create problems during lithography. We solved this issue using a high speed agitator in the beginning to break any possible silver lumps, we then de-gas the mixture in an ultrasound bath, finally we maintain the mixture in constant agitation using a magnetic stirrer; slow enough to avoid the air bubbles but high enough to prevent sedimentation.

The mixture of conductive SU-8 was patterned using ordinary photolithography techniques in a cleanroom. Because the silver fillers tend to adsorb UV light around 300nm in wavelength, a higher UV light dose was required to photopolymerize the mixture and create conductive patterns in a single fabrication step. We used kapton films as the flexible substrates because of its chemical and thermal properties. We successfully patterned conductive lines to create resistive paths and planar capacitors on flexible substrates. Because inductors need low impedance traces, we used an electroplating stage to boost the conductivity of the patterned structures. Because of this, we were able to fabricate a resonant LC circuit that was still operational after repetitively bending it several hundreds of times at small radii. The demonstration of high-density interconnection lines in a ball-grid-array (BGA) fan-out design and the fabrication of a microinductor with 5$\mu$m conductive lines was also presented.

It is important to mention that the presented devices are directly exposed to air, and that an extra encapsulation step might increase the bending properties of these passive devices with the possibility of having multilayer structure. More work needs to be done to fully couple polyCMUTs with this technology, but the proof of concept that polymer-metals mixture

can be used to fabricate inductors on flexible substrates is completed.

## 6.2 Contributions to the state of knowledge

In this thesis document we presented the development of an accurate large-signal model for symmetric and asymmetric CMUTs based on energy-flow theory. This macromodel is capable to capture the non-linearities associated with CMUTs such as spring-softening and pull-in.

We successfully designed, simulated, fabricated and characterized CMUTs built using polymer materials. The fabricated polyCMUTs used inexpensive materials, a simple fabrication process, and were created in less than 24 hours; obtaining performances comparable with traditional CMUTs created with polysilicon or silicon nitride. The developed devices allowed us to obtain the first B-mode image in the world using a linear array of 64 poly-CMUT elements, with material costs well below $100 USD (compared to ∼$4000 USD using a commercial piezoelectric-based probe). The potentials of this achievement will be discussed more in detail in the next section.

Lastly, we explored the possibility of fabricating passive devices using a conductive polymers created using silver nanoparticles and the photopolymer SU-8. We successfully patterned high-density interconnection lines, planar resistors, capacitors and even inductors when coupled to an electroplating stage. Low-pass filters and resonators were created on flexible substrates that successfully withstood numerous bending cycles under small bending radii. This technology can be potentially integrated with poly-CMUT technology to reduce the SNR during readout.

## 6.3 Future directions

The advantages offered by polyCMUTs open many possible future directions. There are still a few unanswered questions that need to be addressed to fully exploit its potentials. The real acoustic pressure generated by polyCMUTs needs to be measured using a calibrated hydrophone in a water tank and compared to the acoustic pressure from commercial piezoelectric-based ultrasound probes and perhaps to traditional CMUT arrays fabricated using polysilicon or silicon nitride. This calibrated hydrophone could also be used to test the sensitivity of our devices during reception and compare it against other types of transducers. The possible thermal energy generated by the resistive chromium-based top electrodes needs to be investigated as well. Chromium has a lower conductivity than aluminum or gold and might lead to electrical power dissipated as heat. A first guess is that the liquid medium on the membranes during real operation will be able to quickly dissipate the potential generated heat, but this could be confirmed by using perhaps a thermal camera.

### 6.3.1 Fabrication of polyCMUTs on flexible substrates

Motivated by the results presented in chapter 4, we are planning to continue investigating other alternatives for fabrication of CMUTs using flexible substrates. This has been a recent hot topic for major players in the ultrasound industry [68, 169]. They have manifested their interest in creating a conformal ultrasound imaging system that can adopt the curved shapes of some body parts such as the abdomen, neck, arms, etc.

Rigid transducers are robust and work perfect for ordinary applications such as obstetrics. Flexible (conformal) ultrasound imaging systems might be beneficial for applications where large transducers cannot easily access, for instance in intravascular imaging (IVUS). Conformal transducers can also work if the target application are large transducers that physically focus the beams by surrounding a curved area.

Figure 6.1 depicts the artist's impression of a desired prototype in the future. We are planning to fabricate a polyCMUT array small enough to fit on a flexible patch that can be powered using a coin battery. The sensed signals will be then transmitted wirelessly to a smartphone or a smartwatch or being processed in the cloud directly.

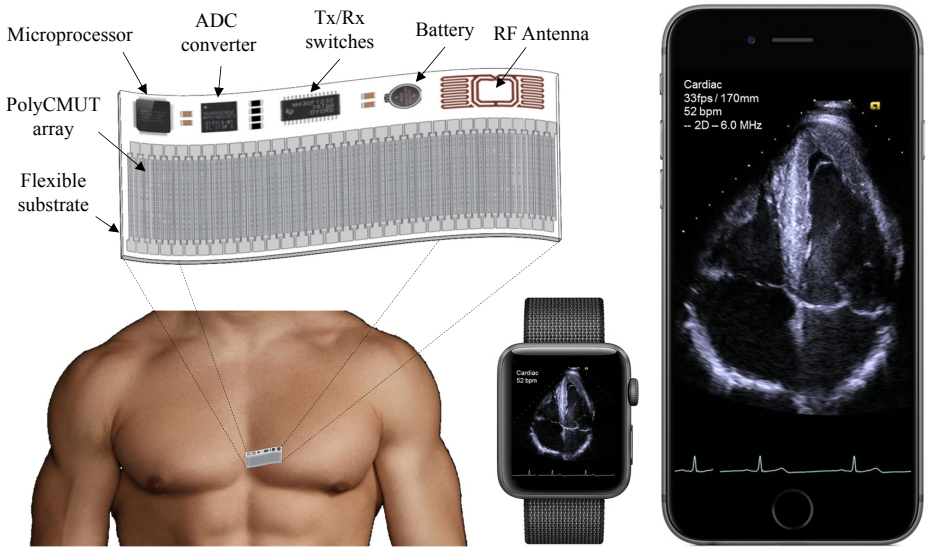


Figure 6.1: Futuristic vision of polyCMUT-based portable and flexible ultrasound system for continuous cardiac monitoring.

We can also leverage from the benefits of the selected materials for the

fabrication of polyCMUTs. Given the fact that both SU-8 and parylene-C are considered biocompatible, we envision the development of a stand-alone ultrasound imaging system that can be implanted inside the body. This might have direct applications in the mobile health care industry, where patients often need continuous monitoring of vital signs.

The main challenge for its development is to find a reliable way to create electrical interconnections to and from the CMUT elements in these kind of arrays. It has been previously reported that CMUTs can be fabricated on flexible substrates [131, 132], nevertheless they face reliability issues during bending as the electrical interconnections between CMUT cells cannot withstand the great strain and forces of the bending moments, leading to degradation of signals and in some cases cracking of lines.

A small patch-like portable ultrasound imaging system can be developed using these inexpensive materials. In fact, we believe we can reduce the fabrication costs even further to the point in which the transducers can be considered disposable.

### 6.3.2 Large-area ultrasound systems

The fabrication technology for polyCMUTs is not restricted to small-size samples, it can be scalable in size and is only limited by the fabrication equipment. We consider the possibility of fabricating polyCMUTs on large-size flexible substrates with the aim of wrapping large and curved body surfaces with it. For example, a large-area polyCMUT array can be built for the detection and monitoring of breast cancer.

We expect that the engineering design of CMUTs on bendable materi-

als to be non-trivial. We speculate that the material and even acoustical properties of the back substrate will play an important role in the final performance of polyCMUTs; as well as the compressive or tensile stresses that arise from bending the polyCMUTs inwards or outwards. It might be necessary to look at other non-peculiar design aspects using an analogy similar to [170].

### 6.3.3 High-frequency polyCMUTs

As mentioned in section 1.3, high frequency ultrasound gives us high axial resolution and is useful to define fine features in the human body such as in the eye or in the skin. The fabrication of piezoelectric-based ultrasonic arrays operating above 20MHz is very challenging [11], this is mostly due to limitations in the spacial scale, materials and fabrication methods. Conventional piezoelectric arrays typically use a "dice-and-fill" approach, where a plate of piezoelectric material us mechanically diced and a polymer is cured within the kerfs. This contrasts with the wide range of operating frequencies of CMUTs, some of them reportedly reaching 60MHz [12]. Nevertheless, the higher the operational frequency in CMUTs, the thicker the membrane, and therefore the larger the operational voltage need to be.

In the case of polyCMUTS, the thickness of the second SU-8 layer is tailored to the desired operational frequency of the device. Since the effective gap between the top and bottom electrodes (and therefore the operational voltage) is dictated by the cavity height and thickness of the first SU-8 layer, this design allows the fabrication of low-frequency and high-frequency CMUTs with constant operational voltages. Figure 6.2 shows a compari-

son in the geometry of CMUTs and polyCMUTs for different operational frequencies maintaining a constant diameter.

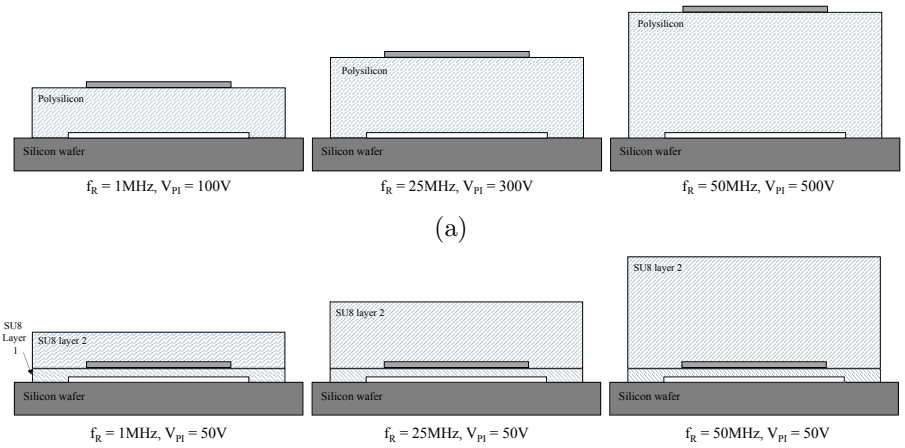


Figure 6.2: Cross sectional view of CMUTs and polyCMUTs for different frequency range. (a) The effective gap CMUTs increases as the membrane get thicker for high-frequency operations, (b) The effective gap in poly-CMUTs remains the same regarding the operational frequency thanks to their embedded electrodes.

### 6.3.4 Charge trapping control of CMUTs

The fabrication of polyCMUTs includes a metal electrode embedded in the CMUT membrane for low-voltage actuation. This unique structure allows electrical charges to be trapped and stored, creating an intrinsic (built-in) voltage. A future work involves exploiting this effect to fabricate polyCMUTs that do not require DC bias to operate, therefore drastically reducing the energy consumption and potentially be used as passive devices during reception.

### 6.3.5 Hybrid integration with electronics

It is known that a way to minimize the electrical losses in ultrasound systems is to counter-react the parasitics capacitances though a matching network using the characteristic impedance of the circuit [168]. The technology described in chapter 5 might be used to fabricate and connect a matching network of inductors between capacitive elements (CMUTs of piezoelectric crystals) and the front-end electronics to guarantee the maximum transmission of energy. This hybrid integration would provide a polyCMUT-based ultrasound transducers the benefits to be fabricated directly on flexible substrates without affecting the electrical parasitic burden imposed by external off-the-shelf components such as beamformers and amplifiers.

A breakthrough in CMUT-based ultrasound systems would be a combination between highly-sensitive low-cost transducers and the integration of polymer-based electronics on flexible substrates for conformal ultrasound imaging applications.

# Bibliography


[1] E. Cretu, *Inertial MEMS Devices: Modeling, design and applications.* PhD thesis, 2003.

[2] O. Oralkan, A. S. Ergun, J. A. Johnson, M. Karaman, U. Demirci, K. Kaviani, T. H. Lee, and B. T. Khuri-Yakub, "Capacitive micromachined ultrasonic transducers: Next-generation arrays for acoustic imaging?," *Ultrasonics, Ferroelectrics and Frequency Control, IEEE Transactions on*, vol. 49, no. 11, pp. 1596–1610, 2002.

[3] R. O. Guldiken, *Dual-electrode capacitive micromachined ultrasonic transducers for medical ultrasound applications.* PhD thesis, 2008.

[4] I. Trots, A. Nowicki, M. Lewandowski, W. Secomski, and J. Litniewski, "The influence of the transducer bandwidth and double pulse transmission on the encoded imaging ultrasound," *Hydroacoustics*, vol. Vol. 11, pp. 419–430, 2008.

[5] G. G. Yaralioglu, A. S. Ergun, B. Bayram, E. Haeggstrom, and B. T. Khuri-Yakub, "Calculation and measurement of electromechanical coupling coefficient of capacitive micromachined ultrasonic transducers," *Ultrasonics, Ferroelectrics and Frequency Control, IEEE Transactions on*, vol. 50, no. 4, pp. 449–456, 2003.

[6] J. A. Gallego-Juarez, "Piezoelectric ceramics and ultrasonic transducers," *J. Phys. E: Sci. Instrum.*, vol. 22, no. 10, p. 804, 1989.

[7] Q. Zhou, K. H. Lam, H. Zheng, W. Qiu, and K. K. Shung, "Piezoelectric single crystals for ultrasonic transducers in biomedical applications," *Prog Mater Sci*, vol. 66, pp. 87–111, Oct. 2014.

[8] J. Cho, M. Anderson, R. Richards, D. Bahr, and C. Richards, "Optimization of electromechanical coupling for a thin-film PZT membrane: I. Modeling," *J. Micromech. Microeng.*, vol. 15, no. 10, p. 1797, 2005.

[9] D. Zhao, S. Zhuang, and R. Daigle, "A commercialized high frequency CMUT probe for medical ultrasound imaging," in *2015 IEEE International Ultrasonics Symposium (IUS)*, pp. 1–4, Oct. 2015.

[10] "Butterfly iQ imaging system." `https://www.butterflynetwork.com/`. Accessed: 2018-07-10.

[11] T. A. Ritter, T. R. Shrout, R. Tutwiler, and K. K. Shung, "A 30-MHz piezo-composite ultrasound array for medical imaging applications," *IEEE Transactions on Ultrasonics, Ferroelectrics, and Frequency Control*, vol. 49, pp. 217–230, Feb. 2002.

[12] O. Oralkan, S. T. Hansen, B. Bayram, G. G. Yaralioglu, A. S. Ergun, and B. T. Khuri-Yakub, "High-frequency CMUT arrays for high-resolution medical imaging," in *IEEE Ultrasonics Symposium, 2004*, vol. 1, pp. 399–402 Vol.1, Aug. 2004.

[13] S. Timoshenko, S. Woinowsky-Krieger, and S. Woinowsky-Krieger, *Theory of plates and shells*, vol. 2. McGraw-hill New York, 1959.

[14] W. Soedel, *Vibrations of shells and plates*. CRC Press, 2004.

[15] I. O. Wygant, M. Kupnik, and B. T. Khuri-Yakub, "Analytically calculating membrane displacement and the equivalent circuit model of a circular CMUT cell," in *2008 IEEE International Ultrasonics Symposium*, pp. 2111–2114, IEEE, Nov. 2008.

[16] N. Hall, R. Guldiken, J. McLean, and F. Degertekin, "Modeling and design of CMUTs using higher order vibration modes [capacitive micromachined ultrasonic transducers]," in *2004 IEEE Ultrasonics Symposium*, vol. 1, pp. 260–263 Vol.1, Aug. 2004.

[17] M. N. Senlik, S. Olcum, H. Koymen, and A. Atalar, "Radiation impedance of an array of circular capacitive micromachined ultrasonic transducers," *Ultrasonics, Ferroelectrics and Frequency Control, IEEE Transactions on*, vol. 57, no. 4, pp. 969–976, 2010.

[18] R. O. Guldiken, J. McLean, and F. L. Degertekin, "CMUTS with dual electrode structure for improved transmit and receive performance," *Ultrasonics, Ferroelectrics and Frequency Control, IEEE Transactions on*, vol. 53, no. 2, pp. 483–491, 2006.

[19] F. J. Fahy and P. Gardonio, *Sound and structural vibration: radiation, transmission and response*. Academic press, 2007.

[20] W. You, E. Cretu, and R. Rohling, "Super-Resolution Imaging Using Multi-Electrode CMUTs: Theoretical Design and Simulation Using Point Targets," *IEEE Transactions on Ultrasonics Ferroelectrics and Frequency Control*, vol. 60, no. 11, pp. 2295–2309, 2013.

[21] W. You, E. Cretu, and R. Rohling, "Direction of Arrival Estimation Using Asymmetric Mode Components of CMUTs," in *2012 IEEE International Ultrasonics Symposium*, 2012. WOS:000326960201135.

[22] B. Ahmad and R. Pratap, "Elasto-electrostatic analysis of circular microplates used in capacitive micromachined ultrasonic transducers," *Sensors Journal, IEEE*, vol. 10, no. 11, pp. 1767–1773, 2010.

[23] S. J. Ballandras, M. Wilm, and J.-F. Gelly, "Theoretical analysis of micro-machined ultrasonic transducer using a simple 1-D model," *Ultrasonics, Ferroelectrics and Frequency Control, IEEE Transactions on*, vol. 53, no. 1, pp. 209–223, 2006.

[24] W. You, E. Cretu, and R. Rohling, "Analytical Modeling of CMUTs in Coupled Electro-Mechano-Acoustic Domains Using Plate Vibration Theory," *IEEE Sensors Journal*, vol. 11, pp. 2159–2168, Sept. 2011.

[25] S. D. Senturia, *Microsystem design*, vol. 3. Kluwer academic publishers Boston, 2001.

[26] W. P. Mason, *Electromechanical transducers and wave filters*. D. Van Nostrand Co., 1948.

[27] M. I. Haller and B. T. Khuri-Yakub, "A surface micromachined electrostatic ultrasonic air transducer," *Ultrasonics, Ferroelectrics and Frequency Control, IEEE Transactions on*, vol. 43, no. 1, pp. 1–6, 1996.

[28] A. Lohfink and P.-C. Eccardt, "Linear and nonlinear equivalent circuit modeling of CMUTs," *Ultrasonics, Ferroelectrics and Frequency Control, IEEE Transactions on*, vol. 52, no. 12, pp. 2163–2172, 2005.

[29] H. Oguz, S. Olcum, M. N. Senlik, V. Tas, A. Atalar, and H. Koymen, "Nonlinear modeling of an immersed transmitting capacitive micromachined ultrasonic transducer for harmonic balance analysis," *Ultrasonics, Ferroelectrics and Frequency Control, IEEE Transactions on*, vol. 57, no. 2, pp. 438–447, 2010.

[30] E. Aydogdu, A. Ozgurluk, A. Atalar, and H. Koymen, "Lumped element modeling of CMUT arrays in collapsed mode," in *Ultrasonics Symposium (IUS), 2014 IEEE International*, pp. 309–312, Sept. 2014.

[31] C. Meynier, F. Teston, and D. Certon, "A multiscale model for array of capacitive micromachined ultrasonic transducers," *The Journal of the Acoustical Society of America*, vol. 128, pp. 2549–2561, 2010.

[32] H. K. Oguz, A. Atalar, and H. Koymen, "Analysis of mutual acoustic coupling in CMUT arrays using an accurate lumped element nonlinear equivalent circuit model," in *Ultrasonics Symposium (IUS), 2012 IEEE International*, pp. 983–986, IEEE, 2012.

[33] M. Engholm and E. V. Thomsen, "Modeling of CMUTs with multiple anisotropic layers and residual stress," in *Ultrasonics Symposium (IUS), 2014 IEEE International*, pp. 2603–2606, Sept. 2014.

[34] S. Satir, J. Zahorian, and F. L. Degertekin, "Large-Signal Model for CMUT Arrays with Arbitrary Membrane Geometry Operating in Non-Collapsed Mode," *IEEE Transactions on Ultrasonics Ferroelectrics and Frequency Control*, vol. 60, no. 11, pp. 2426–2439, 2013.

[35] H. Koymen, A. Atalar, E. Aydogdu, C. Kocabas, H. K. Oguz, S. Olcum, A. Ozgurluk, and A. Unlugedik, "An improved lumped element nonlinear circuit model for a circular CMUT cell," *Ultrasonics, Ferroelectrics and Frequency Control, IEEE Transactions on*, vol. 59, no. 8, pp. 1791–1799, 2012.

[36] H. Kagan Oguz, S. Olcum, M. N. Senlik, A. Atalar, and H. Koymen, "A novel equivalent circuit model for CMUTs," in *Ultrasonics Symposium (IUS), 2009 IEEE International*, pp. 2193–2196, IEEE, 2009.

[37] A. Ronnekleiv, "Fast and accurate CMUT modeling using equivalent circuits with lumped parameters," in *2008 IEEE International Ultrasonics Symposium*, pp. 496–499, IEEE, Nov. 2008.

[38] S. Frew, H. Najar, and E. Cretu, "VHDL-AMS behavioural modelling of a CMUT element," in *Behavioral Modeling and Simulation Workshop, 2009. BMAS 2009. IEEE*, pp. 19–24, IEEE, 2009.

[39] G. G. Yaralioglu, S. A. Ergun, and B. T. Khuri-Yakub, "Finite-element analysis of capacitive micromachined ultrasonic transducers,"

*Ultrasonics, Ferroelectrics and Frequency Control, IEEE Transactions on*, vol. 52, no. 12, pp. 2185–2198, 2005.

[40] B. Bayram, G. G. Yaralioglu, M. Kupnik, A. S. Ergun, O. Oralkan, A. Nikoozadeh, and B. T. Khuri-Yakub, "Dynamic analysis of capacitive micromachined ultrasonic transducers," *Ultrasonics, Ferroelectrics and Frequency Control, IEEE Transactions on*, vol. 52, no. 12, pp. 2270–2275, 2005.

[41] M. Rafiq and C. Wykes, "The performance of capacitive ultrasonic transducers using v-grooved backplates," *Meas. Sci. Technol.*, vol. 2, p. 168, Feb. 1991.

[42] K. Suzuki, K. Higuchi, and H. Tanigawa, "A silicon electrostatic ultrasonic transducer," *Ultrasonics, Ferroelectrics and Frequency Control, IEEE Transactions on*, vol. 36, no. 6, pp. 620–627, 1989.

[43] D. Schindel, D. Hutchins, L. Zou, and M. Sayer, "The design and characterization of micromachined air-coupled capacitance transducers," *IEEE Transactions on Ultrasonics, Ferroelectrics, and Frequency Control*, vol. 42, pp. 42–50, Jan. 1995.

[44] A. S. Ergun, X. Zhuang, Y. Huang, O. Oralkan, G. G. Yaralioglu, and B. T. Khuri-Yakub, "Capacitive micromachined ultrasonic transducer technology for medical ultrasound imaging," in *Medical Imaging*, pp. 58–68, International Society for Optics and Photonics, 2005.

[45] D. F. Lemmerhirt, X. Cheng, R. D. White, C. A. Rich, M. Zhang, J. Fowlkes, and O. D. Kripfgans, "A 32 x 32 capacitive micromachined ultrasonic transducer array manufactured in standard CMOS," *Ultrasonics, Ferroelectrics and Frequency Control, IEEE Transactions on*, vol. 59, no. 7, pp. 1521–1536, 2012.

[46] Y. Huang, A. Ergun, E. Haggstrom, M. Badi, and B. Khuri-Yakub, "Fabricating capacitive micromachined ultrasonic transducers with wafer-bonding technology," *Journal of Microelectromechanical Systems*, vol. 12, pp. 128–137, Apr. 2003.

[47] A. S. Erguri, Y. Huang, X. Zhuang, O. Oralkan, G. G. Yarahoglu, and B. T. Khuri-Yakub, "Capacitive micromachined ultrasonic transducers: fabrication technology," *Ultrasonics, Ferroelectrics and Frequency Control, IEEE Transactions on*, vol. 52, no. 12, pp. 2242–2258, 2005.

[48] A. S. Ergun, G. G. Yaralioglu, and B. T. Khuri-Yakub, "Capacitive micromachined ultrasonic transducers: Theory and technology," *Journal of Aerospace Engineering*, vol. 16, no. 2, pp. 76–84, 2003.

[49] R. O. Guldiken, M. Balantekin, and F. L. Degertekin, "Analysis and design of dual-electrode CMUTs," in *Ultrasonics Symposium, 2005 IEEE*, vol. 1, pp. 581–584, IEEE, 2005.

[50] K. K. Park, M. Kupnik, H. J. Lee, B. T. Khuri-Yakub, and I. O. Wygant, "Modeling and measuring the effects of mutual impedance on multi-cell CMUT configurations," *Ultrasonics Symposium (IUS), 2010 IEEE*, pp. 431–434, 2010.

[51] C.-H. Cheng, A. Ergun, and B. Khuri-Yakub, "Electrical through-wafer interconnects with sub-picofarad parasitic capacitance [MEMS packaging]," in *Microelectromechanical Systems Conference, 2001*, pp. 18–21, 2001.

[52] S. Calmes, C. H. Cheng, F. L. Degertekin, X. C. Jin, S. Ergun, and B. T. Khuri-Yakub, "Highly integrated 2-D capacitive micromachined ultrasonic transducers," in *Ultrasonics Symposium, 1999. Proceedings. 1999 IEEE*, vol. 2, pp. 1163–1166, IEEE, 1999.

[53] C.-H. Cheng, C. Chao, X. Shi, and W. Leung, "A flexible capacitive micromachined ultrasonic transducer (CMUT) array with increased effective capacitance from concave bottom electrodes for ultrasonic imaging applications," in *Ultrasonics Symposium (IUS), 2009 IEEE International*, pp. 996–999, IEEE, 2009.

[54] P.-F. Chong, X. Shi, and C.-H. Cheng, "A novel flexible capacitive micromachined ultrasonic transducer (CMUT) array with isolated metallic islands riveted to a polymer film," in *Nano/Micro Engineered and Molecular Systems (NEMS), 2013 8th IEEE International Conference on*, pp. 923–926, IEEE, 2013.

[55] M. Ming-Wei Chang, M.-M. Deng, J.-J. Gwo, J. D. Mai, and E. Hsu, "Polymer-based Capacitive Micromachined Ultrasonic Transducers (CMUT) for Micro Surgical Imaging Applications," in *Nano/Micro Engineered and Molecular Systems, 2006. NEMS'06. 1st IEEE International Conference on*, pp. 61–65, IEEE, 2006.

[56] D. A. Hutchins, D. R. Billson, R. J. Bradley, and K. S. Ho, "Structural health monitoring using polymer-based capacitive micromachined ultrasonic transducers (CMUTs)," *Ultrasonics*, vol. 51, no. 8, pp. 870–877, 2011.

[57] C. F. Dalziel, "Electric shock hazard," *IEEE Spectrum*, vol. 9, pp. 41–50, Feb. 1972.

[58] O. Oralkan, A. S. Ergun, C.-H. Cheng, J. A. Johnson, M. Karaman, T. H. Lee, and B. T. Khuri-Yakub, "Volumetric ultrasound imaging using 2-D CMUT arrays," *Ultrasonics, Ferroelectrics and Frequency Control, IEEE Transactions on*, vol. 50, no. 11, pp. 1581–1594, 2003.

[59] I. O. Wygant, X. Zhuang, D. T. Yeh, O. Oralkan, A. S. Ergun, M. Karaman, and B. T. Khuri-Yakub, "Integration of 2d CMUT arrays with front-end electronics for volumetric ultrasound imaging," *Ultrasonics, Ferroelectrics and Frequency Control, IEEE Transactions on*, vol. 55, no. 2, pp. 327–342, 2008.

[60] A. Nikoozadeh, O. Oralkan, M. Gencel, J. W. Choe, D. N. Stephens, A. de la Rama, P. Chen, F. Lin, A. Dentinger, and D. Wildes, "Forward-looking intracardiac imaging catheters using fully integrated CMUT arrays," in *Ultrasonics Symposium (IUS), 2010 IEEE*, pp. 770–773, IEEE, 2010.

[61] D. T. Yeh, O. Oralkan, I. O. Wygant, M. O'Donnell, and B. T. Khuri-Yakub, "3-D ultrasound imaging using a forward-looking CMUT ring array for intravascular/intracardiac applications," *Ultrasonics, Ferroelectrics and Frequency Control, IEEE Transactions on*, vol. 53, no. 6, pp. 1202–1211, 2006.

[62] S. H. Wong, M. Kupnik, K. Butts-Pauly, and B. T. Khuri-Yakub, "Advantages of Capacitive Micromachined Ultrasonics Transducers (CMUTs) for High Intensity Focused Ultrasound (HIFU)," in *Ultrasonics Symposium, 2007. IEEE*, pp. 1313–1316, IEEE, 2007.

[63] S. H. Wong, M. Kupnik, R. D. Watkins, K. Butts-Pauly, and B. T. Khuri-Yakub, "Capacitive micromachined ultrasonic transducers for therapeutic ultrasound applications," *Biomedical Engineering, IEEE Transactions on*, vol. 57, no. 1, pp. 114–123, 2010.

[64] K. K. Park, H. Lee, M. Kupnik, m. Oralkan, J.-P. Ramseyer, H. P. Lang, M. Hegner, C. Gerber, and B. T. Khuri-Yakub, "Capacitive

micromachined ultrasonic transducer (CMUT) as a chemical sensor for DMMP detection," *Sensors and Actuators B: Chemical*, vol. 160, no. 1, pp. 1120–1127, 2011.

[65] M. Thranhardt, P.-C. Eccardt, H. Mooshofer, P. Hauptmann, and L. Degertekin, "A resonant CMUT sensor for fluid applications," in *Sensors, 2009 IEEE*, pp. 878–883, IEEE, 2009.

[66] X. Wang, Y. Fan, W.-C. Tian, H.-J. Kwon, S. Kennerly, G. Claydon, and A. May, "An Air-Coupled Capacitive Micromachined Ultrasound Transducer for Noncontact Nondestructive Evaluation," in *Sensors, 2007 IEEE*, pp. 1464–1467, IEEE, 2007.

[67] N. Apte, K. K. Park, A. Nikoozadeh, and B. T. Khuri-Yakub, "Bandwidth and Sensitivity Optimization in CMUTs for Airborne Applications," in *2014 IEEE International Ultrasonics Symposium*, 2014.

[68] C. M. W. Daft, "Conformable transducers for large-volume, operator-independent imaging," in *2010 IEEE International Ultrasonics Symposium*, pp. 798–808, Oct. 2010.

[69] R. S. Singh, M. O. Culjat, M. Lee, D. B. Bennett, S. Natarjan, B. P. Cox, E. R. Brown, W. S. Grundfest, and H. Lee, "Conformal Ultrasound Imaging System," in *Acoustical Imaging* (M. P. Andr, J. P. Jones, and H. Lee, eds.), no. 30 in Acoustical Imaging, pp. 211–222, Springer Netherlands, 2011.

[70] M. S. Salim, M. F. Abd Malek, R. B. W. Heng, K. M. Juni, and N. Sabri, "Capacitive Micromachined Ultrasonic Transducers: Technology and Application," *Journal of Medical Ultrasound*, vol. 20, pp. 8–31, Mar. 2012.

[71] A. Caronti, G. Caliano, R. Carotenuto, A. Savoia, M. Pappalardo, E. Cianci, and V. Foglietti, "Capacitive micromachined ultrasonic transducer (CMUT) arrays for medical imaging," *Microelectronics Journal*, vol. 37, pp. 770–777, Aug. 2006.

[72] D. M. Mills and L. S. Smith, "Real-time in-vivo imaging with capacitive micromachined ultrasound transducer (cMUT) linear arrays," in *Ultrasonics, 2003 IEEE Symposium on*, vol. 1, pp. 568–571, IEEE, 2003.

[73] M. Legros, C. Meynier, R. Dufait, G. Ferin, and F. Tranquart, "Piezo-composite and CMUT arrays assessment through in vitro imaging performances," in *Ultrasonics Symposium, 2008. IUS 2008. IEEE*, pp. 1142–1145, IEEE, 2008.

[74] O. Oralkan, B. Bayram, G. G. Yaralioglu, A. S. Ergun, M. Kupnik, D. T. Yeh, I. O. Wygant, and B. T. Khuri-Yakub, "Experimental characterization of collapse-mode CMUT operation," *Ultrasonics, Ferroelectrics and Frequency Control, IEEE Transactions on*, vol. 53, no. 8, pp. 1513–1523, 2006.

[75] S. Olcum, F. Y. Yamaner, A. Bozkurt, and A. Atalar, "Deep-collapse operation of capacitive micromachined ultrasonic transducers," *Ultrasonics, Ferroelectrics and Frequency Control, IEEE Transactions on*, vol. 58, no. 11, pp. 2475–2483, 2011.

[76] S. Olcum, F. Yamaner, A. Bozkurt, H. Koymen, and A. Atalar, "An equivalent circuit model for transmitting capacitive micromachined ultrasonic transducers in collapse mode," *Ultrasonics, Ferroelectrics and Frequency Control, IEEE Transactions on*, vol. 58, no. 7, pp. 1468–1477, 2011.

[77] R. O. Guldiken, J. Zahorian, F. Yamaner, and F. Degertekin, "Dual-electrode CMUT with non-uniform membranes for high electromechanical coupling coefficient and high bandwidth operation," *Ultrasonics, Ferroelectrics and Frequency Control, IEEE Transactions on*, vol. 56, no. 6, pp. 1270–1276, 2009.

[78] H.-S. Yoon, M.-C. Ho, N. Apte, P. Cristman, S. Vaithilingam, M. Kupnik, K. Butts-Pauly, and B. T. Khuri-Yakub, "Fabrication of CMUT Cells with Gold Center Mass for Higher Output Pressure," in *AIP Conference Proceedings*, vol. 1359, p. 183, 2011.

[79] R. Guldiken, M. Balantekin, J. Zahorian, and F. Degertekin, "Characterization of dual-electrode CMUTs: demonstration of improved receive performance and pulse echo operation with dynamic membrane shaping," *IEEE Transactions on Ultrasonics, Ferroelectrics and Frequency Control*, vol. 55, pp. 2336–2344, Oct. 2008.

[80] T. A. Emadi and D. A. Buchanan, "Design and Fabrication of a Novel MEMS Capacitive Transducer With Multiple Moving Membrane, M$ˆ3$-CMUT," *IEEE Transactions on Electron Devices*, vol. 3, pp. 890–896, 2014.

[81] Y. P. Li, C. D. He, J. T. Zhang, J. L. Song, W. D. Zhang, and C. Y. Xue, "Design and Analysis of Capacitive Micromachined Ultrasonic Transducers Based on SU-8," *Key Engineering Materials*, vol. 645-646, pp. 577–582, May 2015.

[82] J. Joseph, S. Singh, and S. Vanjari, "Fabrication of SU-8 based Capacitive Micromachined Ultrasonic Transducer for low frequency therapeutic applications," in *2015 37th Annual International Conference of the IEEE Engineering in Medicine and Biology Society (EMBC)*, pp. 1365–1368, Aug. 2015.

[83] D.-Y. Chiou, M.-Y. Chen, M.-W. Chang, and H.-C. Deng, "Finite element modeling, characterization, and optimization design for the polymer-typed capacitive micro-arrayed ultrasonic transducer," *Microsyst Technol*, vol. 14, pp. 787–797, June 2008.

[84] S. Zhou and J. A. Hossack, "Reducing inter-element acoustic crosstalk in capacitive micromachined ultrasound transducers," *Ultrasonics, Ferroelectrics and Frequency Control, IEEE Transactions on*, vol. 54, no. 6, pp. 1217–1228, 2007.

[85] A. Caronti, C. Longo, A. Savoia, P. Gatta, G. Caliano, and M. Pappalardo, "Analysis of Acoustic Interaction Effects and Crosstalk in CMUT Linear Arrays for Medical Imaging," in *2006 Ieee Ultrasonics Symposium, Vols 1-5, Proceedings*, pp. 582–585, 2006. WOS:000260407800138.

[86] S. Berg and A. Ronnekleiv, "Reduction of crosstalk in CMUT Arrays by introducing double Periodicities," in *2007 Ieee Ultrasonics Symposium Proceedings, Vols 1-6*, pp. 2155–2158, 2007. WOS:000254281802039.

[87] X. Zhuang, A. S. Ergun, O. Oralkan, Y. Huang, I. O. Wygant, G. G. Yaralioglu, D. T. Yeh, and B. T. Khuri-Yakub, "Through-wafer trench-isolated electrical interconnects for CMUT arrays," in *IEEE International Ultrasonics Symposium*, 2005.

[88] C. Daft, S. Calmes, D. da Graca, K. Patel, P. Wagner, and I. Ladabaum, "Microfabricated ultrasonic transducers monolithically integrated with high voltage electronics," in *2004 IEEE Ultrasonics Symposium*, vol. 1, pp. 493–496 Vol.1, Aug. 2004.

[89] W. You, *Exploring multiple-mode vibrations of capacitive micromachined ultrasonic transducers (CMUTs)*. PhD thesis, 2013.

[90] F. M. Battiston, J. P. Ramseyer, H. P. Lang, M. K. Baller, C. Gerber, J. K. Gimzewski, E. Meyer, and H. J. Gntherodt, "A chemical sensor based on a microfabricated cantilever array with simultaneous resonance-frequency and bending readout," *Sensors and Actuators B: Chemical*, vol. 77, pp. 122–131, June 2001.

[91] L. Yang and C. Eng Gan, "Costing small cleanrooms," *Building and Environment*, vol. 42, pp. 743–751, Feb. 2007.

[92] D. Koester, A. Cowen, R. Mahadevan, M. Stonefield, and B. Hardy, "PolyMUMPs design handbook," *MEMSCAP Inc*, 2003.

[93] R. Bogue, "Towards the trillion sensors market," *Sensor Review*, vol. 34, pp. 137–142, Mar. 2014.

[94] "Global Flexible Electronics Market 2016-2020 - Research and Markets." `http://www.researchandmarkets.com/reports/3832417/global-flexible-electronics-market-2016-2020`. Accessed: 2017-01-20.

[95] ECRI Institute, "Modern Healthcare Price Index," index, Aug. 2014.

[96] P. Behnamfar and S. Mirabbasi, "A CMUT read-out circuit with improved receive sensitivity using an adaptive biasing technique," in *Biomedical Circuits and Systems Conference (BioCAS), 2011 IEEE*, pp. 397–400, IEEE, 2011.

[97] A. W. Leissa, *Vibration of plates*. DTIC Document, 1969.

[98] M. Greenspan, "Piston radiator: Some extensions of the theory," *The Journal of the Acoustical Society of America*, vol. 65, no. 3, pp. 608–621, 1979.

[99] T. Lehrmann Christiansen, O. Hansen, E. Vilain Thomsen, and J. Arendt Jensen, "Modal radiation patterns of baffled circular plates and membranes," *The Journal of the Acoustical Society of America*, vol. 135, pp. 2523–2533, May 2014.

[100] M. T.-K. Hou and R. Chen, "A new residual stress measurement method using ultra-wide micromachined bilayer cantilevers," *J. Micromech. Microeng.*, vol. 14, no. 4, p. 490, 2004.

[101] B. Bayram, M. Kupnik, G. G. Yaralioglu, O. Oralkan, D. Lin, X. Zhuang, A. S. Ergun, A. F. Sarioglu, S. H. Wong, and B. T. Khuri-Yakub, "Characterization of cross-coupling in capacitive micromachined ultrasonic transducers," in *Proc. IEEE Ultrason. Symp*, pp. 601–604, 2005.

[102] S. Mao, X. Rottenberg, L. Liu, V. Rochus, G. B. Torri, R. Haouari, B. Nauwelaers, and H. A. C. Tilmans, "A general multi-mode lumped equivalent circuit model for circular cMUT cells," in *2016 IEEE International Ultrasonics Symposium (IUS)*, pp. 1–4, Sept. 2016.

[103] A. Bozkurt, I. Ladabaum, A. Atalar, and B. Khuri-Yakub, "Theory and analysis of electrode size optimization for capacitive microfabricated ultrasonic transducers," *IEEE Transactions on Ultrasonics, Ferroelectrics, and Frequency Control*, vol. 46, pp. 1364–1374, Nov. 1999.

[104] H. Lorenz, M. Despont, N. Fahrni, N. LaBianca, P. Renaud, and P. Vettiger, "SU-8: a low-cost negative resist for MEMS," *J. Micromech. Microeng.*, vol. 7, no. 3, p. 121, 1997.

[105] C. Liu, "Recent Developments in Polymer MEMS," *Adv. Mater.*, vol. 19, pp. 3783–3790, Nov. 2007.

[106] "MicroChem - Innovative Chemical Solutions for MEMS and Microelectronics." `http://www.microchem.com/`. Accessed: 2017-09-04.

[107] I.-h. Song and P. K. Ajmera, "Use of a photoresist sacrificial layer with SU-8 electroplating mould in MEMS fabrication," *Journal of Micromechanics and Microengineering*, vol. 13, no. 6, p. 816, 2003.

[108] Y. Moser, R. Forti, S. Jiguet, T. Lehnert, and M. A. M. Gijs, "Suspended SU-8 structures for monolithic microfluidic channels," *Microfluidics and Nanofluidics*, vol. 10, no. 1, pp. 219–224, 2011.

[109] I. G. Foulds, R. W. Johnstone, and M. Parameswaran, "Polydimethylglutarimide (PMGI) as a sacrificial material for SU-8 surface-micromachining," *J. Micromech. Microeng.*, vol. 18, no. 7, p. 075011, 2008.

[110] M. S. Chiriac, M. Bianco, F. Amato, E. Primiceri, F. Ferrara, V. Arima, and G. Maruccio, "Fabrication of interconnected multilevel channels in a monolithic SU-8 structure using a LOR sacrificial layer," *Microelectronic Engineering*, vol. 164, pp. 30–35, Oct. 2016.

[111] V. Seidemann, J. Rabe, M. Feldmann, and S. Bttgenbach, "SU8-micromechanical structures with in situ fabricated movable parts," *Microsystem Technologies*, vol. 8, pp. 348–350, Aug. 2002.

[112] S. D. Psoma and D. W. Jenkins, "Comparative assessment of different sacrificial materials for releasing SU-8 structures," *Reviews on Advanced Materials Science*, vol. 10, no. 2, pp. 149–155, 2005.

[113] L. Dellmann, S. Roth, C. Beuret, G. A. Racine, H. Lorenz, M. Despont, P. Renaud, P. Vettiger, and N. F. de Rooij, "Fabrication process of high aspect ratio elastic and SU-8 structures for piezoelectric motor applications," *Sensors and Actuators A: Physical*, vol. 70, pp. 42–47, Oct. 1998.

[114] V. Linder, B. Gates, D. Ryan, B. Parviz, and G. Whitesides, "Water-Soluble Sacrificial Layers for Surface Micromachining," *Small*, vol. 1, pp. 730–736, July 2005.

[115] B. A. Peeni, M. L. Lee, A. R. Hawkins, and A. T. Woolley, "Sacrificial Layer Microfluidic Device Fabrication Methods," *Electrophoresis*, vol. 27, pp. 4888–4895, Dec. 2006.

[116] J. Melai, C. Salm, S. Smits, J. Visschers, and J. Schmitz, "The electrical conduction and dielectric strength of SU-8," *J. Micromech. Microeng.*, vol. 19, no. 6, p. 065012, 2009.

[117] W. Dai, K. Lian, and W. Wang, "A quantitative study on the adhesion property of cured SU-8 on various metallic surfaces," *Microsyst Technol*, vol. 11, pp. 526–534, July 2005.

[118] R. Feng and R. J. Farris, "Influence of processing conditions on the thermal and mechanical properties of SU8 negative photoresist coatings," *J. Micromech. Microeng.*, vol. 13, no. 1, p. 80, 2003.

[119] N. Tas, T. Sonnenberg, H. Jansen, R. Legtenberg, and M. Elwenspoek, "Stiction in surface micromachining," *J. Micromech. Microeng.*, vol. 6, no. 4, p. 385, 1996.

[120] E. Jeanne, C. Meynier, J. Terry, M. Roy, L. Haworth, and D. Alquier, "Evaluation of Parylene as protection layer for capacitive micromachined ultrasonic transducers," *ECS Transactions*, vol. 11, no. 16, pp. 25–33, 2008.

[121] V. M. Fthenakis and P. D. Moskovitz, "An assessment of silane hazards," *Solid State Technology*, vol. 33, pp. 81–85, Jan. 1990.

[122] Y. Huang, E. O. Hggstrom, X. Zhuang, A. S. Ergun, and B. T. Khuri-Yakub, "A solution to the charging problems in capacitive micromachined ultrasonic transducers," *Ultrasonics, Ferroelectrics and Frequency Control, IEEE Transactions on*, vol. 52, no. 4, pp. 578–580, 2005.

[123] K. K. Park, M. Kupnik, H. J. Lee, . Oralkan, and B. T. Khuri-Yakub, "Zero-bias resonant sensor with an oxide-nitride layer as charge trap," in *2010 IEEE Sensors*, pp. 1024–1028, Nov. 2010.

[124] I. O. Wygant, M. Kupnik, J. C. Windsor, W. M. Wright, M. S. Wochner, G. G. Yaralioglu, M. F. Hamilton, and B. T. Khuri-Yakub, "50 kHz capacitive micromachined ultrasonic transducers for generation of highly directional sound with parametric arrays," *Ultrasonics, Ferroelectrics and Frequency Control, IEEE Transactions on*, vol. 56, no. 1, pp. 193–203, 2009.

[125] J. A. Jensen, S. I. Nikolov, K. L. Gammelmark, and M. H. Pedersen, "Synthetic aperture ultrasound imaging," *Ultrasonics*, vol. 44, pp. e5–e15, Dec. 2006.

[126] "DuPont Polyimide Films." `http://www.dupont.com/products-and-services/membranes-films/polyimide-films.html`. Accessed: 2018-03-14.

[127] R. R. Richardson, J. A. Miller, and W. M. Reichert, "Polyimides as biomaterials: preliminary biocompatibility testing," *Biomaterials*, vol. 14, pp. 627–635, Jan. 1993.

[128] N. L. D. Somasiri, R. L. D. Zenner, and J. C. Houge, "A process for surface texturing of Kapton polyimide to improve adhesion to metals," in *1991 Proceedings 41st Electronic Components Technology Conference*, pp. 580–584, May 1991.

[129] C. D. Gerardo, E. Cretu, and R. Rohling, "Fabrication of Circuits on Flexible Substrates Using Conductive SU-8 for Sensing Applications," *Sensors*, vol. 17, p. 1420, June 2017.

[130] C. D. Gerardo, E. Cretu, and R. Rohling, "Fabrication and testing of Polymer-based Capacitive Micromachined Ultrasound Transducers for medical imaging," *Microsystems & Nanoengineering*, July 2018.

[131] X. Zhuang, D. S. Lin, . Oralkan, and B. T. Khuri-Yakub, "Fabrication of Flexible Transducer Arrays With Through-Wafer Electrical Interconnects Based on Trench Refilling With PDMS," *Journal of Microelectromechanical Systems*, vol. 17, pp. 446–452, Apr. 2008.

[132] A. I. H. Chen, L. L. P. Wong, S. Na, Z. Li, M. Macecek, and J. T. W. Yeow, "Fabrication of a Curved Row-Column Addressed Capacitive Micromachined Ultrasonic Transducer Array," *Journal of Microelectromechanical Systems*, vol. 25, pp. 675–682, Aug. 2016.

[133] J. McLean and F. L. Degertekin, "Interdigital capacitive micromachined ultrasonic transducers for sensing and pumping in microfluidic applications," in *TRANSDUCERS, Solid-State Sensors, Actuators and Microsystems, 12th International Conference on, 2003*, vol. 1, pp. 915–918, IEEE, 2003.

[134] G. Yaralioglu, "Ultrasonic heating and temperature measurement in microfluidic channels," *Sensors and Actuators A: Physical*, vol. 170, pp. 1–7, Nov. 2011.

[135] J. Joseph, S. G. Singh, and S. R. K. Vanjari, "A low pull-in SU-8 based Capacitive Micromachined Ultrasonic Transducer for medical imaging applications," in *2014 36th Annual International Conference of the IEEE Engineering in Medicine and Biology Society (EMBC)*, pp. 1398–1401, Aug. 2014.

[136] Y. Asaoka, T. Kanno, E. Yamamoto, T. Maeda, Y. Tsuda, and Y. Shimada, "Cavity Shape Control of the Roll-to-Roll Fabricated Novel Microstructure Film for Improving the Viewing-Angle Characteristics of LCDs," *SID Symposium Digest of Technical Papers*, vol. 45, pp. 17–20, June 2014.

[137] A. Khosla and B. L. Gray, "Photopatternable Electrical Conductive Ag- SU-8 Nanocomposite for MEMS/MST," *ECS Trans.*, vol. 33, pp. 313–318, Oct. 2010.

[138] S. Jiguet, A. Bertsch, H. Hofmann, and P. Renaud, "SU8-Silver Photosensitive Nanocomposite," *Adv. Eng. Mater.*, vol. 6, pp. 719–724, Sept. 2004.

[139] S. Jiguet, A. Bertsch, H. Hofmann, and P. Renaud, "Conductive SU8-silver composite photopolymer," in *Micro Electro Mechanical*

*Systems, 2004. 17th IEEE International Conference on. (MEMS)*, pp. 125–128, 2004.

[140] N. Hauptman, M. vegli, M. Maek, and M. K. Gunde, "Carbon based conductive photoresist," *J Mater Sci*, vol. 44, pp. 4625–4632, July 2009.

[141] M. Benlarbi, L. J. Blum, and C. A. Marquette, "SU-8-carbon composite as conductive photoresist for biochip applications," *Biosensors and Bioelectronics*, vol. 38, pp. 220–225, Oct. 2012.

[142] C. Grimaldi, M. Mioni, R. Gaal, L. Forr, and A. Magrez, "Electrical conductivity of multi-walled carbon nanotubes-SU8 epoxy composites," *Applied Physics Letters*, vol. 102, p. 223114, June 2013.

[143] M. Mioni, K. Pataky, R. Gaal, A. Magrez, J. Brugger, and L. Forr, "Carbon nanotubesSU8 composite for flexible conductive inkjet printable applications," *J. Mater. Chem.*, vol. 22, pp. 14030–14034, June 2012.

[144] H. Cong, L. Hong, R. S. Harake, and T. Pan, "CNT-based photopatternable nanocomposites with high electrical conductivity and optical transparency," *J. Micromech. Microeng.*, vol. 20, p. 025002, Feb. 2010.

[145] M. Majidian, C. Grimaldi, A. Pisoni, L. Forr, and A. Magrez, "Electrical conduction of photo-patternable SU8graphene composites," *Carbon*, vol. 80, pp. 364–372, Dec. 2014.

[146] U. Annaiyan, K. Kalantar-Zadeh, Q. Fang, and I. Cosic, "Development of a conductive photoresist with a mixture of SU-8 and HCl doped polyaniline," in *TENCON 2005 2005 IEEE Region 10*, pp. 1–5, Nov. 2005.

[147] H. C. Chiamori, J. W. Brown, E. V. Adhiprakasha, E. T. Hantsoo, J. B. Straalsund, N. A. Melosh, and B. L. Pruitt, "Suspension of nanoparticles in SU-8: Processing and characterization of nanocomposite polymers," *Microelectronics Journal*, vol. 39, pp. 228–236, Feb. 2008.

[148] P. Renaud, S. Metz, S. Jiguet, and A. Bertsch, "Composite photopolymer microstructures: from planar to 3d devices," in *TRANSDUCERS, Solid-State Sensors, Actuators and Microsystems, 12th International Conference on, 2003*, vol. 2, pp. 991–994 vol.2, June 2003.

[149] L. Gammelgaard, P. A. Rasmussen, M. Calleja, P. Vettiger, and A. Boisen, "Microfabricated photoplastic cantilever with integrated photoplastic/carbon based piezoresistive strain sensor," *Applied Physics Letters*, vol. 88, no. 11, p. 113508, 2006.

[150] L. K. Siong, I. Abdul Azid, O. Sidek, K. Ibrahim, and M. Devarajan, "SU-8 piezoresistive microcantilever with high gauge factor," *IET Micro Nano Letters*, vol. 8, pp. 123–126, Mar. 2013.

[151] S. Jiguet, A. Bertsch, H. Hofmann, and P. Renaud, "Conductive SU8 Photoresist for Microfabrication," *Adv. Funct. Mater.*, vol. 15, no. 9, pp. 1511–1516, 2005.

[152] S. H. Cho, N. Xue, L. Cauller, W. Rosellini, and J. B. Lee, "A SU-8-Based Fully Integrated Biocompatible Inductively Powered Wireless Neurostimulator," *Journal of Microelectromechanical Systems*, vol. 22, pp. 170–176, Feb. 2013.

[153] W. Jillek and W. K. C. Yung, "Embedded components in printed circuit boards: a processing technology review," *Int J Adv Manuf Technol*, vol. 25, pp. 350–360, Feb. 2005.

[154] E. H. Conradie and D. F. Moore, "SU-8 thick photoresist processing as a functional material for MEMS applications," *J. Micromech. Microeng.*, vol. 12, no. 4, p. 368, 2002.

[155] C. Ge and E. Cretu, "MEMS transducers low-cost fabrication using SU-8 in a sacrificial layer-free process," *J. Micromech. Microeng.*, vol. 27, no. 4, p. 045002, 2017.

[156] J. D. Venables, "Adhesion and durability of metal-polymer bonds," *J Mater Sci*, vol. 19, pp. 2431–2453, Aug. 1984.

[157] J. Fjelstad, *Flexible Circuit Technology*. Silicon Valley Publishers Group, 1998. Google-Books-ID: gavjAQAACAAJ.

[158] J. P. Gianvittorio and Y. Rahmat-Samii, "Fractal antennas: a novel antenna miniaturization technique, and applications," *IEEE Antennas and Propagation Magazine*, vol. 44, pp. 20–36, Feb. 2002.

[159] N. Xiang, H. Yi, K. Chen, S. Wang, and Z. Ni, "Investigation of the maskless lithography technique for the rapid and cost-effective prototyping of microfluidic devices in laboratories," *Journal of Micromechanics and Microengineering*, vol. 23, no. 2, p. 025016, 2013.

[160] J. Webster and H. Eren, *Measurement, Instrumentation, and Sensors Handbook, Second Edition: Two-Volume Set*. Jan. 2014.

[161] R. Xu, "Light scattering: A review of particle characterization applications," *Particuology*, vol. 18, pp. 11–21, Feb. 2015.

[162] J. C. Russ, *The Image Processing Handbook, Seventh Edition*. CRC Press, Jan. 2016. Google-Books-ID: ROSYCgAAQBAJ.

[163] "Abracon Near Field Communications." `https://abracon.com/product-lineup/rf-connectivity/near-field-communications-nfc`. Accessed: 2018-07-12.

[164] "Ionbeam Planar Chip Inductors." `https://www.ionbeammilling.com/PLANAR_CHIP_INDUCTORS`. Accessed: 2016-10-27.

[165] D. Masse, "RF and Microwave Semiconductor Device Handbook," *Microwave Journal*, vol. 46, no. 12, pp. 176–177, 2003.

[166] S. Grego, J. Lewis, E. Vick, and D. Temple, "Development and evaluation of bend-testing techniques for flexible-display applications," *Journal of the Society for Information Display*, vol. 13, pp. 575–581, July 2005.

[167] Z. Suo, E. Y. Ma, H. Gleskova, and S. Wagner, "Mechanics of rollable and foldable film-on-foil electronics," *Applied Physics Letters*, vol. 74, pp. 1177–1179, Feb. 1999.

[168] J. L. S. Emeterio, A. Ramos, P. T. Sanz, and A. Ruiz, "Evaluation of Impedance Matching Schemes for Pulse-Echo Ultrasonic Piezoelectric Transducers," *Ferroelectrics*, vol. 273, pp. 297–302, Jan. 2002.

[169] S. Joshi, S. Yazadi, V. Henneken, R. Dekker, and R. Sanders, "Conformable body patches for ultrasound applications," in *2015 IEEE 17th Electronics Packaging and Technology Conference (EPTC)*, pp. 1–4, Dec. 2015.

[170] J. C. Schelleng, "The Violin as a Circuit," *The Journal of the Acoustical Society of America*, vol. 35, pp. 326–338, Mar. 1963.

[171] "Polyjet Matrix 3d Printing." `http://proto3000.com/polyjet-matrix-3D-printing-technology-services.php`. Accessed: 2018-07-10.

[172] "Metal 3d printer ProX DMP 300." https://www.3dsystems.com/3d-printers/prox-dmp-300. Accessed: 2018-07-10.

# Appendix A

# Combining Symmetric and Asymmetric CMUTs in an array

As stated in section 1.3.1, when an asymmetric CMUT cell is operating in water, the first vibration mode (0,1) appears overdamped with a wide band frequency response, whereas the second vibration mode (1,1) is still resonant. It has been explored the possibility of exploiting the resonant behavior of an asymmetric CMUT cell to extract more information from ultrasonic waves using the signals on each electrode of the asymmetric cell [21]. The problem with this approach is that the separation in frequency between the first mode and the second mode is too large compared to the frequency range of the transmitted pulse and corresponding echoes.

Motivated by this resonant behavior of the asymmetric mode and the potential applications of asymmetric CMUTs discussed in section 1.3.1 we created an array of asymmetric CMUT elements in a silicon chip. We conceived the idea of having both symmetric and asymmetric CMUT cells operating in array; the symmetric cells were designed to be used during transmission,

having a square shape; whereas the asymmetric cells were designed to be used during reception, having a rectangular shape. The key concept here is to match the first resonant frequency (0,1) of the square CMUTs with the second resonant frequency (1,1) of the rectangular ones as depicted in Figure A.1. This way we would be able to extract some extra information from the transmitted and received ultrasonic pulses within the same bandwidth of the transducers.

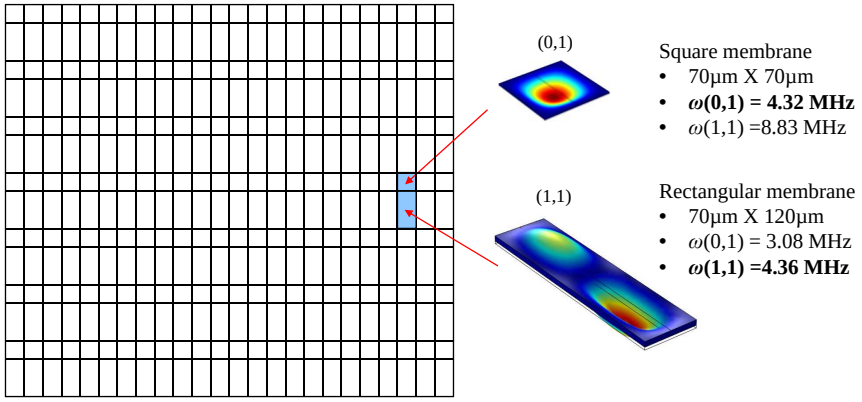


Figure A.1: Proposed chip structure of the CMUT array. Containing 32 rows of square membranes and 32 rows of rectangular membranes in parallel

Before developing the fabrication process for polyCMUTs, the PolyMUMPs fabrication process [92] was used to fabricate the chips, a three-layer polysilicon micromachining process offered by MEMSCAP Inc.(North Carolina, USA). The general layout of the chip is shown in Figure A.2; it consists of 32 rows of rectangular and 32 rows of square CMUT elements with 100 CMUT cells on each row. At the bottom of the chip we included some test cells using different silicon layers as the electrodes for the CMUTs. The physical dimensions of each cell are specified in Table A.3.

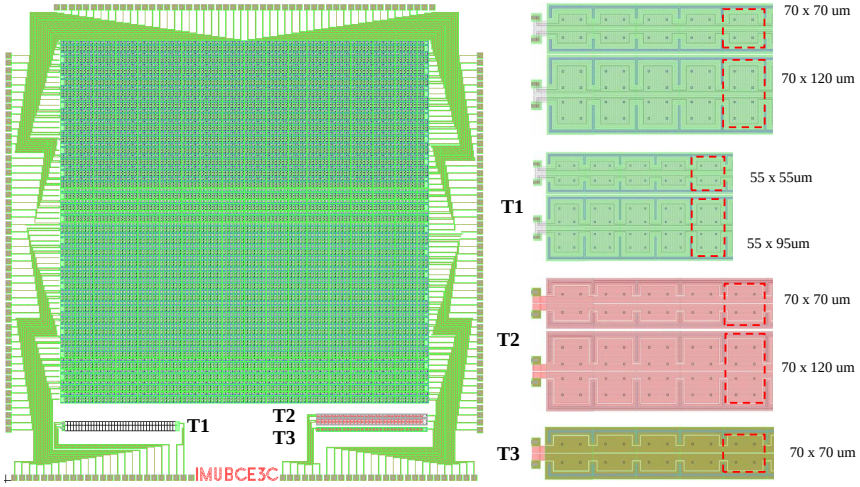


Figure A.2: General layout of the asymmetric CMUT array, showing the details of individual cells and the test structures

| CMUT cell location | Shape | Width (µm) | Length (µm) | Membrane thickness (µm) | Bottom E. thickness (µm) | Air gap (µm) | Calculated resonant frequency (MHz) | | Measured resonant frequency (MHz) | |
|---|---|---|---|---|---|---|---|---|---|---|
| | | | | | | | (0,1) mode | (1,1) mode | (0,1) mode | (1,1) mode |
| **Array** | **Square** | 70 | 70 | 1.5 | 2 | 0.75 | 4.33 | 8.83 | 4.35 | 9.47 |
| **Array** | **Rectangular** | 70 | 120 | 1.5 | 2 | 0.75 | 3.08 | 4.36 | 4.03 | 5.79 |
| **Test cells 1 (T1)** | **Square** | 55 | 55 | 1.5 | 2 | 0.75 | 7.01 | 14.03 | 5.08 | 12.55 |
| **Test cells 1 (T1)** | **Rectangular** | 55 | 95 | 1.5 | 2 | 0.75 | 4.97 | 7.01 | 5.11 | 8.93 |
| **Test cells 2 (T2)** | **Square** | 70 | 70 | 2 | 0.5 | 2 | 5.77 | 11.77 | 4.58 | 10.06 |
| **Test cells 2 (T2)** | **Rectangular** | 70 | 120 | 2 | 0.5 | 2 | 4.11 | 5.81 | 3.38 | 5.15 |
| **Test cells 3 (T3)** | **Square** | 70 | 70 | 1.5 | 0.5 | 2.75 | 4.33 | 8.83 | 3.19 | 7.01 |

Table A.3: Parameters of the asymmetric CMUT array, including theoretical and experimental values of the resonant frequencies

The resonant frequencies of the square and rectangular membranes shown in Table A.3 were calculated using plates vibration theory [14], considering a flat plate clamped all-around.

We measured the topography of the membrane using a white light interferometer (Polytec,Inc., CA, USA), being able to visualize the fine details of each cell; the results are shown in Figure A.4, with a simulated cross sectional view of the transducers shown below.

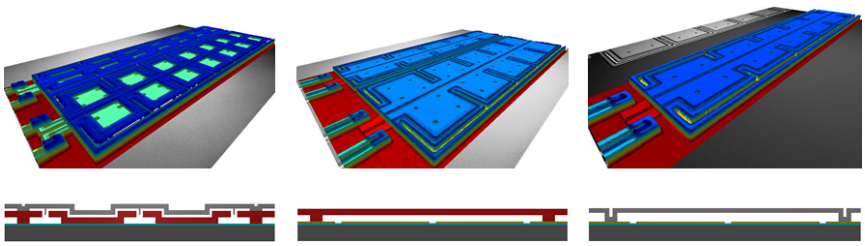

Figure A.4: Measured topography of the different CMUT cells in the chip and the simulated cross-sectional view. Left to right: CMUTs in the array, test cells 2 and test cells 3

The CMUT array was characterized using a Laser Doppler Vibrometer (LDV) Polytec® Microsystem Analyzer (MSA-500) (Polytec,Inc., CA, USA). The frequency response of the square and rectangular membranes is shown in Figure A.5, and a comparison between theoretical and experimental values is shown in Table A.3. A discrepancy was found between resonant frequencies of the modes. Ideally, the frequency of the first mode in the square membranes would match with the frequency of the second mode in the rectangular ones. We attribute this discrepancy to the real shape of the fabricated membrane; instead of being flat, the membrane has a corrugated structure that increases the overall stiffness [97], having a higher than expected resonant frequency.

Another contribution to the discrepancy is the consideration of the clamped edges; we calculated the expected resonant frequencies considering a fully clamped membrane, but in reality, there is an unclamped section at the middle of perimeter of the real membrane to allocate the electrical connections for the two bottom electrodes.

As stated in section 1.3.1, it is desired for a CMUT to have a sealed

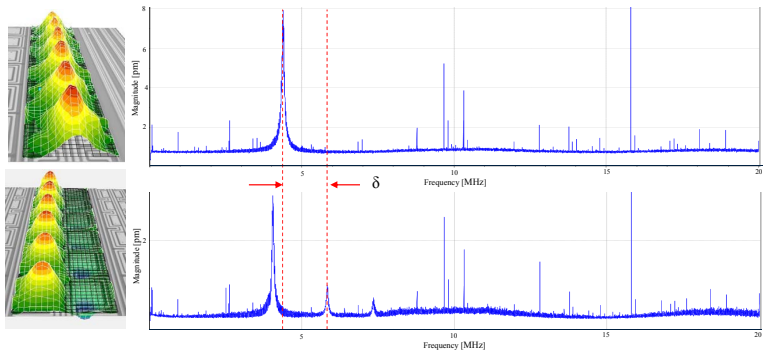


Figure A.5: Comparison of the frequency response of asymmetric CMUTs in the array showing the separation in frequency ($\delta$) between the mode (0,1) for the square membranes and mode (1,1) for the rectangular membranes

cavity in order to operate it in water; however one of the disadvantages of the PolyMUMPS technology we used is that there are unsealed releasing holes on the CMUT membranes, making it impossible to perform fluid-immersion experiments. It is necessary to seal these holes for immersed applications, otherwise water might enter into the cavities and cause a short circuit between the electrodes.

This novel integration of symmetric and asymmetric CMUTs working together on the same array could be benefited from the fabrication process developed for polyCMUTs, with future experiments still pending.

# Appendix B

# Polysilicon-based CMUTs sealing experimentation using an aerosol jet printer

As stated in section 1.5.2 ,the PolyMUMPs technology is a relatively inexpensive alternative to fabricate silicon chips. Nevertheless, the main disadvantage is that it is not possible to create CMUTs with sealed cavities for immersed applications. Motivated by this limitation, we attempted to seal the releasing holes of the CMUTs membranes using an Aerosol Jet Printer (Optomec®, NM, USA) available our laboratory. This kind of equipment is capable to deposit materials with a viscosity up to 1000cP using high pressurized gas to atomize, transport and focus an aerosol mist on a substrate without making physical contact.

We attempted to seal the releasing holes of previous CMUT chips fabricated using the same PolyMUMPS technology. Each chip has 71 rows of circular CMUT cells connected in parallel, and each CMUT cell has a diameter of 94$\mu$m and 12 square releasing holes with a size of 3$\mu$m each. We tried different kinds of photoresists available in the cleanroom as sealing

materials, such as 950-PMMA-C4, 950-PMMA-A5, 495-PMMA-A6 and PR-S1813. The best results were obtained when using 495-PMMA-A6. During the deposition of the material, we encountered difficulty trying to adjust the printing parameters to get narrow and continuous printed lines. The narrowest printing line we could get was 10$\mu$m wide; during the printing process it was necessary to constantly re-adjust the printing parameters to maintain relatively continuous lines.

An image showing the unsealed cells, the printing pattern (cross-shape design on each releasing hole) and the sealed cells is shown in Figure B.1. It can be noticed that the amount of material deposited for the top cells is less than the material deposited for the cells at the bottom. This is due to the increase in the material viscosity caused by the evaporation of the solvent present in the mixture; since a constant amount of gas is being blown into a jar containing the material, part of the volatile solvent is evaporated, making the mixture denser and causing a non-uniformity in the printed patterns.

The operation of the sealed CMUT cells was later characterized using a Laser Doppler Vibrometer. A 0-10 MHz chirp signal with an amplitude of 100V was applied to the CMUT elements to measure their new resonant frequency. The results corresponding to one of the sealed rows is shown in Figure B.2.

Each row has two electrical connections on each side; the outermost cells were still vibrating after the sealing process, having a new resonant frequency of 2.66MHz (compared to 2.57MHz of unsealed cells). After some detailed examination we discovered that some of the releasing holes in all the

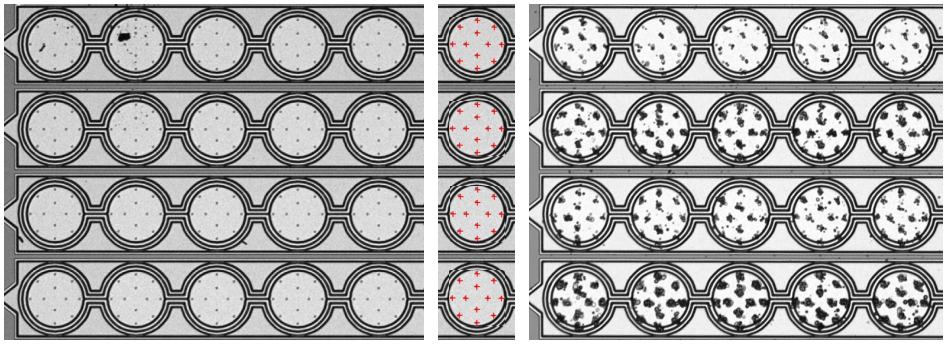


Figure B.1: Section view of CMUT array showing the unsealed membranes (left), the printing pattern (center) and the cells after sealing (right)

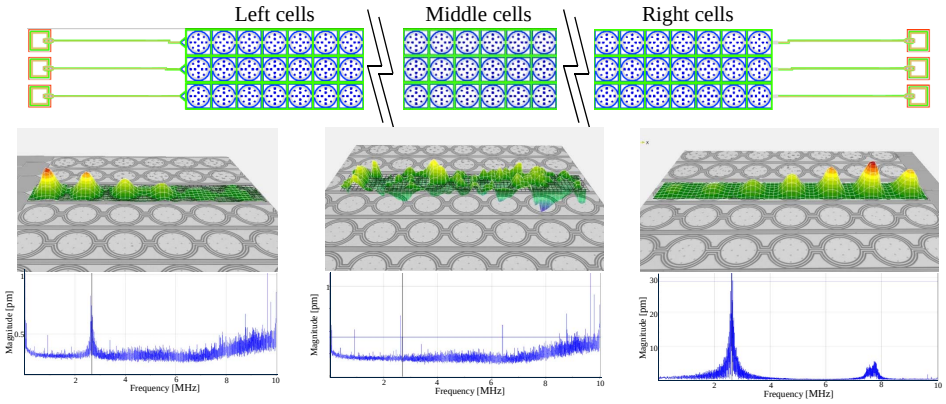


Figure B.2: Frequency response of a row of sealed CMUT membranes showing the variation in resonant frequency

rows were not covered by the sealing material, leaving the original releasing holes prone to cause a short circuit if the chip were immersed in water; therefore immersed tests were not carried out for this chip.

Different sealing techniques to cover the releasing holes of the membrane are yet to be tested. One of the potential sealing techniques is to use a mask-

less lithography system to deposit and selectively polymerize photoresist on top of the releasing holes, creating a watertight seal for immersed applications. Another alternative is to use a more viscous material as a sealing agent, this would prevent the sealant to go inside the cavities.

# Appendix C

# Alternative fabrication for CMUTs

As outlined in section 1.3.3, a typical approach to fabricate CMUTs is by using lithographic fabrication techniques, where the final structures are produced by the deposition and selectively removal of material layers. One of the inconveniences of this approach is that is an expensive fabrication technique; specially when the number of devices produced is low.

Recently, some state-of-the-art equipment like an Aerosol Jet printer, a 3D printer, a Laser Micromachining System, and a Maskless Lithography System was installed in the Microsystems and Nanotechnology (MiNa) laboratory at the UBC; making this set of equipment unique in Canada. Motivated by the potential interaction between this equipment and the fact that developing ultrasonic industry needs a fast way to create prototypes, we attempted to fabricate capacitive ultrasonic transducers using a non-conventional fabrication approach.

**Electrostatically actuated 3D printed structures**

As a proof of concept, we successfully fabricated electrostatically driven devices coupling a 3D printer and an Aerosol Jet Printer. Support structures were created using a 3D printer (Projet 3510HD 3D Systems®, SC, USA). A structure acting as the base of the transducers was coated with conductive paint to act as a bottom electrode using an Aerosol Jet Printer; a second structure containing the movable devices was also coated with conductive silver paint to act as a top electrode; finally, an AC voltage was applied across electrodes and their displacement was measured using a Laser Doppler Vibrometer. Figure C.1 shows some of the fabricated structures and their characterization; from left to right, an array of cantilevers (3mm in length, 100$\mu$m thick and 50-200$\mu$m in width), doubly-clamped beams (3mm in length, 100$\mu$m thick and 50-200$\mu$m in width) and square membranes (100$\mu$m thick and 50-5000$\mu$m in side length)[5].

The resulting devices had a low quality factor (Q) of about 10, probably because of the mechanical properties of the ABS-like material used by the 3D printer. We experimentally discovered that the microstructures did not have a uniform resonant frequency among similar cantilevers. This might have been caused by the resolution of the 3D printer, causing a variation in the final dimensions of the structures.

A post analysis of the printed structures using a white light interferometer revealed that the surfaces of the final structures were not completely flat, having crests and valleys in the order of tens of microns. Because the con-

[5]The results shown in this section were presented at the $2^{nd}$ International Congress on Materials and Renewable Energy (MRE) in Hong Kong in 2014

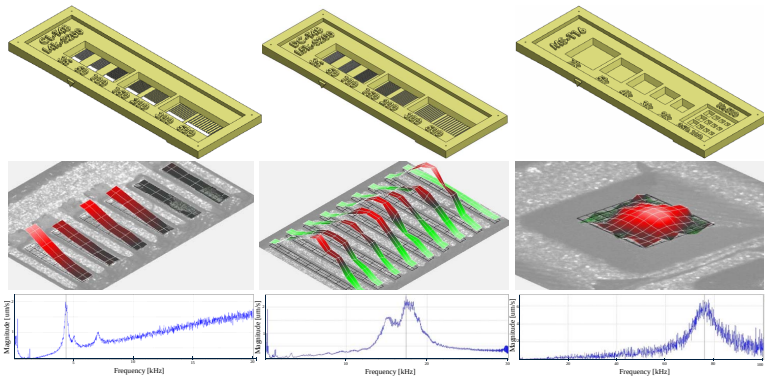

Figure C.1: Different electrostatically actuated structures showing the frequency response and the deflections measured using an LDV. Left to right: cantilevers, doubly-clamped beams and square membranes

ductive silver ink was deposited in liquid state before drying and becoming conductive, some of this paint might have accumulated in the uneven parts of the printed structures, causing a variation in the resonant frequency.

Different coating techniques were also used to metalize the 3D printed structures; we tried to gold-coat the structures using an e-beam evaporator; we also tried to manually coat them using a small brush; however the non-uniformity in the resonant frequencies of the final devices was still present.

### Copper foil CMUTs

The most critical step during the fabrication of CMUTs is to obtain a sealed membrane suspended on top of a sub-micron cavity. We devised the idea of creating CMUTs by integrating commercially available products aided with the equipment in the MiNa laboratory.

Copper tape is commonly used by the RF industry to reduce the effects

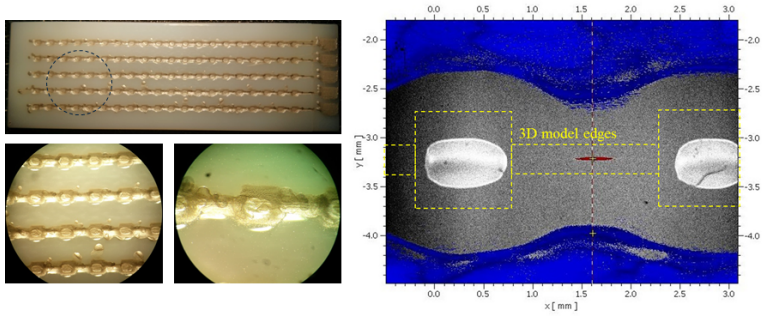


Figure C.2: Support structure from 3D printer showing the printer bottom electrodes (left). Measured topography revealing the discrepancies between the 3D model and the real model

of electromagnetic interference in electronic components. This tape is made of pure copper foil with a layer of dielectric adhesive at the bottom. We attempted to integrate this copper tape as part of a CMUT. We fist created a support structure including some cavities using a 3D printer, then we deposited silver paint to act as the bottom electrode using an Aerosol Jet Printer, finally some copper tape was glued on top of the structure to act as the membrane of our CMUTs.

The support structure with the printed electrodes is shown in Figure C.2. The cavities have 1x1 mm square shapes with a connecting channel between them. Measuring the real geometry of the cavities using a white light interferometer revealed that the real dimensions are very different from the dimensions in the 3D model as shown in Figure C.2. The blue area represent the edges of the real device, and the dotted lines represents the dimensions according to the 3D model.

The thickness of the copper tape used was 36$\mu$m, and the thickness of

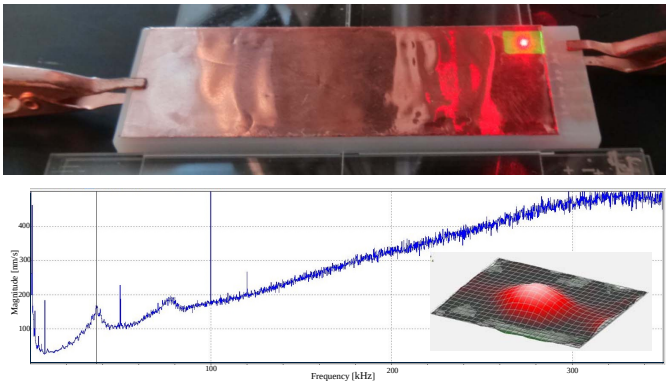


Figure C.3: Final device with the copper tape glued on the support structure (top). Frequency response and deflection shape of membranes captured by an LDV (bottom)

the dielectric adhesive was 30$\mu$m. Ideally, the expected resonant frequency of such membranes would be 226.8kHz. The final device was later characterized using a Laser Doppler Vibrometer, applying a 100V 0-400kHz chirp signal. The final device with the electrical connections is shown in Figure C.3, with its measured frequency response shown at the bottom. The measured resonant frequency of the membranes was 36.5kHz, much below than the expected value.

We suspect that the discrepancy between the expected and the measured resonant frequency was caused by the real dimensions of the printed structures. Moreover, since the properties of the dielectric adhesive are unknown, the effect it had on the calculated resonant frequency was not taken into account.

As a second fabrication approach, we used a piece of copper clad PCB as a bottom electrode, then we created some cavities using a Laser Micro-

machining System (Oxford Lasers®, OX, UK) to finally glue some copper tape on top to act as the membrane of our CMUTs. The Laser Micromachining system used has a picosecond solid-state laser with a beamwidth of about 30$\mu$m. Two different sizes for the cavities were created: 500$\mu$m and 1mm. It was necessary to use 15 passes of the latter over the same pattern at 10% of the laser power in order to create a flat cavity.

The topography of the cavities was measured using a white light interferometer (Figure C.4). The real diameters of the cavities were 523$\mu$m and 1032$\mu$m, with a depth of 31$\mu$m; having very similar dimensions from the input CAD files.

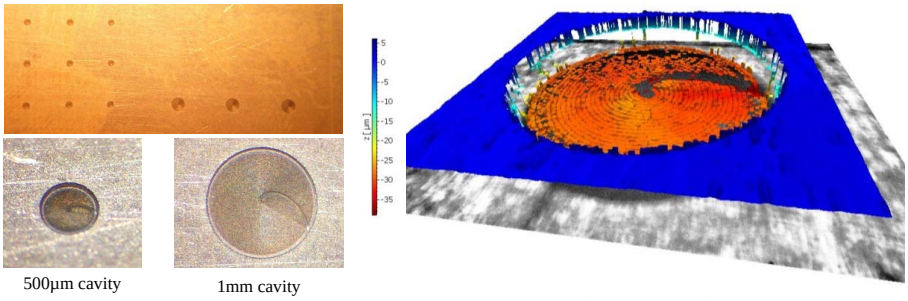


Figure C.4: Cavities created using a Laser Micromachining System (left) and measured topography using a white light interferometer (right)

Ideally the resonant frequencies of the membranes would be 256.5kHz and 64.13kHz for the 500$\mu$m and 1mm membrane sizes respectively. The final device and the frequency response of the system is shown in Figure C.5. A resonant frequency of 163kHz was measured for the 500$\mu$m CMUTs, and a frequency of 124.7kHz for the 1mm CMUTs. Once again, the ideal and measured resonant frequencies are very different. We attribute this effect

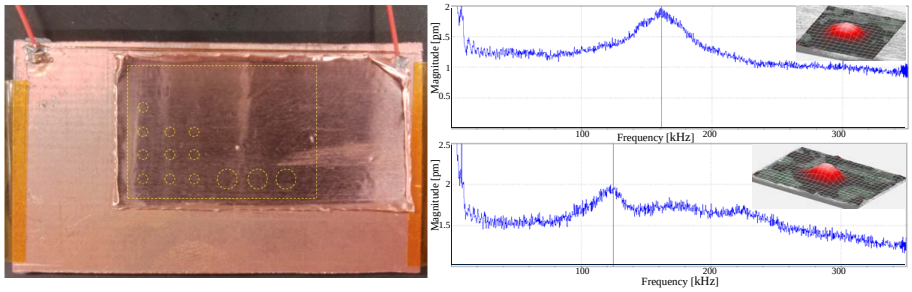


Figure C.5: Final device showing the electrical connections on top (left). Frequency response of 500um (top) and 1mm membranes (bottom)

to the unknown properties of the adhesive layer in the copper tape.

One of the disadvantages of this approach is that the creation of the cavities is serialized, making it a extremely slow process. For instance, it took almost 2 hours to create an array of 5x5 cavities of 500$\mu$m in diameter and 15$\mu$m in depth.

New technology for 3D printers could still benefit this fabrication approach. Recent 3D printers can now combine two or more materials at the same time [171], with the possibility of even printing metals [172]. These could be used to directly create CMUTs on virtually any surface.